Dissertation
submitted to the
Combined Faculties for the Natural Sciences and for Mathematics
of the Ruperto-Carola University of Heidelberg, Germany
for the degree of
Doctor of Natural Sciences

presented by

Diplom-Physicist: Roland Jesseit
born in: Hamburg

Oral Examination: 21. January 2004

The Orbital Structure of Galaxies and Dark Matter Halos in N-Body Simulations

Referees: **Prof. Dr. Andreas Burkert**
Prof. Dr. Hans-Walter Rix

Die Orbitale Struktur von Galaxien und Dunkle Materie Halos in N-Körper Simulationen

In dieser Arbeit werden zwei Entstehungmechanismen für Galaxien in N-Körper Rechnungen untersucht. Unter der Annahme, dass die Teilchen in einem sphärischen dunkle Materie Halo sich auf Kreisbahnen bewegen, macht die adiabatische Näherung genaue Voraussagen über das Maß der Kontraktion des Halos während der langsamen Scheibenbildung. Wir finden in N-Körper Rechnungen, dass die adiabatische Näherung für alle realistischen Massenverhältnisse zwischen Scheibe und Halo gilt, und Abweichungen von Kreisbahnen keine grössere Rolle spielen.

Im zweiten Teil beschäftigen wir uns mit der Entstehung von elliptischen Galaxien durch Verschmelzung von Scheibengalaxien. In einem Sample von 150 solcher Kollisionen klassifizieren wir die komplexe orbitale Struktur des Endergebnisses jeder Kollisionsrechnung. Die Klassifikation wird mit der Triaxialität und der Länge der Hauptträgheitsachsen verknüpft, mit denen die Gestalt einer elliptischen Galaxie parametrisiert wird. Wir leiten daraus eine globale Besetzungswahrscheinlichkeit für selbstkonsistente triaxiale Galaxien ab, die mit theoretischen Erwartungen übereinstimmt.

Weiterhin finden wir, dass die Isophotenstruktur in den N-Körperrechnungen nicht von einer Orbitgattung, sondern von einer Überlagerung verschiedener Gattungen herrührt. Die Dichotomie zwischen elliptischen Galaxien mit boxförmigen und scheibenförmigen Isophoten kann deswegen nicht vollständig auf eine Dominanz von box- bzw. scheibenförmigen Orbits zurückgeführt werden. Bisherige Simulationen können nicht beobachtete Korrelationen zwischen dem h_3 Parameter und der mittleren Geschwindigkeit reproduzieren. Als Ursache dieser Diskrepanz werden die box Orbits identifiziert, die in dissipationslosen Simulationen überproduziert werden. Z-tube Orbits erfüllen diese Korrelation jedoch sehr gut. Ebenso zeigt diese Komponente dieselbe Korrelation zwischen dem h_3 Parameter und v/σ_0, wie beobachtete elliptische Galaxien. Wir schließen daraus, dass nur eine dynamische Komponente, nämlich eine sehr dicke Scheibe mit hoher Geschwindigkeitsdispersion ausreicht, um beobachtete Korrelationen zu erklären.

The Orbital Structure of Galaxies and Dark Matter Halos in N-Body Simulations

We examine in this work two different formation mechanism of galaxies in N-body simulations. Under the assumption that particles in a spherical dark matter halo move on circular orbits we can predict the amount of contraction of the dark matter halo during the slow formation of the disk with an adiabatic approximation. We find in N-body simulations that the adiabatic approximation is valid for all realistic mass ratios between dark matter halos and disk galaxies and that deviations from circular orbits cannot play a decisive role. In the second part we focus on the formation of ellipticals through mergers of disk galaxies. We classify the complex orbital structure in a sample of 150 collisions. The classification is correlated with shape parameters of an elliptical galaxy, such as its triaxiality or the ratios of its principal axes. We are deriving a global occupation probability for self-consistent triaxial galaxies which are in agreement with theoretical expectations. Furthermore we find that the isophotal structure of the merger remnants cannot be explained by one orbit class alone, but by a superposition of classes. The dichotomy of observed isophotal shape in boxy and disky elliptical galaxies, cannot be completely explained by the dominance of box-like, respectivley disk-like orbits in those galaxies. Current simulations cannot reproduce observed correlation between the h_3 parameter and the mean velocity. We identify a central box orbit component as the reason for this discrepancy, which are overproduce in dissipationless simulations. The z-tube component follows the correlation very well. It follows also the observed correlation between the h_3 parameter and v/σ_0. We conclude that only one dynamical component is necessary to explain the observed correlations, which looks like a puffy disk with high velocity dispersion.

Meinen Eltern

Contents

Chapter 1

Slow Galaxy Formation - The Adiabatic Approximation

1.1 Introduction

The hierarchical clustering model is the paradigm for galaxy formation today. In this cosmological scenario, structure forms around peaks of primordial dark matter density fluctuations. The baryonic matter, which can dissipate energy through radiation, cools and falls into the center of its surrounding dark halo. The question of how a spherical mass distribution, e.g. a galactic bulge, will respond to the growth of mass in its center has been adressed by Barnes & White (1984), hereafter BW84. They devised a simple recipe for predicting the density profile of a contracted spherical density distribution. This recipe was used by Blumenthal et al. (1986) to examine contracted dark halos, assuming that the baryonic disk forms in the center so slowly that the time for the increase of mass inside an orbit of a dark particle is long compared to its orbital period. In a slowly varying potential the action integral $j_i = \int p_i dq_i$ is a conserved property of the particle orbit, called an adiabatic invariant (Binney & Tremaine, 1987). Here, j is the action, p and q are the phase space coordinates of the dark particle. As a first approximation, BW84 assumed a spherical density distribution with particles moving on circular orbits. In this case, the radial action integral simplifies to the conservation of angular momentum. With $L = mvr$ and the circular velocity $v^2(r) = GM(r)/r$ we get the adiabatic invariant $M(r)r$.
Given that we know the final baryonic matter distribution, e.g. an exponential disk-like profile $M_b(r)$ and the initial dark halo distribution $M_i(r)$, we can construct the final dark matter distribution $M_f(r)$ according to

$$r_f[M_b(r_f) + M_f(r)] = rM_i(r), \tag{1.1}$$

where r_f is the final radius of a dark particle. This approximation is strictly valid only if the initial mass distribution is spherically symmetric. The mapping between initial and final radius is unique, because the dark particles are dissipationless and their circular orbits do not cross. The adiabatic compression has been used widely in estimating rotation curves in semi-analytical galaxy models (Ryden & Gunn, 1987; Ryden, 1988, 1991; Flores et al., 1993; Mo et al., 1998), in investigating the origin of the Tully-Fisher relation (Courteau & Rix, 1999), in analysing the core structure of dark matter halos (van den Bosch & Swaters, 2001; Marchesini et al., 2002) and in the formation of gaseous disks in cosmological N-body halos (M. Steinmetz 2001, private communication). The adiabatic contraction assumption has been tested qualitatively in a low-resolution study by Blumenthal et al. (1986).

It is surprising that equation (1.1) should hold in realistic situations, where a non-spherical galactic disk is added to a halo of particles which move on eccentric or chaotic orbits (Valluri & Merritt, 2000).

Table 1.1: Model runs

Model	M_d/r_d	Particle Number	ϵ	timestep	total time
1	0.05/0.14	10000	0.03	6.25e-3	adiabatic
2	0.05/0.14	80000	0.01	6.25e-3	adiabatic
3	0.05/0.14	200000	0.007	6.25e-3	adiabatic
4	0.2/0.14	10000	0.03	1.57e-3	adiabatic
5	0.2/0.14	80000	0.01	1.57e-3	adiabatic
6	0.2/0.14	200000	0.007	1.57e-3	adiabatic
7	0.05/0.14	200000	0.007	6.25e-3	violent
8	0.2/0.14	200000	0.007	1.57e-3	violent
9	0.2	10000	0.03	1.57e-3	point grow
10	0.2	10000	0.03	1.57e-3	point contract

1.2 The Simulations

The N-body halo is set up according to the distribution function devised by Hernquist (1990, 1993). Its density distribution is $\rho(r) = M_h r_h/[2\pi r(r+r_h)^3]$, where M_h is the total mass and r_h is the scale length. The Hernquist halo has the same $\rho \propto r^{-1}$ dependence in the center as the universal dark matter profile found by Navarro et al. (1996b), however with a finite total mass as the density in the outermost regions decreases as $\rho \propto r^{-4}$. The baryonic component is represented by analytic external potentials of a disk and a central point mass. We used the potential of an exponentially thin disk according to Dehnen & Binney (1998). Its strength depends on the ratio of the disk mass M_d to the disk scale length r_d. Following Navarro et al. (1996a), we started with a very large disk scale length and kept the disk mass constant throughout the simulation. The disk scale length is contracted linearly with time, where the contraction rate is a free parameter. Large contraction time scales compared to the dynamical time scales correspond to the adiabatic limit. In the limit of zero contraction time the halo will go through a phase of violent relaxation. The halo-disk system was allowed to relax after the contraction phase for several dynamical time scales. We applied a massive and a low-mass disk model with 20 % (MD) and 5 % (LD) of the total dark halo mass, and with a typical final scale length of 0.14 r_h.

In order to test the dependence on the concentration of the potential we used a softened point mass potential following

$$\Phi_p(r) = \frac{GM_p \arctan(r/r_p)}{r_p}. \tag{1.2}$$

Similar to the disk case we kept its mass M_p constant and shrank the smoothing length to a final value of $r_p = 0.03$ (test case PC). We also tested the case where r_p was kept constant and M_p was allowed to grow (PG). For all calculations we chose $G = M_h = r_h = 1$, where G is the gravitational constant. Simulations were performed with halos represented by N = 1×10^4, 8×10^4, 2×10^5 and 1×10^6 particles in order to test the dependence of the results on the numerical resolution. All model parameters are listed in Table 1.1. The gravitational softening length ϵ was chosen according to the criterium of Merritt (1996). We used a time step at least a hundred times smaller than the dynamical time scale we would expect at the half mass radius for each model. The timestep, adequate for the runs with the highest number of particles, was not enlarged for lower particle number runs. We used a newly developed tree code VINE (Wetzstein et al., in preparation) in combination with special purpose hardware GRAPE-5 (Kawai et al., 2000) at the MPIA, Heidelberg. The refined force accuracy criterium of Salmon & Warren (1994) guarantees that the absolute force error stays below the precision of the GRAPE hardware.

1.3 Results

The four top panels in Fig. 1.1 show the final density profiles of the contracted halos for two resolutions for the massive and the light disk, respectively (models LD1, LD2 and MD1, MD2). The error bars show the Poissonian error. The softening length is indicated with an arrow on each plot. In the innermost parts of the halo, i.e. $r \leq 2\epsilon$, the density is influenced by at least two effects: The softening length and fluctuations in the density due to small particle numbers. To show the effect of the fluctuations we plot the density profile of four consecutive dumps taken shortly after the contraction has been completed. This is important as the fluctuations sometimes exceed the 1 σ Poissonian error. At radii larger than two softening lengths the analytical approximation of BW84 gives a very good account of the matter distribution of the halo for every disk model. The two panels at the bottom of Fig. 1.1 show the point mass case which is also in very good agreement with the theoretical profile, independent of the way we grow the external potential. However, the density is somewhat lower than theoretically predicted inside the scale radius r_p.
Fig. 1.2 illustrates for the LD case that the agreement between numerical simulation and theoretical profile improves with increasing particle number, as we are able to probe deeper into the center of the dark matter halo.
In Fig. 1.3 we examine the response of the halo to an abrupt addition of the external potentials (models MDV, LDV and PV). The profile with the light disk (top left) still matches the theoretical curve. Even in the case of the massive disk (bottom left), the predicted density distribution agrees well with the numerical model although we find a somewhat lower density inside a radius of one disk scale length. Adding the point mass potential instantaneously (bottom right) leads to a density distribution that deviates strongly from the adiabatic prediction. The top right panel in Fig. 1.3 shows the time evolution of the 1% mass shell radius in each case. For the LD models the mass shells stabilize at more or less the same radius, though the detailed path of contraction is very different for LD2 and LDV. For the more centrally concentrated potential (PV) this is not the case. It stabilizes at radii further outside than in the adiabatic case. Consequently these density profiles are less concentrated in the center than in the adiabatic case.

1.4 Discussion

We showed that the adiabatic contraction approximation is valid at least in the case of a spherical dark matter halo and an axisymmetric disk. Let us stress that on a particle to particle basis even if we would have superposed a spherical perturbing potential, M(r)r is not conserved (apart from circular orbits of course). We demonstrate this in Fig. 1.4. We compare the conservation of the time averaged mean radius of a general orbit in a spherical potential and the conservation of the eccentricity of the same orbit, which is defined as $r_p * r_a/(r_a + r_p)$, where r_a and r_p stand for apoapse and periapse. The form of the orbit is a planar rossette and it fills an annullus in configuration space. So rather than a certain radius, the eccentricity is conserved well. This is a very old result of Jeans (1924) who examined the influence of mass loss on the orbit of a binary star system and derived that the eccentricity is an adiabatic invariant.
The theoretical solution for the fact that the ensemble of rossette orbits form a system with a M(r) as predicted by the formula of BW84 lies probaly in casting the form of the distribution function in dependence of pericenter and apocenter of the orbits, as has been done by Baes & Dejonghe (2002). However, this is not alleviating general concerns, as e.g. are dark matter halos sufficiently spherical. If they are very triaxial (Dubinski & Carlberg, 1991) or axisymmetric (Dubinski, 1994) other orbit classes (see following chapters) will appear which will not be spherically symmetric in configuration space. Adiabatic contraction of such orbits might even cause them to change their class Binney & Spergel (1984a). Resonant interaction between a rotating disk and the dark matter might cause the orbits change their actions (see Weinberg, 1994 and companion papers). It is an open question if due to dynamical friction infalling dense gas clumps can destroy the central cusp of NFW dark matter halo. Recently it some researchers pointed out that adiabatically contracted NFW halos predict to steep

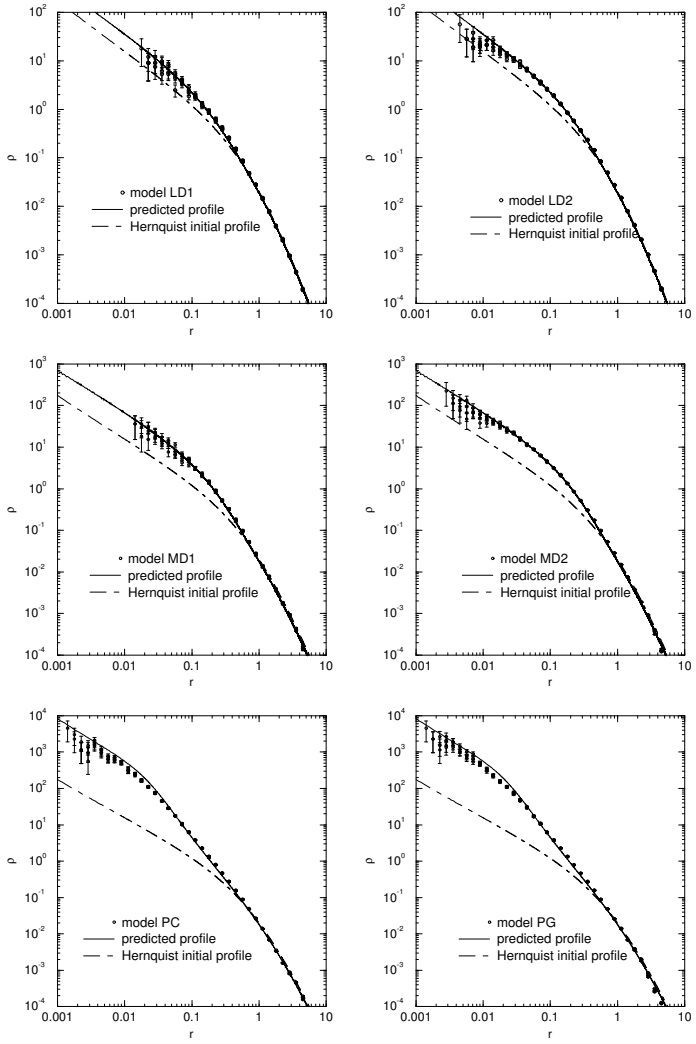

Figure 1.1: Final density profiles of contracted dark halos. The top two panels show the results for models LD1 and LD2, and the middle two for models MD1 and MD2. The bottom two panels show the results for the point mass. In the left panel the contracting scale length case and in the right panel the growing mass case is shown. Arrows indicate the used softening length.

rotation curves in the center even for HSB galaxies (de Jong et al., 2003). Future work should target aforementioned problems for the adiabatic approximation which we did not test with the addition of a mere analytical potential.

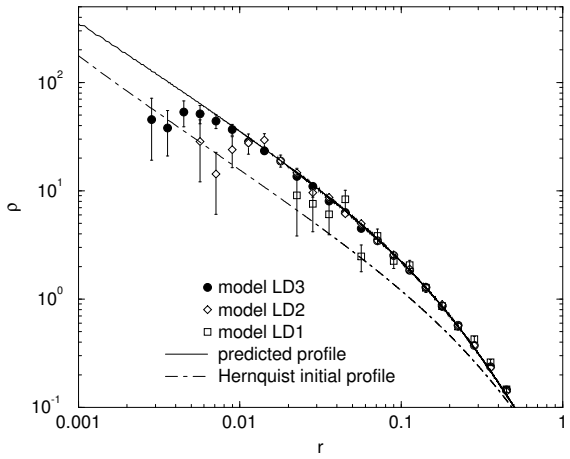

Figure 1.2: Final density profiles of LD1, LD2, and LD3 are shown to examine the effects of numerical resolution.

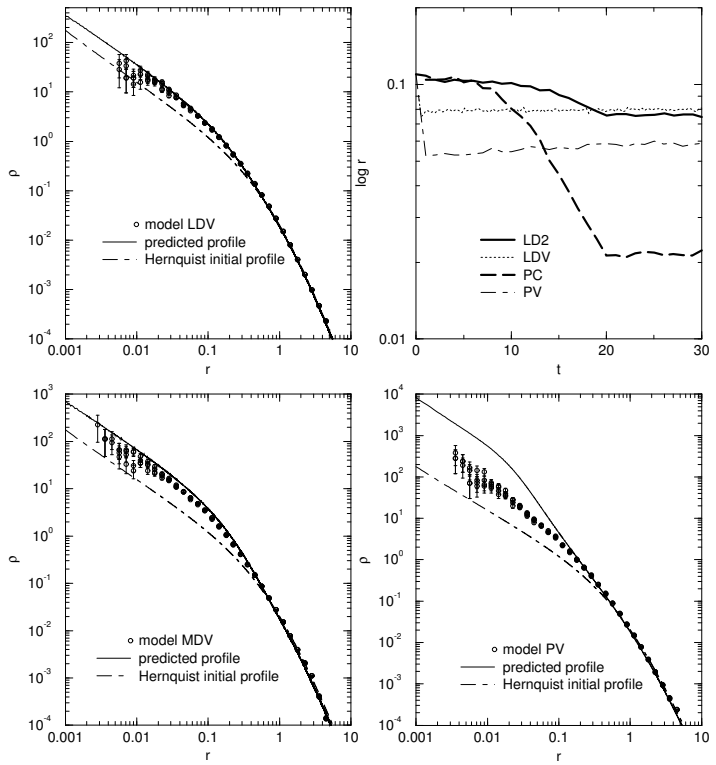

Figure 1.3: Final density profiles after abrupt addition of external potential. Top left, LDV; bottom left, MDV; bottom right, PV. In the top right panel, a comparison of the evolution of the 1models LD and P is shown.

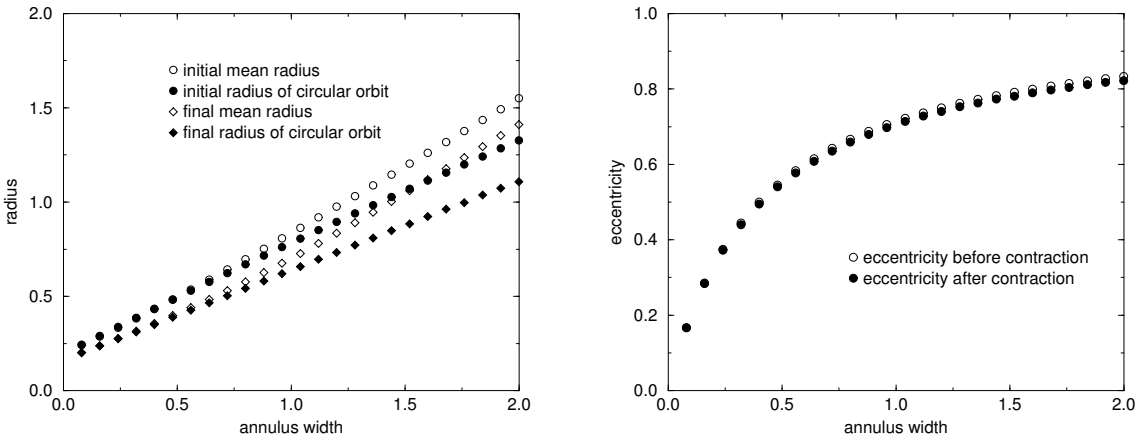

Figure 1.4: Quality of prediction of adiabatic approximation for the mean radius (left) and the eccentricity (right)

Chapter 2

Introduction to Orbit Classification in Merger Remnants

At the root of a collisionless stellar system lies its orbital content. It was not initially clear if this content consisted of regular orbits, regular meaning the orbit obeys as many isolating integrals as it has degrees of freedom. Indeed Contopoulos (1958) was the first to calculate numerically the orbits in the potential of an axisymmetric galaxy and expected them to be ergodic, but found them to be Lissajou figures which did not fill the whole phase space energetically accesible to them. This was because of the existence of a so called third integral, which needs to be calculated numerically in many models for a galactic potential.
This work is mainly concerned with the dynamics of elliptical galaxies, which are clearly three-dimensional objects and not axisymmetric thin disks like spiral galaxies. Initially they were also believed to be objects flattened by rotation, but it became clear that they are dynamically hot systems, which are pressure supported rather than rotationally supported.
Binney found that such systems could be either axisymmetric or triaxial. It was at first not known which orbital structure could be expected in triaxial mass configurations, until Schwarzschild (1979) calculated solutions for triaxial galactic model. He used a novel technique, which fitted numerically a set of orbits, also termed orbit library, to a given mass distribution. His findings implied that many potentials existed, also in the triaxial case, that were integrable. This important result means that we can use the theory of orbits rather than statistical mechanics for the examination of kinematical features in elliptical galaxies.
In the following years this method was applied to many different models to examine their orbital content. Stäckel potentials proved to be especially instructive for triaxial configurations, because all integrals of motion are analytic expressions in ellipsoidal coordinates as was shown by de Zeeuw (1985). He found that four major orbit families should dominate the content of elliptical galaxies: Box orbits, inner major axis tube, outer major axis tubes and short axis tubes. Subsequently many galactic models with Stäckel potentials were constructed by Statler (1987), Bishop (1987), Merritt & Hernquist (1991), Hunter & de Zeeuw (1992), Arnold et al. (1994) and others. It became clear that the solutions found for one model with Schwarzschild's method are not unique (de Zeeuw et al., 1987, Statler, 1987, Hunter, 1995). Many solutions are possible and it is unclear which orbit population would be preferred by nature for a given potential.
Many researchers took advantage of Schwarzschild's method and improved it to fit not only the mass distribution, but also the kinematical data of a galaxy (Richstone & Tremaine, 1984, Richstone & Tremaine, 1985, Richstone & Tremaine, 1988, Levison & Richstone, 1985), e.g. using the velocity dispersion as a constraint. But there is not enough information either in the deprojected surface brightness or the velocity dispersion to find a unique mass-to-light ratio for an observed galaxy (Binney & Mamon, 1982). If an elliptical galaxy is a fully relaxed object, we would expect that the distribution of stellar velocities follows a Maxwellian distribution and the line-of-sight-velocity profiles

are approximately Gaussian. With the advent of high resolution kinematic data more sophisticated analyzation methods showed that higher moments of the line of sight velocity distribution are important in elliptical galaxies (e.g. Rix & White, 1992, van der Marel & Franx, 1993, Kuijken & Merrifield, 1993). Following work attained better results in fitting distribution functions of different types to kinematical data (Gerhard, 1993, Qian et al., 1995, Rix et al., 1997, van der Marel et al., 1998). The constraints on the presence of dark matter in elliptical galaxies or of a black hole were further improved.
Elliptical galaxies were also found to exhibit distinct photometric features, as their isophotal shape. Bender (1988) and Bender et al. (1988) found that elliptical galaxies divide up in objects with boxy isophotal and disky isophotal shape. Interestingly galaxies with boxy isophotes have extensive X-ray halos of hot gas, rotate slowly, and have higher luminosity while disky galaxies are fast rotators, with low luminosity and have no X-ray halos. Apart from the isophotal shape disparity Bender et al. (1994) found correlations between the observable kinematical features of ellipticals like the third moment of the LOSVD and the isophotal shape parameter, for which there is no theoretical explanation.
Toomre & Toomre (1972) were the first to propose that ellipticals could origin from the mergers of two disk galaxies. Further N-body simulations of collisions of disk galaxies showed that they can mimick important features of elliptical galaxies, like kinematic misalignments, kinematically decoupled cores and isophotal twists (Barnes, 1992, Weil & Hernquist, 1996). In detail dissipationless mergers do not fit real ellipticals as reported by Cretton et al. (2001), who tried to fit the dynamics of 3:1 merger remnants to a sample of observed low luminosity elliptical galaxies. But a non-negligible amount of gas is found in the arms of spiral galaxies and has to be taken into account. Mergers with a dissipative component alleviate some of the problems of gas-free mergers (Barnes & Hernquist, 1996). The remnants tend to be more axisymmetric and less triaxial. They form disk-like components which were also found in elliptical galaxies. But Barnes (1998) proposed a solution for the isophotal shape of elliptical galaxies independent of a gaseous component by assuming that an unequal mass fraction of a major merger will result in a remnant with disky isophotal shapes. Naab et al. (1999) explored this hypothesis in detail and found that indeed equal mass and unequal mass mergers can account for the isophotal dichotomy of elliptical galaxies.
Several workers, most notably Bendo & Barnes (2000), examined the orbital content of merger remnants. They found that the center of the remnants is dominated by box orbits, while short axis tubes dominate at larger radii. Also in agreement with theory they found that x-tubes dominate in prolate remants. They also extracted higher moments of the LOSVD for selected remnants and showed a richness of features, but did not connect their results with a statistical analysis.

We find it striking that while the knowledge of the orbital content of analytical potentials and their fits to observational data has improved greatly, but we know very little about the orbital content of an important self-consistent formation mechanism of elliptical galaxies: mergers of disk galaxies. The aim of this work is not to improve agreement with features of real ellipticals, the solution to this problem would rather need more realistic simulations, e.g. the addition of gas, star formation or a black hole. We want to know what the orbital origin of the observed and the intrinsic features of the remnants are. A long-term goal then would be to connect the fine structure of an elliptical galaxy with its detailed formation history.
The first and foremost ingredient to such an analysis is a statistical relevant sample of mergers in two regards: merger symmetry and mass ratios between mergers. Such a sample was produced recently by Naab & Burkert, which includes 112 dissipationless merger remnants with mass ratios of 1:1, 2:1, 3:1 and 4:1 for close encounters and 48 1:1 and 3:1 merger remnants of wide encounters.
We will classify a representative sample of orbits in each merger remnant. The classification will be linked to triaxiality, isophotal shape, mean rotational velocities, velocity dispersion and higher moments of the LOSVD which we extract from the remnants by applying observational techniques. We will compare our orbital abundances with orbital fractions found in general triaxial potentials by the Schwarzschild method. The models which are represented by the merger remnants are at least as (if not more) realistic as e.g. Stäckel potentials. Global correlations are built to see if one orbit class or a combination of orbit classes can be accounted for certain structural and/or kinematical features.

In chapter 3 we will introduce the merger remnant sample. The classification technique and first tests are outlined in chapter 4 We will examine the correlation between shape and orbit classification in chapter 5. Basic kinematic features of classified orbits are checked in chapter 6. The connection between the isophotal shape and the orbital stucture and global correlations of the third moment of the line of sight velocity distribution are examined in chapter 7 and 8, respectively.

Chapter 3

The Merger Sample

3.1 Physical Setup

We follow the description of the sample as reported by Naab & Burkert. The merging spiral galaxies were constructed in dynamical equilibrium using the method described by Hernquist (1993). In all calculations used in this work the units are $G = M_d = r_d = 1$, where M_d is the mass of the more massive disk, r_d the scale length of the more massive disk and G is the gravitational constant. The disks are following an exponential law. At the center of each disk a spherical, non-rotating bulge with mass $M_b = 1/3$, a Hernquist density profile (Hernquist, 1990) with a scale length $r_b = 0.2r_d$ is added. The disk system is embedded in a live pseudo-isothermal halo with a mass $M_h = 5.8$, cut-off radius $r_c = 10r_d$ and core radius $\gamma = r_d$.

Merger mass ratios of 1:1, 2:1, 3:1 and 4:1 were calculated. The equal mass mergers have 80000 particles in each galaxy, 60000 in the disk and 20000 in the bulge. They decided to use twice as many halo particles than disk particles to reduce heating and instability effects in the disk components (Naab et al., 1999), i.e 120000 dark halo particles for each galaxy. This amounts to a total of 400000 particles. For the mergers with mass ratios $s\eta = 2, 3, 4$ the number of particles for the less massive collision partner are scaled down accordingly. The particle numbers of each simulation are summarized in Table 3.1. They assigned a disk scale length of $h = \sqrt{1/\eta}$ for the low mass companion as expected from the Tully-Fisher relation (Pierce & Tully, 1992).

3.2 Software and Hardware

The N-body simulations for the equal-mass mergers were performed by direct summation of the forces using the special purpose hardware GRAPE6. One force calculation for 400000 particles takes $\delta t \approx$ .11 seconds. The unequal mass mergers were simulated using the newly developed treecode VINE (Wetzstein et al., 2003) in combination with the GRAPE5 (Kawai et al., 2000) hardware. VINE uses a binary tree in combination with the refined multipole acceptance criterion proposed by Salmon & Warren (1994). This criterion enables the user to control the absolute force error which is introduced by the tree construction. We chose a value of 0.001 which guarantees that the error resulting from the tree is smaller than the intrinsic force error of the GRAPE5 hardware which is of the order of 0.1%. One force calculation with VINE and GRAPE5 for 400000 particles takes approx. 12 seconds.

They used a gravitational Plummer-softening of $\epsilon = 0.05$ and a fixed leap-frog integration time step of $\Delta t = 0.04$. For the equal-mass mergers simulated with direct summation on GRAPE6 the total energy is conserved, VINE in combination with GRAPE5 conserves the total energy up to 0.5%.

Table 3.1: Number of particles of different components in the merger simulation for different mass ratios

Mass Ratio	N total	N_{lum} total	N_{dark} total	N_{disk} massive	N_{bulge} massive	N_{dark} massive	N_{disk} light	N_{bulge} light	N_{dark} light
1:1	400000	160000	240000	60000	20000	120000	60000	20000	120000
2:1	300000	120000	180000	60000	20000	120000	30000	10000	60000
3:1	266666	106666	160000	60000	20000	120000	20000	6666	40000
4:1	250000	100000	150000	60000	20000	120000	15000	5000	30000

3.3 Orbital Geometry

The merging galaxies in the simulations approach each other on nearly parabolic orbits. A study of orbits of merging dark matter halos in cosmological large scale simulations by Khochfar & Burkert has shown that most of the merging halos are indeed on parabolic orbits. The first sample is started with an initial separation of $r_{sep} = 30$ length units and a pericenter distance of $r_p = 2$ length units (same parameters as e.g. Hernquist (1992). These are termed close encounters. The second sample has a pericenter distance of $r_p = 6$ length units termed distant encounters. The rest of the procedure of setting up the initial conditions is identical for both samples.
The inclinations of the two disks relative to the orbit plane were i_1 and i_2 with arguments of pericenter ω_1 and ω_2 (see Fig. 3.1).

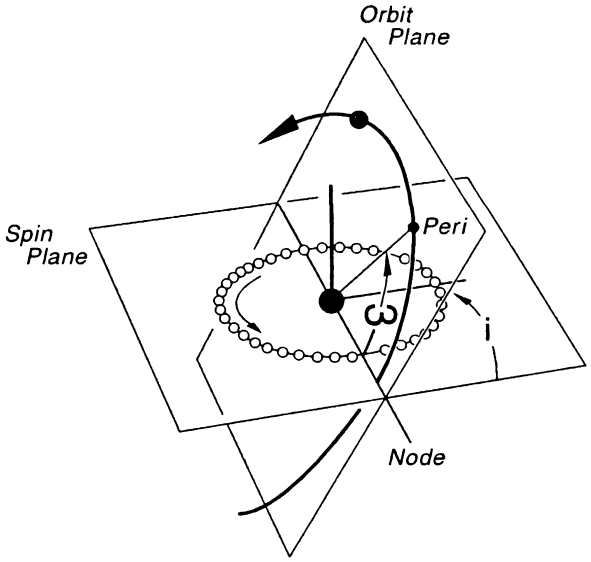

Figure 3.1: Illustration of the angles used to specify a certain merger symmetry.

In selecting unbiased initial parameters for the disk inclinations Naab & Burkert followed the procedure described by Barnes (1998). For the spin vector of each disk we defined four different orientations pointing to every vertex of a regular tetrahedron. The initial orientations we used translate to the following set of angles: For the first galaxy $i_1 = (0, -109, -109, -109), \omega_1 = (0, -60, 180, 60)$. The second galaxy has $i_2 = (180, 71, 71, 71), \omega_2 = (0, -30, 30, 90)$. These parameters result in 16 initial

Table 3.2: For unequal-mass mergers the first number indicates the orientation of the more massive galaxy as i_1 and ω_1, the second number indicates the orientation of the more massive galaxy as i_2 and ω_2.

Geometry	i_1	ω_1	i_2	ω_2	r_p	$r_{\rm sep}$
1/17	0	0	180	0	2 or 6	30
2/18	0	0	71	30	2 or 6	30
3/19	0	0	71	-30	2 or 6	30
4/20	0	0	71	90	2 or 6	30
5/21	-109	-60	180	0	2 or 6	30
6/22	-109	-60	71	30	2 or 6	30
7/23	-109	-60	71	-30	2 or 6	30
8/24	-109	-60	71	90	2 or 6	30
9/25	-109	0	180	0	2 or 6	30
10/26	-109	0	71	30	2 or 6	30
11/27	-109	0	71	-30	2 or 6	30
12/28	-109	0	71	90	2 or 6	30
13/29	-109	60	180	0	2 or 6	30
14/30	-109	60	71	30	2 or 6	30
15/31	-109	60	71	-30	2 or 6	30
16/32	-109	60	71	90	2 or 6	30

configurations for equal-mass mergers and 16 more for every mass ratio $\eta = 2, 3, 4$ where the initial orientations are interchanged. Following the simple hypothesis that the orientations of the merging disks are independent of each other and independent of their mutual orbital plane, every merger geometry has an equal probability to be realized (Barnes, 1998). The orbital parameters are listed in Table 3.2. In total 112 mergers of close encounters and 48 mergers of distant encounters were simulated, because only 1:1 and 3:1 mergers were calculated for distant encounter symmetries. For all simulations the merger remnants were allowed to settle into equilibrium approximately 8 to 10 dynamical times after the merger was complete. Then their equilibrium state was analyzed.

Chapter 4

Orbit Classification in Merger Remnants

The realm of orbits can be divided between the regular and the chaotic orbits. An orbit is called regular, when it conserves at least as many isolating integrals as it has degrees of freedom Each integral confines the regular orbit to a certain shape in configuration space. The four major orbit families in triaxial potentials are widely known and named according to their shape box orbits, inner major axis tubes, outer major axis tubes and short axis tubes. For chaotic orbits (sometimes called irregular, not to be confused with irregular families) this is not true. As the chaotic orbit only obeys one integral of the motion, the energy integral, it will visit the whole phase space allowed to it. After a long enough time it will fill a spherical volume. The relative importance of both types of motion in stellar dynamics is not yet clear. Dynamical studies (Gerhard & Binney, 1985) showed that the addition of cusp and/or a black hole to a galactic potential can introduce chaos into the center of a galaxy. It is even argued that stochasticity (Merritt & Fridman, 1996) drives most elliptical galaxies towards axisymmetry and that it limits the shape parameters accessible to self-consistent models (Merritt, 1997). On the other hand there are triaxial elliptical galaxies which have preserved their shape for many dynamical times (see Statler & SAURON Team (2003) for a recent observational result and Hunter (2001) for a recent theoretical review). Chaos must not have played a major role in those galaxies. The merger remnants devoid of any black holes do keep their shape. In our analysis we concentrate on regular orbits as the main building blocks of galaxies.

If one is convinced that regular orbits play an important role in stellar dynamics a few classification methods are open for choice. One of the oldest methods to classify orbits was envisioned by Henri Poincare, the so called surface of section. In principle it is possible to classify orbits in 2 dimensions with this method. At a given cut through the trajectory, normally at the 0-surface of one coordinate, the value of the other coordinate and its corresponding velocity are recorded. In other words a surface of section is a cut through the phase space torus of the orbit. While visually beautiful it is tiresome to classify orbits by inspection only. A practical impossibility is that SOS of 3-dimensional orbits are 4 dimensional (the phase space coordinates of the other two coordinates) and cannot be visualized in a simple way. Binney & Spergel (1984b) pioneered an alternative way to reconstruct the phase space torus of a regular orbit, which they termed spectral analysis. We will outline why we chose this method and how the results relate to other methods of choice.

The problem at hand is that we want to classify the orbits of an N-body object much coarser grained than real galaxies in nature. It would be desirable to analyse the orbits 'on the fly' while conducting the N-Body simulation. But this is out of the question for practical reasons. The dump frequency would be too high to be useful for a powerful classification algorithm. We chose to extract the potential and forces by an Self Consistent Field code (SCF hereafter, see e.g. Hernquist & Ostriker, 1992, hereafter HO92) and integrate the orbits with a high order, high accuracy Runge-Kutta Integrator. We will introduce shortly the major orbit families existing in triaxial potentials, explain the numerical methods

to classify the orbits in a merger remnant and test the results with an alternative classification method.

4.1 Numerical Methods

4.1.1 Spectral Dynamics

The quasi-periodicity of a regular orbit allows to expand the motion in a Fourier series

$$x(t) = \sum_{l,m,n} X_{(l,m,n)} cos(\omega_{x(l,m,n)} t + \chi_{(l,m,n)}) \tag{4.1}$$

$$y(t) = \sum_{l,m,n} Y_{(l,m,n)} cos(\omega_{y(l,m,n)} t + \psi_{(l,m,n)}) \tag{4.2}$$

$$z(t) = \sum_{l,m,n} Z_{(l,m,n)} cos(\omega_{z(l,m,n)} t + \phi_{(l,m,n)}) \tag{4.3}$$

in three dimensions, where l, m and n are integers and χ, ψ and ϕ are constant phases. The ωs are linear combinations of the base frequencies.

$$\omega_{x,y,z,(l,m,n)} = l\omega_1 + m\omega_2 + n\omega_3, \tag{4.4}$$

where ω_1, ω_2 and ω_3 are the base frequencies also sometimes termed fundamental frequencies in the literature. The shape and family of the orbits are determined by two factors.

- 1. The resonance (or lack of resonance) between the quasiperiodic motion in x, y and z
- 2. The number of independent base frequencies

An orbit is resonant when there is a non-trivial choice for p and q such that

$$p\omega_x + q\omega_y = 0, \tag{4.5}$$

or ω_x and ω_y are said to be commensurabel. The resonance determines the main family of an orbit. A tube orbit will always have a 1:1 resonance, which will give this orbit a definite sense of rotation around the minor or the major axis of the potential. If an orbit has a 1:1 resonance in the motion in y and z direction it will be termed x-tube (or minor axis tube). Analogously if it has a 1:1 resonance in the motion in x and y direction it is called a z-tube (minor axis tube). Y-tubes are instable in general triaxial potentials (Heiligman & Schwarzschild, 1979) except in the special case of a spherical potential. An orbit can have either no resonance, one resonance or three resonances. Of course, there can not be two resonances because by transitivity if ω_x is resonant with ω_y and ω_y is in resonance with ω_z then ω_x is also resonant with ω_z.
The second point is not so easily understood. The base frequencies determine what we could call the topology of an orbit. If all spectral lines of an orbit (in all three degrees of freedom) can be represented by one frequency, it will be a closed orbit, regardless if its resonance determines the orbit as a box or a tube. If three frequencies are needed, the orbit will be termed open. The rossette orbits is a 2D analogue of such an orbit. In general spherical potentials, the rossete will not close on itself to form an elliptical orbit, but will precess. The test star will densely fill a ringlike structure. For two base frequencies there is no real 2D analogue. These orbits will move on thin two-dimensional 'walls' in configuration space, which can take complex forms. If now there is a line in the Fourier spectrum which is not commensurabel with three base frequencies it must be the fourth base frequency. The orbit is termed irregular, or chaotic. The extra frequency causes the orbit to diffuse in phase space, i.e. it is not bound on a phase space torus.
Carpintero & Aguilar (1998) (henceforth CA98) devised a code which automatically calculates the Fourier spectrum of an orbit and classifies it according to the scheme outlined in Table 4.1. The input consists of the positions and corresponding times. The input must be equally spaced in time. The

spectra is calculated by a fast Fourier transform. FFT work only with time series which are a power of 2, in our case 4096 dumps. The five most prominent lines are extracted and the orbit classified. We refer the reader for mathematical details of the line extraction to CA98. See also Hunter (2002) for a detailed discussion on harmonic analysis.
The code was tested on the singular, triaxial logarithmic potential first analysed by Miralda-Escude & Schwarzschild (1989) and found a very good agreement. There are several features of the code which makes it attractive for use on N-Body objects.

- Although we correct the particle positions and velocities by finding the center of mass for an ever smaller shell of particles, this correction may not be completely correct. For certain orbits the spectral code can find a non-zero amplitude in the 0-frequency slot, which is non-physical, of course. It automatically translates the orbit until the 0-frequency slot is nullified. This works because the rest of the spectrum is unaffected in such a translation.

- The code assumes that the x-axis is aligned to the major axis of the system. However, merger remnants are known to have twists. Especially tube orbits need to be aligned with the correct axis to classify them correctly. But the code can compensate for small to intermediate twists as long as the axis fits through the hole of the tube orbit (i.e. with large angular momentum). Orbits with small holes are lost more quickly (Carpintero, private communication). Those will not be very frequent though as the z-tubes are left over of one of one the disks and did not come near to the center. We tested this by purposefully inclining a disk by 30 degrees. The algorithm still classified 80 % of the orbits as z-tubes. We will discuss it in more detail below, because it explains the robustness of our results. Note, that if x and z-axis are exchanged the algorithm breaks down. X-tubes are classified as z-tubes and vice versa. 90 degree twists are (luckily) not observed in the remnants.

- If the potential is oriented wrongly this does not matter for loop orbits, but box orbits are not rotationally invariant. The code tests this by rotating the orbit, when the classification indicated a box orbit. If the spectra changes and it was initially classified as tube, it reclassifies the orbit according to the maximum amplitude found.

- The accuracy of the extraction of the Fourier lines is given one part in 10^{-4}. We are aware that there are algorithms which extract the base frequencies with higher accuracy (see e.g. Laskar, 1993, Hunter, 2001), such as Hanning filters. But the accuracy of the extraction should not be overestimated in the context of N-body merger remnants. The potential itself is coarsely sampled. These extraction methods are best applied to analytical potentials, which are resolved to the machine limit.
  CA98 restrict themselves to the extraction of the five most prominent lines in each coordinate and take only lines into account which have at least an amplitude 0.02 of the most prominent in the respective coordinate. When the code extract two neighbouring lines it must decide if they are the same line to within the desired accuracy.

$$\frac{a-b}{a+1} < \epsilon\Delta, \tag{4.6}$$

  where a and b are the frequencies in question, Δ is the difference in frequency space and ϵ is the parameter to fix. CA98 found a value $\epsilon \approx 0.25$ as a good compromise, which we adopted. The code therefore gives a healthy balance between sophisticated extraction of lines and overly exagerrated accuracy, which will render most orbits to be (spuriously) chaotic.

- Automatism. We are planning to classify between 40000 and 64000 orbits in each merger remnant. The sample contains 150 mergers. In the course of this work an approximate amount of 7,5 million orbits will have been classified. Any classification scheme has to be fully automatic and well tested. The code of CA98 is the only public available code, which we know of, suitable for this task.

Table 4.1: Classification scheme. We follow the nomenclature of CA98. The topology is determined by the number of base frequencies. A 1:1 designates the resonance responsible for a rotation around the x or z-axis. n,l,m designate other resonances for each degree of freedom. π stands for irrational divisor, or simpler, no resonance in one coordinate direction.

topology	n:l:m	name	Independent frequencies	Resonances
open	π:m:n	resonant box	3	1
open	π:1:1	z-tube	3	1
open	π:1:1	outer x-tube	3	1
open	π:1:1	inner x-tube	3	1
open	l:m:n	resonant box	3	3
open	l:1:1	z-tube	3	3
open	l:1:1	outer x-tube	3	3
open	l:1:1	inner x-tube	3	3
thin	π:m:n	resonant box	2	1
thin	π:1:1	z-tube	2	1
thin	π:1:1	outer x-tube	2	1
thin	π:1:1	inner x-tube	2	1
thin	l:m:n	resonant box	2	3
thin	l:1:1	z-tube	2	3
thin	l:1:1	outer x-tube	2	3
thin	l:1:1	inner x-tube	2	3
closed	l:m:n	resonant box	1	3
closed	l:1:1	z-tube	1	3
closed	l:1:1	outer x-tube	1	3
closed	l:1:1	inner x-tube	1	3
-	π: π: π	box	3	0
-	-	irregular	>3	

4.1.2 Self Consistent Field Methods

The self-consistent field approach (SCF hereafter) stems from the fast multipole algorithms developed in quantum mechanics, also known as Hatree-Fock methods. The method is also applicable on the gravitational N-Body problem. The aim is to solve Poisson's equation by expanding the density and the potential in a bi-orthogonal basis set. Poisson's equation reads as

$$\nabla^2 \Phi_{nlm}(r) = 4\pi G \rho_{nlm}(r) \tag{4.7}$$

and the basis set

$$\rho(r) = \sum_{nlm} A_{nlm} \rho_{nlm}(r) \tag{4.8}$$

$$\Phi(r) = \sum_{nlm} A_{nlm} \Phi_{nlm}(r), \tag{4.9}$$

where n, l and m are the 'quantum' numbers or the spherical harmonics. Analogously n is the number of radial expansion terms, l and m are the number of angular expansion terms, with m=-l..+l. The

coefficients can be calculated from these formula when the position and the masses of the particles are known (for a detailed description of the calculation of the expansion coefficients see HO92). When the coefficients are known the acceleration can be calculated as following

$$a(r) = -\sum_{nlm} A_{nlm} \nabla \Phi_{nlm}(r), \tag{4.10}$$

where $\nabla\Phi_{nlm}(r)$ must be calculated analytically in advance. This implies that we have to make a choice of the lowest order term of potential expansion, i.e. Φ_{000}, which should resemble the overall structure of the N-body object. Rather than particles interacting directly the gravity is represented in a mean-field sense. Direct collisions which are inhibited in traditional N-body codes by the smoothing length are not possible in a SCF code. It is truely collisionless. Although the concept of a smoothing length is not needed, the finite number of expansion coefficients introduces some noise. SCF codes scale with O(NlogN), but as we are treating the remnant as a static potential it just scales with N. A code to calculate the coefficients for a given particle distribution was kindly provided by Shunsuke Hozumi.

4.1.3 Integration

We use an explicit Runge-Kutta-Integrator of 8th order developed by Hairer et al. (1987), called DOP853. It produces a dense output, dense meaning it interpolates the coordinates and velocities at given equal distant time intervals, although it is an adaptive time-step scheme. As discussed above the FFT needs an input at equal-distant time steps. An adaptive scheme is necessary because the dynamical times become rather large in the outer parts of the remnant. The CPU time of the integration is proportional to the tolerance allowed on the energy conservation of the orbit. We restricted the energy conservation to smaller than one part in 10^{-8} and still achieved an integration CPU time of less than a second for approximately 200 dynamical times. We can effectively reduce small scale noise (due to the finite number expansions coefficients, as we have no particle noise any more) which could otherwise wreak havoc on the line extraction.

4.2 Tests on Merger Remnants

We introduced the numerical ingredients of our codes. How they play out when they are applied to merger remnants is another question. We had to test rather extensively to make sure that the orbits are classified correctly. The test (and the production) runs needed to be reduced in an effective. The procedure is explained step by step in the following:

1. The merger remnant is translated to its center of mass and rotated such that the major axis is aligned with the x-coordinate axis, the intermediate axis is aligned with the y-coordinate axis and the short axis is aligned to the z-coordinate axis calculated close to the half mass radius of the merger remnant.

2. The initial velocities and positions are taken from the last dump of the merger remnant

3. The expansion coefficients are calculated and saved to a file

4. The main code reads the coefficients only once, as the potential is static

5. The trajectory is evolved for a fixed time (3.25 Gy). Accelerations are taken from the SCF part of the code. Exactly 4096 equal distant points in time of the trajectory are saved

6. The spectral code Fourier transforms the time series and classifies the orbit

7. The rotation numbers, i.e. ω_x/ω_z and ω_y/ω_z , the classification and the number of completed periods are saved. Go to step 2. for the next orbit.

4.2.1 Choice of Basis Set

There are two commonly used basis sets in the literature: the Clutton-Brock basis set (Clutton-Brock (1973) from here on CB) and the Hernquist-Ostriker basis set (HO92). As mentioned, the lowest order expansion term should be able to fit the overall structure of the object in question. The CB basis set is the well known Plummer sphere

$$\rho_{000} = \frac{3}{4\pi}\frac{1}{(1+r^2)^{5/2}} \tag{4.11}$$

$$\Phi_{000} = -\frac{1}{(1+r^2)}, \tag{4.12}$$

and the HO basis set is the Hernquist sphere

$$\rho_{000} = \frac{1}{2\pi}\frac{1}{3}\frac{1}{(1+r)^3} \tag{4.13}$$

$$\Phi_{000} = -\frac{1}{(1+r)}. \tag{4.14}$$

These two models show very different behaviour in the center. While the Plummer sphere has a shallow core, the Hernquist sphere is cuspy with $\rho \propto r^{-1}$. Normally the HO basis set should be the choice for dense objects like the merger remnant, although they have a small core because relaxations and smoothing length affect the center mostly. We apply both basis sets to the same merger remnant: 1:1 with symmetry 10. It is a very prolate merger remnant and should show a significant amount of x-tubes. We use the same number of expansion terms n=6 and l=4. The result is surprising. While the results attained with the CB basis set are showing a variety orbits, tubes and boxes alike, the HO calculations just show box orbits (mainly resonant boxes). Such a configuration cannot be stable After eliminating possible trivial mistakes, we tentatively conclude that there is a incompatibility between the spectral code and the HO basis set. The reason might be that the forces of the Hernquist sphere do not go to zero in the center. There is a residual radial force of $f_r(0)$=-1. The spectral code explicitly assumes that the potential minimum is centered at the coordinate center. The radial force of the Plummer sphere does smoothly go to zero. Hozumi (1997) examined the phase space structure of the core violently relaxed uniform density sphere. He finds significant differences between a direct phase space code and results obtained with the HO basis set and good agreement with the CB basis set. We will use the CB basis set throughout this work. In the future the results should be tested against more sophisticated methods like numerical basis sets introduced by Weinberg (1999).

4.2.2 Dependence on Number of Expansion Terms

A good balance between representing the remnant and on the other hand not adding too much small scale noise to the orbit integration has to be found. We will use more radial than angular expansion terms. A high number of l is suitable for very flattened systems like disks, but our remnants have triaxial shapes. We adopt the cases (n=6, l=4), (n=8, l=6) and (n=10, l=8). Table 4.2 shows that as expected the number of chaotic orbits increase with the number of expansion coefficients. The z-tubes seem to be unaffected, while the outer x-tubes gain and inner x-tubes loose in numbers. The increase in chaotic and in not classified orbits is compensated by a drop of the box orbit fraction.
We have to bring back to mind that all orbits of N-Body calculations are chaotic. The SCF extraction is precisely used for smoothing the potential to assign an orbit to a class it would most likely belong, if it would not be chaotic. Increasing the number of expansions terms would be counterproductive, because it reintroduces small scale noise. It is understandable that a normal box orbit, which has no resonances, will be more prone to spurious frequencies, which will render it chaotic. Also they are more closer to the dense center (of course they form the center, this is an ambiguous formulation), in which the potential gradient is steeper and causes scattering. Similarly the inner x-tubes are closer to the center then their sister family of outer tubes and lose proportionally more family members.

Do we gain any knowledge from increasing the number of expansion terms? Not really, only that orbits which belong to the center are more chaotic than orbits which live further outside. With this in mind the family proportions are not changing dramatically.
We will therefore choose the lowest number of expansion terms n=6 and l=4. On the practical side this is a convenient choice, as the computation time of the accelerations increases with the number of expansion terms.

Table 4.2: Classification results for different choices of expansion coefficients

(n,l)	Resonant Box	Z-Tube	Inner X-Tube	Outer X-Tube	Box	Irregular	Not Classified
10,8	0.060	0.051	0.210	0.184	0.268	0.106	0.122
8,6	0.059	0.052	0.219	0.168	0.319	0.082	0.101
6,4	0.061	0.052	0.256	0.151	0.358	0.050	0.071

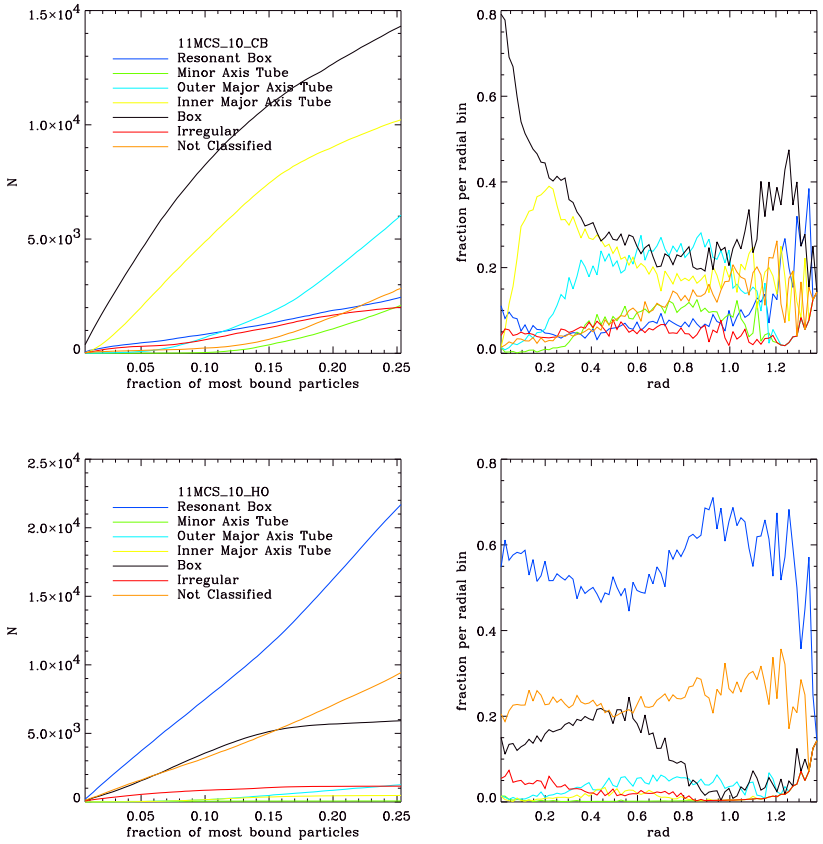

Figure 4.1: Comparison of classification results from different basis sets. Top Graph: Calculations with CB basis set. Bottom Graph: Calculations with the HO basis set. Left panel each graph: Cumulative distributions of orbit classes with binding energy. Righ Panel both graphs: radial distribution of orbit classes normalized for each radial density bin.

Table 4.3: Classification results for different choices of alignment

Particle Fraction	Resonant Box	Z-Tube	Inner X-Tube	Outer X-Tube	Box	Irregular	Not Classified
0.2	0.063	0.051	0.145	0.253	0.340	0.069	0.079
0.3	0.061	0.051	0.149	0.252	0.355	0.057	0.075
0.4	0.061	0.052	0.151	0.256	0.358	0.050	0.071
0.5	0.064	0.051	0.147	0.251	0.343	0.064	0.081
0.6	0.065	0.059	0.164	0.229	0.317	0.076	0.094

4.2.3 Alignment of Major Axis

We discussed already that the code is capable to compensate significant twists and inclinations of the analysed N-Body object. Table 4.3 quantifies this for the merger remnants. The merger remnant used in the tests is very prolate in the center ($T \approx 1.0$), but becomes more triaxial outwards($T \approx 0.5$). We calculate the inertial axis of the remnant for the 0.2, 0.3, 0.4 ,0.5 and 0.6 fraction of the most bound particles. The remnant is rotated on these axis and the classification started. The agreement is impeccable. The scatter of the results is very small. However, beyond the 60% fraction the alingment is lost and the number of not classified orbit rises exponentially. The remnant has no clear shape anymore, and leftovers of the tidal arms are ruining the alignment.

4.2.4 Sign Change of Angular Momentum

It is desirable to test our classification method against another classification method. Following Barnes (1992) we record each instance when the sign of one component of the angular momentum changes at a time dump. The simple idea is that a tube orbit never changes its sense of rotation in a static potential. X-Tubes should not change the sign of their L_x component, z-tubes do not change the sign of the L_z-component, all other orbits are boxes. The short-comings of this scheme are obvious. Neither can we distinguish between inner and outer major axis tubes, nor can we detect any resonances. This is the most trivial method by far, however, it offers a good sanity check when one of the more sophisticated methods might go astray. In Figure 4.2 the statistics for the test remnant are shown (64000 orbits in total).

- Both types of box orbits change the sign of the angular momentum of all components, as expected. There is a difference in the histogramms of the L_z which is peaked for the resonant orbits.
- The majority of the z-tubes do not change the sign of their L_z component. About 10% do change their sign. As the potential is not perfectly aligned to the principal axes, the z-tube might rotate slightly around the coordinate z-axis. Such an inclination will cause the orbit to change its sign only for the particular coordinate sytem we chose, when we rotated the merger remnant.
- The inner and the outer x-tubes also show the desired behaviour and do not change the sign of the L_x component. Interestingly the L_y and the L_z component histograms show a double peak for the inner x-tubes and an exponential drop off for the outer x-tubes. Maybe this fact can be exploited for a circumvention of the spectral code.
- The irregular orbits show a low contamination of x-tubes and z-tubes (few hundreds)
- The 'not classified' category shows a significant contamination of x-tubes and a low contamination of z-tubes. For statistical reasons it would be worrisome if one type of orbit is more often misclassified than another. But if we calculate the relative fractions between misclassified

tubes and correctly classified tubes, we see that 6,8 % of the x-tubes would have been recovered by a simple angular momentum change code and 6,1 % of the z-tubes. The conclusion is that orbits which are intrinsically more abundant in a merger remnant are proportionally also more often misclassified. We will show in the following chapter that the not classified category shows no correlation with fundamental properites of a merger remnant and is treated as background noise.

4.2.5 Orbit Envelopes

We have talked now in detail about abstract poperties of classified orbits in merger remnants, but sometimes seeing is believing. The location of a 'star' in a galaxy depends on which orbit family it belongs to. We will expect box orbits to be concentrated towards the center and z-tubes will circulate in the x-y plane. An individual orbit will fill a negligible volume, but the entire population of z-tubes can make up a disk. The isodensity lines of a sample of orbits will not be shapeless but reflect the shape of the orbit family or in other words the family forms an envelope. Such envelopes have been plotted by Statler (1987), who examined the orbital content of triaxial potentials (see next chapter). The initial positions are known from simulations and as we know the assigned classification for each particle, we can visualize these subsets of particles for better understanding. We do not produce 3D plots, as configuration space is still too coarsely sampled to render a smooth 3D plot. Instead we project the densities onto the three principal planes. We will take them from different merger remnants this time, because a single merger remnant has not enough particles belonging to all four major orbit families to give a smooth picture. The projections of the samples of the major orbit families are compared to the envelopes produced by Statler in the following figures.

- The resonant box orbits show a strong dent towards the center in their x-y and and x-z projections. This reflects their steep approach towards the center of the potential. The normal boxes show this behaviour only vaguely. As the orbits do not follow any resonances there is also no clear shape that they could support.
- The z-tubes can be recognized by the projection on the x-y plane. It is round and has a hole in the center. This reflects their centrophobic nature. Because they have significant angular momentum they will not approach close. The other two projections show that the 'disk' is rather puffy and extends to high latitudes.
- Also the inner and outer x-tubes divide up nicely. Both exhibit a hole in their y-z projection, but inner x-tubes wind along the major axis and have an elongated shape, while the outer x-tubes extend very little in x-direction.

4.3 Conclusions

We have shown that orbit classification in merger remnants is possible with a spectral classification method and an SCF method for the reconstruction of the N-Body potential. The agreement with results from a simple classification based on the sign change of angular momentum has an error margin between 5% to 8%. Additionally we can distinguish resonant orbits, both families of the x-tubes and different orbit topologies. The sensitivity on the choice of the alignment of the remnant is negligible (if the axis are not measured in the very outer parts), an increase of the number of expansion terms (both radial and angular) increases the amount of noise and hence the amount of chaotic orbits. An low number of expansion terms is chosen n=6 and l=4. Finally the form of the envelope formed by the configuration space of an orbit family agrees well with the envelope shapes as expected by theory.

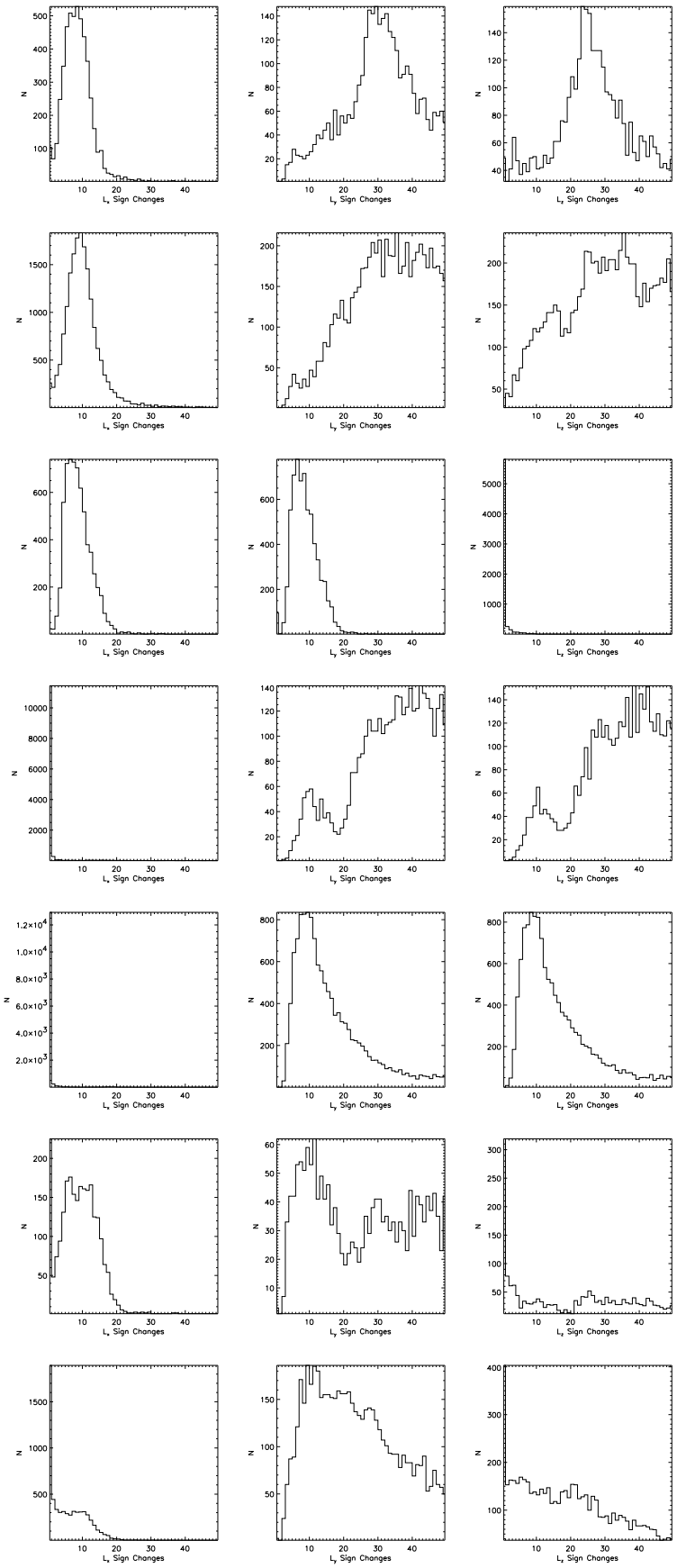

Figure 4.2: Histograms of the number of angular momentum sign changes of each classification category as attained by the spectral code. From top to bottom: Resonant Boxes, Box Orbits, Z-Tubes, Inner X-Tubes, Outer X-Tubes, Irregular Orbits and Not Classified.

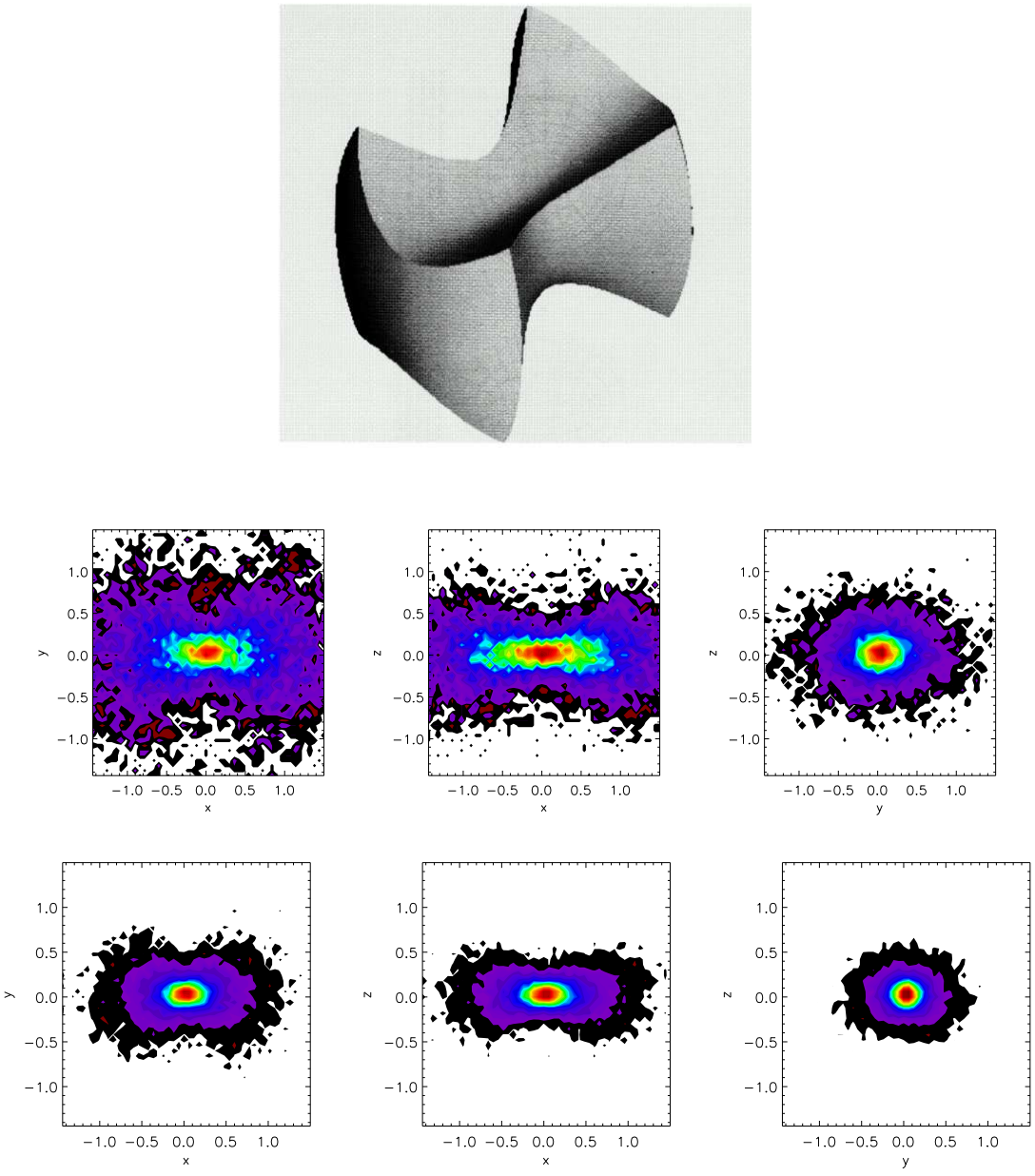

Figure 4.3: Top: Envelope of box orbits. Middle: Projection of resonant box orbits. Bottom Projections of non-resonant box orbits in merger remnants

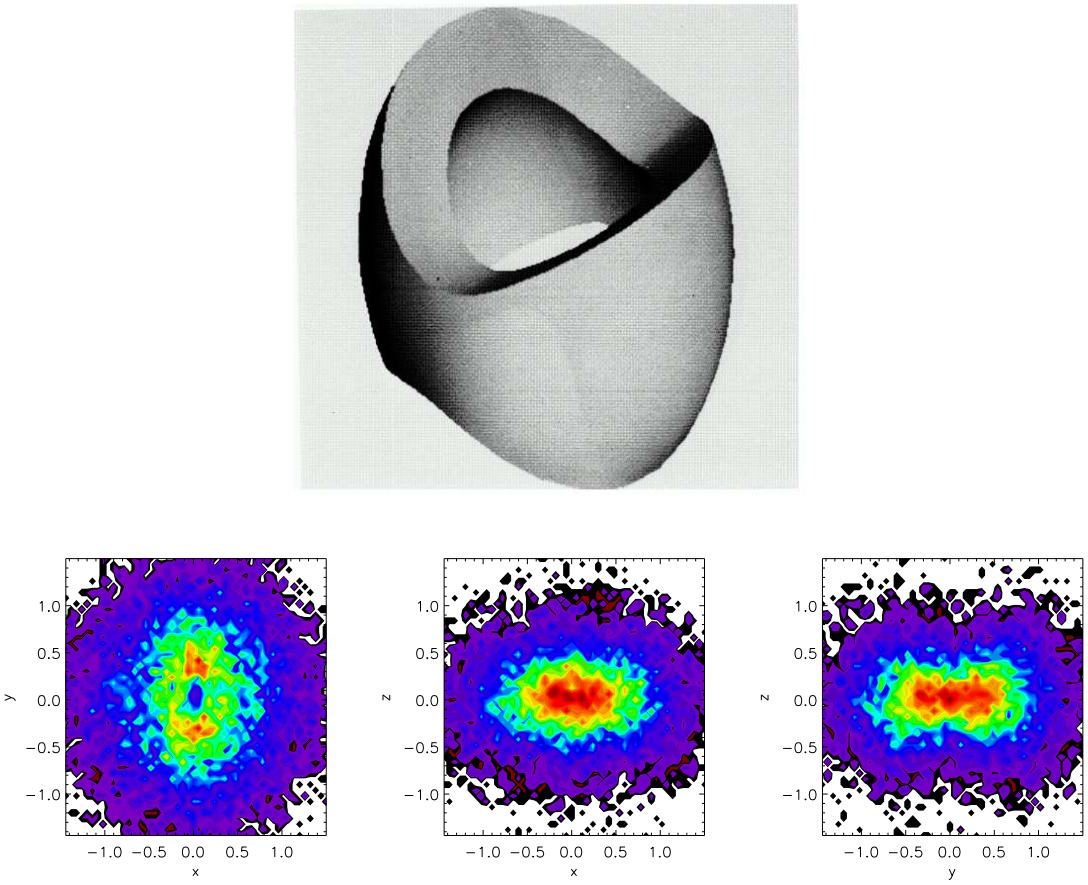

Figure 4.4: Top:Envelope of z-tubes Bottom: Projections of z-tubes in merger remnants

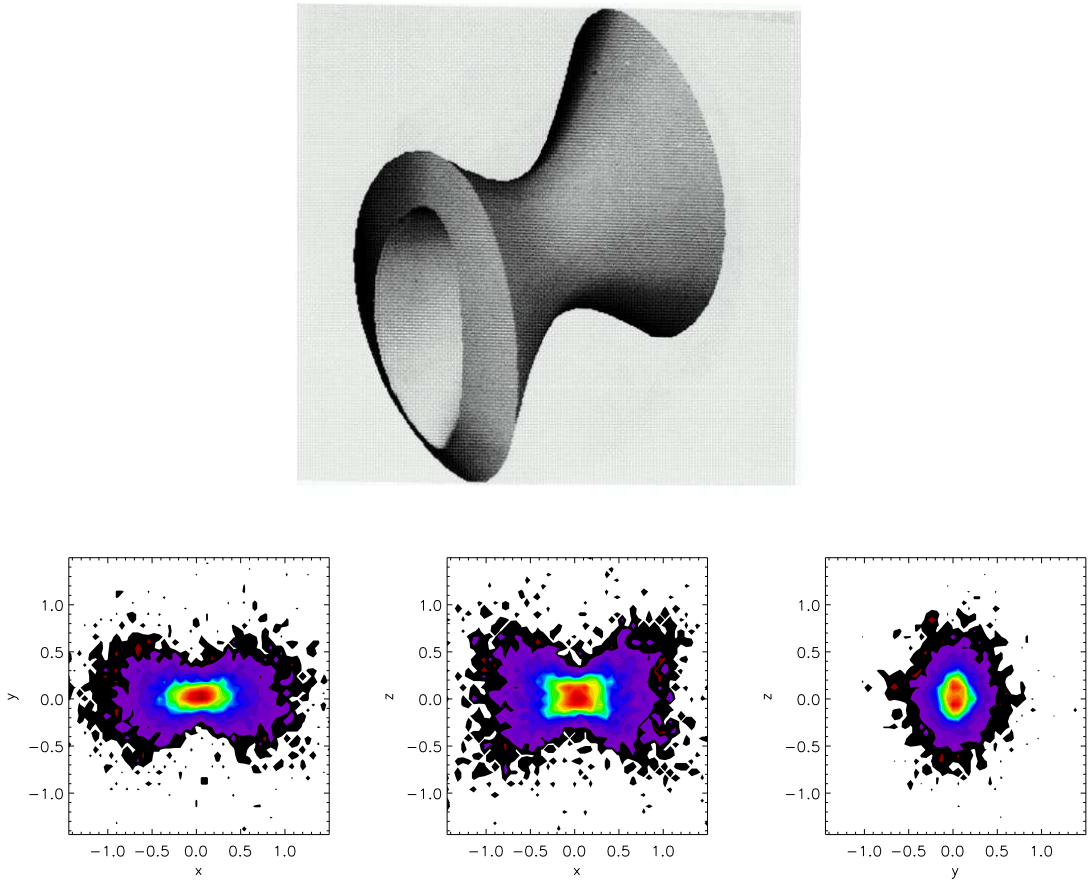

Figure 4.5: Top: Envelope of inner major axis tubes. Bottom: Projections of inner major axis tubes in merger remants

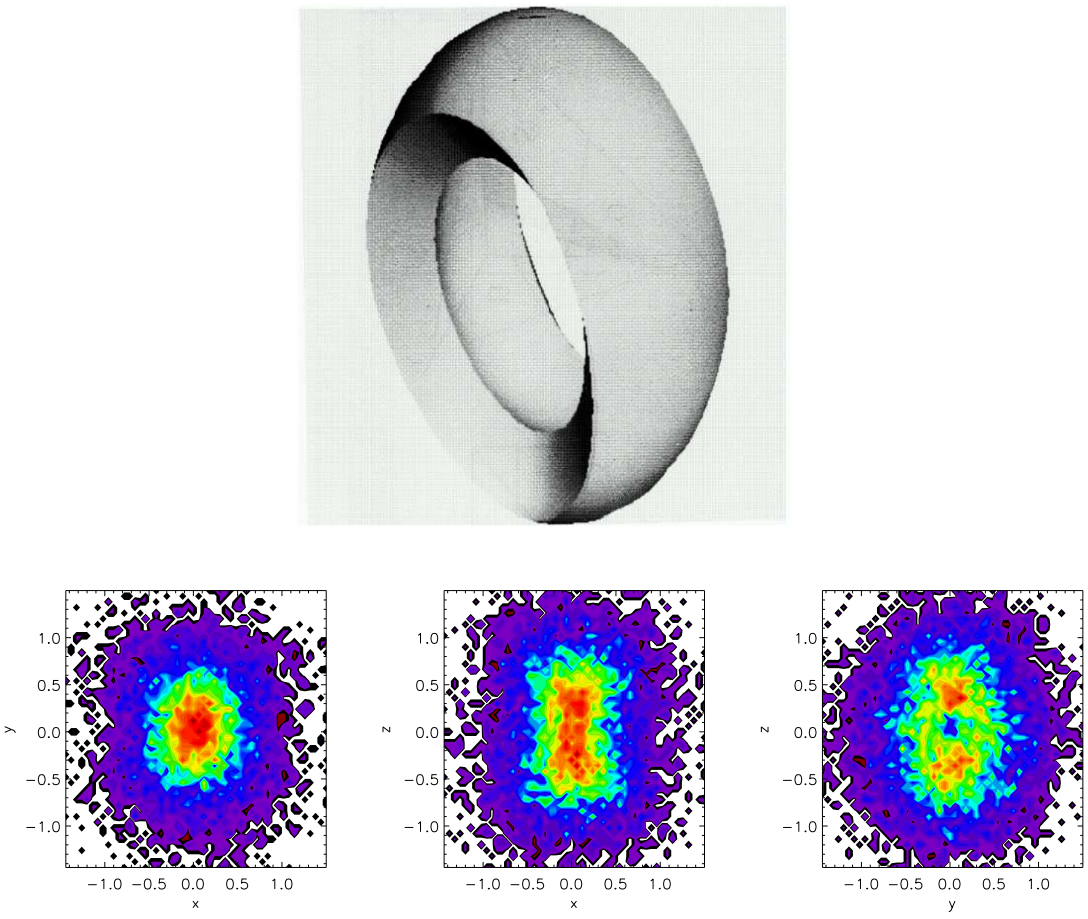

Figure 4.6: Top: Envelope of outer major axis tubes. Bottom: Projections of outer major axis tubes

Chapter 5

The Orbital Structure and the Shape Parameters

The intrinsic shape of elliptical galaxies is an outstanding problem since Hubble's times. It is an ill-determined problem as by the projection on the sky the information of the true shape is lost. Hubble (1926) classified the 'elliptical nebulae' according to the ratio of their apparent minor and major axis, defining the ellipticity (a-b)/a. As long as elliptical galaxies were assumed to form an oblate spheroidal population originated from a monolithic collapse of a gas cloud, there was not a big interest in their true shape. When it was shown that elliptical galaxies rotate too slowly to account for their flattening (Bertola & Capaccioli, 1975), the question rose again. They are rather dynamically hot systems. Binney (1978) suggested that the flattening is produced by the anisotropy of their velocity distributions. This would be entirely possible in a triaxial or an axis-symmetric potential. Statistical methods (Binggeli, 1980) show that the shape distribution of elliptical galaxies is inconsistent with a pure population of oblate spheroids.
Whatever form galaxies intrinsically have it must origin from a superposition of orbit families. The triaxial models which are 'explored' by our merger remnants will result in a self-consistent distribution function naturally. It is therefore interesting to ask what fraction of which type of orbit is found in which merger remnant. We will analyse the orbital content of the remnants and confront our results to the theoretical work of self-consistent models of triaxial potentials.

5.1 Shape parameters

The shape of a triaxial mass distribution is determined by ratio of its three main inertial axis. We find the inertial axis through diagonalising the inertial tensor of each merger remnant. We bin the particles according to binding energy such that they follow the structure of the remnant naturally (Weil & Hernquist, 1996). The triaxiality is defined

$$T = \frac{1-(b/a)^2}{1-(c/a)^2} \tag{5.1}$$

where a, b, and c are the long, intermediate and minor axis respectively. Alle spheroidal shapes accesible for a triaxial configuration are illustrated in Fig. 5.1. Two sides of the triangle are formed by the axis ratios b/a and c/a. The diagonal line forms the T=1 division, beyond which the roles of major and minor axis would be reversed. That is the reason of course why the axis ratio space forms a triangle. At the three corners we find the limiting cases of triaxial spheroids: the sphere, the needle and and Kuzmins disk. In case of the sphere all inertial axis have the same length ($a = b = c$). All orbits are planar rossettes. Many physicaly viable distribution functions are known, e.g Hernquist sphere. The orbital content of Kuzmin's disk is also planar rossetes, albeit just in one plane ($a = b, c = 0$). The needle ($b = c = 0$) does have a self-consistent configuration (Tremaine & de Zeeuw, 1987), but

it is only one-dimensional. The prolate spheroids ($b/a = c/a$) are supported by the x-tube which are rather elongated. The oblate spheroids ($b = 0, 0 < c/a < 1$) just allow z-tubes. To the middle of the diagramm box orbits become more important. As both tube families are depopulated and actually oppose the shape of the figure, the box orbits have to be populated to sustain a triaxial form.

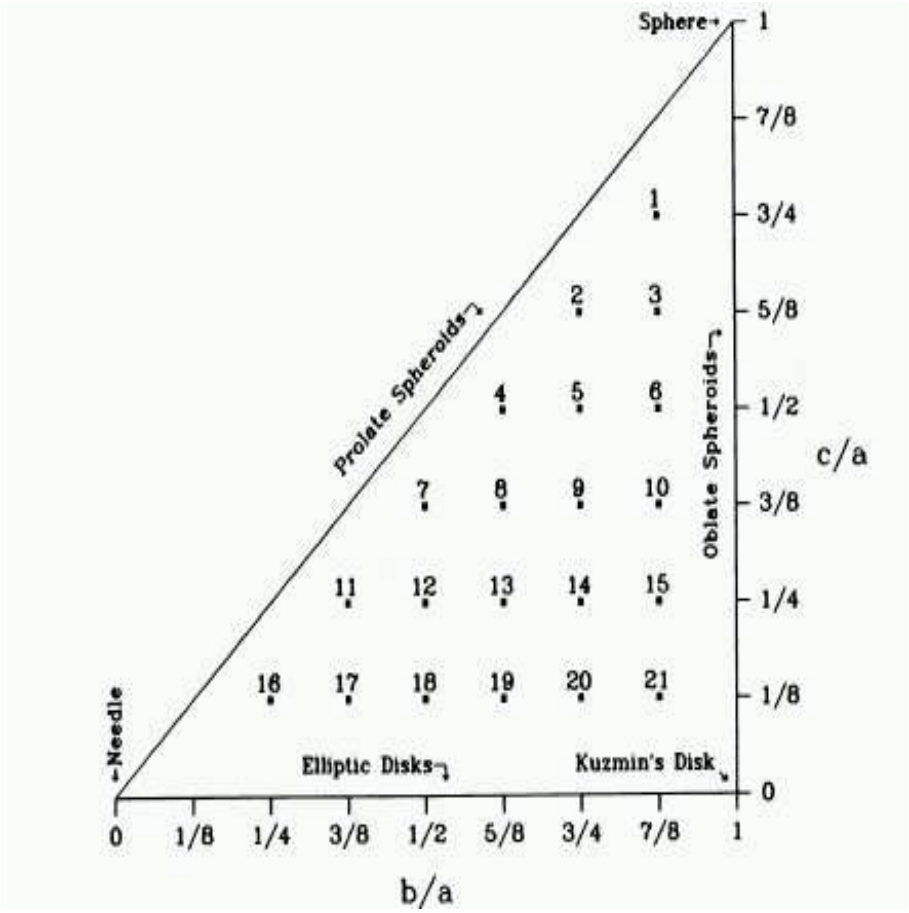

Figure 5.1: Overview of models in axis-ratio space. Figure reproduced from Statler (1987). Numbers inside the triangle denote models explored by Statler. We compare our results to the first ten.

5.2 The Shape of Merger Remnants

We can now place the remnants in such an axis ratio diagramm. It is especially illustrative to examine the merger remants inside out. We are plotting the results for the particle fractions of 0.1, 0.2, 0.3 and 0.4. Remember that each following plot includes the particles of the former. Therefore the expression shell is not accurate and we should speak of subsets of particles. The different merger ratios have been run with different number of particles. We list the real number of orbits for each subset and merger fraction in Table 5.1.

In Fig. 5.2 it is apparent how the shape of the remnant changes. The color coding in the plot subdivides the different mass fractions of the mergers. The 0.1 % subset is for all merger remnants rather prolate. More than 50 % have a triaxiality of more than 0.7. There is a very tight relation between the axis ratios. The mass fractions are occupying different stretches of this relation. Beginning with 0.2

Table 5.1: Number of orbits classified in merger remnants with different mass ratios

Mass Ratio	N_{lum}	N_{dark}	40% of N_{lum}	30% of N_{lum}	20% of N_{lum}	10% of N_{lum}
1:1	160000	240000	64000	48000	32000	16000
2:1	120000	180000	48000	36000	24000	12000
3:1	106666	160000	42666	32000	21333	10666
4:1	100000	150000	40000	30000	20000	10000

% subset the shapes are dispersing. Already here we can see that in the center one or only few orbit families determine the shape while further outside the shape is more complex and more families come into play. In the final panel the different merger ratios occupy overlapping regions in axis ratio space. But it is evident that 1:1 mergers are the most prolate remnants. Some 2:1 mergers interestingly have a high c/a, while being moderately oblate. The 3:1 and 4:1 mergers are the most oblate spheroids with a low c/a. However not few of them have maximum triaxiality of T=0.5. No merger remnant is found below a minor to major axis ratios of 0.5, although this would be theoretically possible.

It is instructive to list the mean orbit fractions for all plots shown, averaged over a mass fraction sample like Table 5.2. For a visual overview the reader is refered to the bar charts of appendix A. We can see that innermost particles are mostly box orbits, most of them non-resonant. Resonant orbits seem to play a minor role in all merger remnants. From 1:1 to 4:1 z-tube becomes gradually more important. x-tubes, especially inner x-tubes only appear in numbers in 1:1 mergers. The trends described visually are confirmed for the box and z-tube orbits. It is interesting that the mean values for the box orbits of the complete orbit sample is not very different for 1:1 to 4:1 mergers. Rather the amount of z-tubes is increasing. Where do the z-tubes go in the equal mass mergers? Mainly into the x-tubes. Very prolate remants, as seen before, are only shaped by 1:1 mergers.

The absolute numbers of the various orbit classes can be deceiving. The reader, e.g. could get the impression that our not classified orbits play a more important role in forming the shape of the remnant than the inner x-tubes. This is not true as the scatter of the x-tubes is much higher than of non-classified orbits. Irregular and non-classified orbits form a uniform background never amounting to more than to 15 % to 20 % of all the orbits in one given remnant. Remnants resulting from special orbital geometries can have up to 40 % of x-tubes (both types summed).
If the shape is decisive we should be able to build correlations between the main parameters, triaxiality, b/a and c/a and the orbital fraction. The triaxiality correlations are shown in Fig. 5.3. In detail the results are:

- Z-Tubes show a tight correlation of exponential form towards the oblate end T=0.
- X-Tubes show a good correlation towards the prolate end T=1. Although the correlation is clearly seen the orbital fractions a low.
- Box orbits peak at T=0.5, i.e. maximal triaxiality.
- Resonant Box orbits show the same qualitative behaviour like non resonant box orbits, but on a much lower level of abundance.
- Irregular and not classified orbits show no correlation at all with triaxiality. They form a uniform background with almost constant abundance and will be neglected in further analysis.

All results are in very good agreement with the theoretical discussion in the previous section.

Even more structure is visible when we look at the two-dimensional correlation in axis ratio space (Fig. 5.9). The same triaxiality can be achieved by a different combination of c/a and b/a as the the lines

Table 5.2: Classification results for different particle fractions of the remnants. The numbers are averaged over one mass ratio sample.

Merger Ratio	Resonant Box	Box	Z-Tube	Outer X-tube	Inner X-tube	Irregular	Not Classified
Statistics of the 10 % most bound particles							
1:1	0.0759	0.7666	0.0149	0.0174	0.0853	0.0324	0.0072
2:1	0.0722	0.7689	0.0484	0.0164	0.0333	0.0513	0.0095
3:1	0.0720	0.7361	0.1001	0.0073	0.0159	0.0587	0.0100
4:1	0.0669	0.7106	0.1256	0.0057	0.0092	0.0705	0.0115
Statistics of the 20 % most bound particles							
1:1	0.0984	0.5650	0.0748	0.0529	0.0793	0.0723	0.0574
2:1	0.0835	0.5848	0.1191	0.0390	0.0350	0.0939	0.0444
3:1	0.0854	0.5569	0.1617	0.0262	0.0216	0.0978	0.0508
4:1	0.0753	0.5270	0.2119	0.0221	0.0132	0.1020	0.0487
Statistics of the 30 % most bound particles							
1:1	0.1073	0.4512	0.1390	0.0818	0.0627	0.0642	0.0938
2:1	0.0956	0.4633	0.1976	0.0532	0.0262	0.0816	0.0823
3:1	0.0982	0.4422	0.2331	0.0363	0.0158	0.0832	0.0912
4:1	0.0848	0.4120	0.2954	0.0298	0.0098	0.0847	0.0835
Statistics of the 40 % most bound particles							
1:1	0.1169	0.3701	0.2040	0.0954	0.0544	0.0526	0.1064
2:1	0.1044	0.3798	0.2696	0.0585	0.0214	0.0662	0.1002
3:1	0.1046	0.3597	0.3102	0.0392	0.0127	0.0664	0.1072
4:1	0.0876	0.3318	0.3763	0.0320	0.0078	0.0678	0.0965

of equal triaxiality illustrate. The orbital abundance is not parallel to lines of equal triaxiality, but also changes with different c/a-b/a. This is seen in the panel which shows the box orbit abundance. The peak is located at T=0.5, but it is not a ridge that follows this value, but has also a gradient along the triaxiality line. The spread in the one dimensional triaxiality diagrams (Fig. 5.3) can be explained that way.

The z-tubes show a more clear cut behaviour than the boxes. They are confined to very oblate remnants and depopulate very quickly for other shapes. There is a notable exception at c/a$\approx$0.65 which shows an abnormal overabundance of z-tubes, extending to lower values of b/a. By closer inspection we find that three remnants show a spherical component in the center, which classifies as z-tubes. They origin from the same merger geometry. This symmetry seems to leave the bulge of the more massive galaxy unscathed. The bulges are Hernquist spheres and consist of planar z-tubes.

The box orbits and z-tubes show antagonistic behaviour. The isoabundance lines of the z-tubes at high abundance are identical with the lines of box orbit at low abundance. Those two families are the most dominant families in most of the remnants. This suggests that many kinematical features might depend on the ratio of the population of those two orbit families. We will exploit this finding in the folowing chapters.

Outer x-tubes and inner x-tubes are not occupying exactly the same positions in the diagrams. Inner x-tubes are abundant in more prolate models, while the outer x-tubes are also common in remnant which tend to the spherical limit. If we remember the shape of the orbits this is understandable. The inner x-tube are far more elongated along the major axis while outer x-tubes support a round and thick shape.

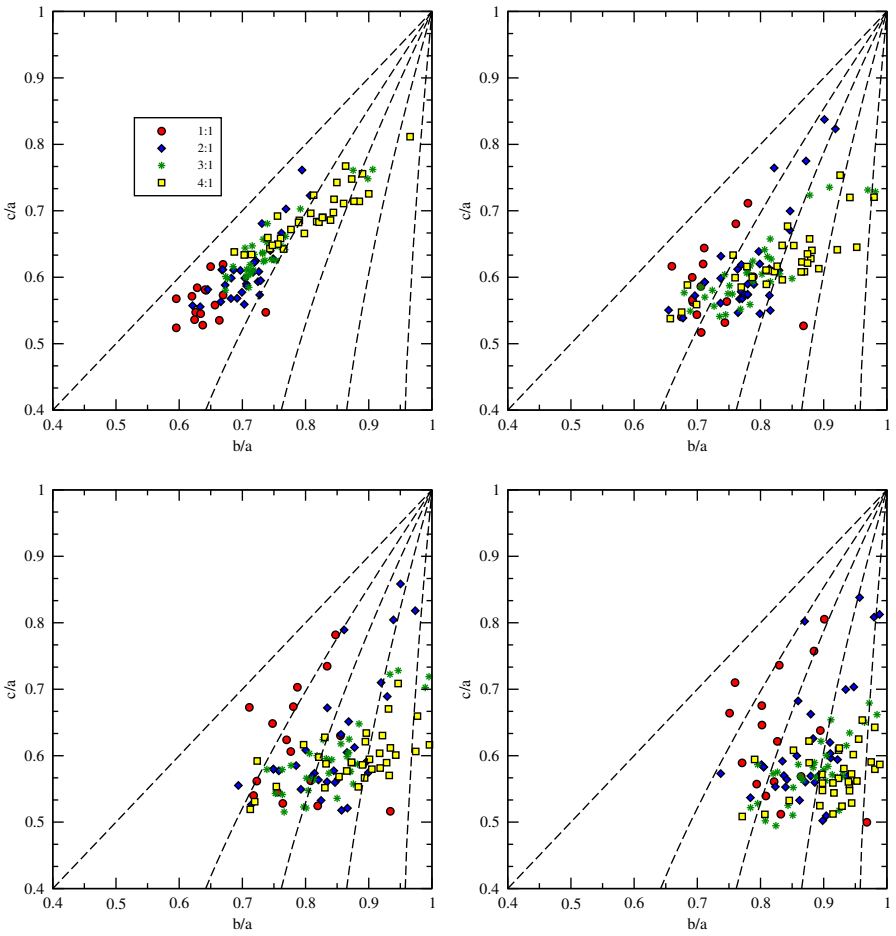

Figure 5.2: Axis ratios of the merger remnants for different particle fractions. Top Left: 10 % most bound particles. Top Right: 20 % most bound. Bottom Left: 30% most bound. Bottom Right: 40% most bound. Lines of equal Triaxiality are overplotted. From left to right T= 1, 0.7, 0.5, 0.3, 0.1.

5.3 Distant Encounter

The correlations between the shape of the remnant and its orbital content are by themselves interesting results. But are these results under all circumstances pathological? Even if we restrict ourselves

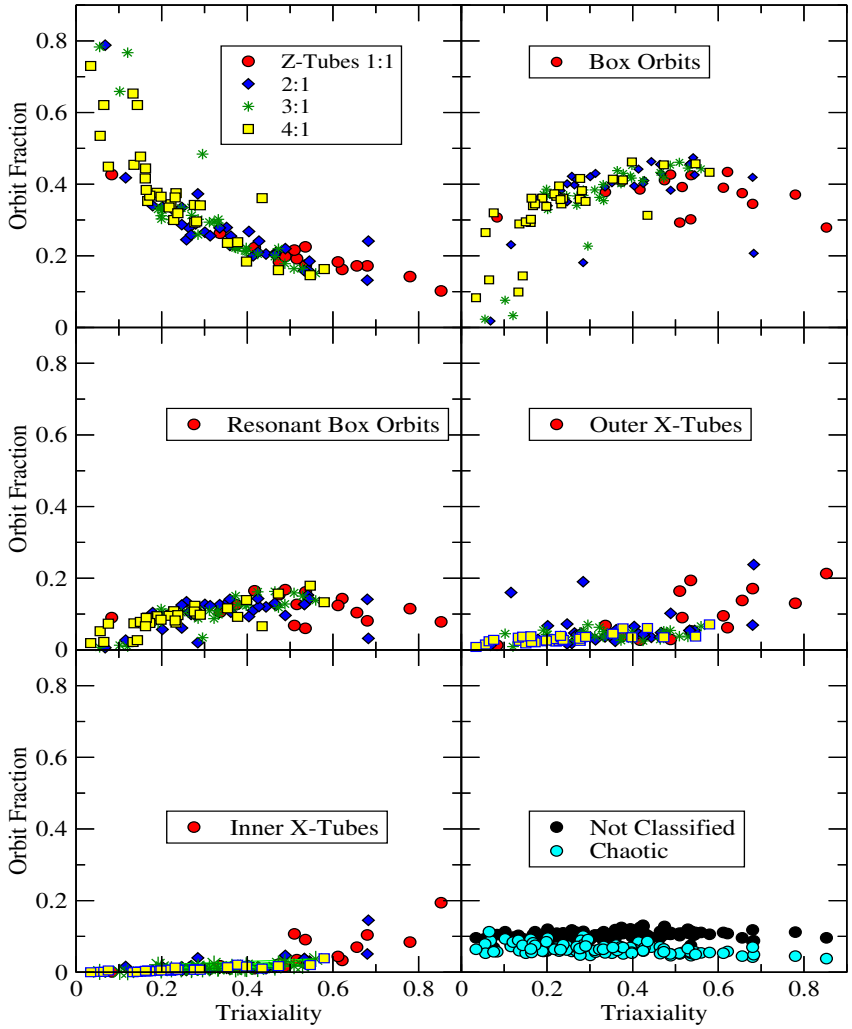

Figure 5.3: Dependence of the fraction of different types of orbit families on the triaxiality of the merger remnant calculated from 40% of the particles sorted according to binding energy.

to dissipationless mergers, we do not know if the merger symmetries we used are representative in a cosmological context. Recently Khochfar & Burkert (2003) examined the distribution of merger symmetries of dark matter halos in a cosmological simulation of the VIRGO CONSORTIUM. The results which are relevant for us are summarized in Fig. 5.4. Most of the encounters found at low pericenter distances are parabolic orbits. This is in agreement with the orbital parameters used in this study. The pericenter distances of the first sample corresponds to approximately 5% of the virial radius of the dark halo of the remnant. However, the bulk of the mergers have rather bigger encounter distances and additionally the eccentricities start to scatter from the parabolic value of ϵ=1. The

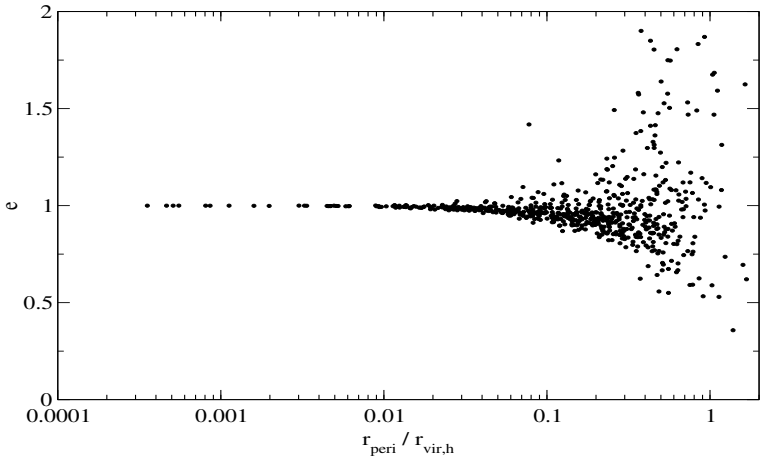

Figure 5.4: Orbital parameters of merging dark matter halos found cosmological simulations. Figure kindly provided by S. Khochfar

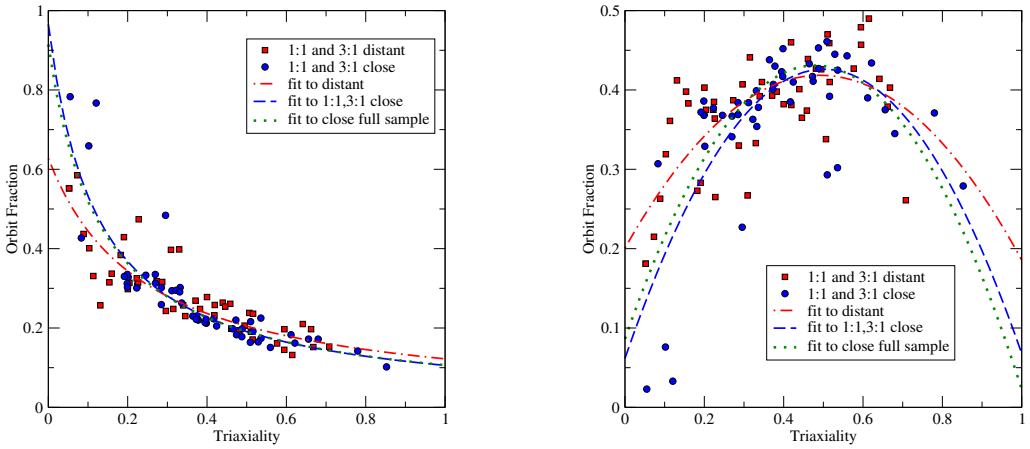

Figure 5.5: Fit to correlations between triaxiality and orbit occupation number. Left: Z-tubes. Right: Box orbits.

paramater space is too big to be surveyed, hence we first test how the results differ when we enlarge the pericenter distance to 6 disk scale lengths which corresponds to roughly 15% of the virial radius. As explained in the previous chapter the distant encounter sample just contains 1:1 and 3:1 mergers. We will therefore compare only to the 1:1 and 3:1 mergers of the close encounter sample.

48 mergers are too few to interpolate them on a regular grid in two dimensions. Instead we will perform a χ^2-fit on the simple correlations we found for the triaxiality (see Fig 5.5). As we have the best statistics for boxes and z-tubes we restrict ourselves to these orbit families. For the box orbits of the reduced (just 1:1 and 3:1) close encounter sample we fit a quadratic function to reproduce the two

falling wings to the prolate and the oblate end. We find the correlation

$$f_{box} = 0.061 + 1.45T - 1.44T^2 \tag{5.2}$$

and for the distant encounter sample

$$f_{box} = 0.201 + 0.89T - 0.90T^2. \tag{5.3}$$

Already here we can see that the distant encounters follow a shallower correlation. Ideally the constant of the correlation should be 0, meaning at the extreme triaxiality limits the number of box orbits drops to zero. This is not the case, the correlation for distant encounter crosses the y-axis at 0.2. One could argue that more 2:1 and 4:1 encounters could alleviate the situation, but when we look at the relation of the full sample of the close encounters

$$f_{box} = 0.09 + 1.44T - 1.50T^2, \tag{5.4}$$

we see that the relation changes only slightly. Firstly this means we could have predicted the orbital content of the 2:1 and 4:1 remnants if we would have known the triaxiality. Secondly also the distant encounter correlation probably will not change much if we would simulate 2:1 and 4:1 mergers. Similarly for the z-tubes we find

$$f_{z-tube} = \frac{1}{1.59 + 6.59T} \tag{5.5}$$

for the distant encounter sample

$$f_{z-tube} = \frac{1}{1.04 + 8.41T} \tag{5.6}$$

for the reduced close encounter sample and

$$f_{z-tube} = \frac{1}{1.09 + 8.31T} \tag{5.7}$$

for the total close encounter sample. Note that we would expect 1 for the constant in the denominator such that the fraction of z-tubes would be one for T=0.
The population process which operates in close and distant mergers seems to be different. The dependence on triaxiality seems to be less obvious in the distant encounter sample. The correlations are flatter and do not go to 0, respectively 1. We want to shed some light on the triaxiality distribution of the two samples, which can be seen in Fig. 5.6. The distant encounter sample is less peaked, but also has less extreme triaxialities than the close encounter sample. The peak from the close encounters and the distant encounters moves from prolate to oblate, while the scatter of shapes is bigger for the close encounter sample. Interestingly the decrease of diversity in the shapes of the distant encounters alleviates another problem of dissipationless mergers found by Naab & Burkert. They found merger remnants which have projections with very high ellipticity, although they are not rotating significantly. Such ellipticals are not observed. These merger remnants are however located at the prolate end of the triaxiality correlation. If we would exclude them, we would still have a significant difference between close and distant encounters.

5.4 Schwarzschild Method vs Merger Remnants

The results of the previous sections give a good insight into the shape evolution of the individual mergers, respectively on the influence of the mass fraction on the orbit population. General properties (see previous chapter) of the orbits are in agreement with expectations of orbit theory. What we really want to know is if the occupation number of orbits for a given shape agrees with what theoriticians and observers use in constructing self-consistent models or fitting orbit libraries to kinematical data

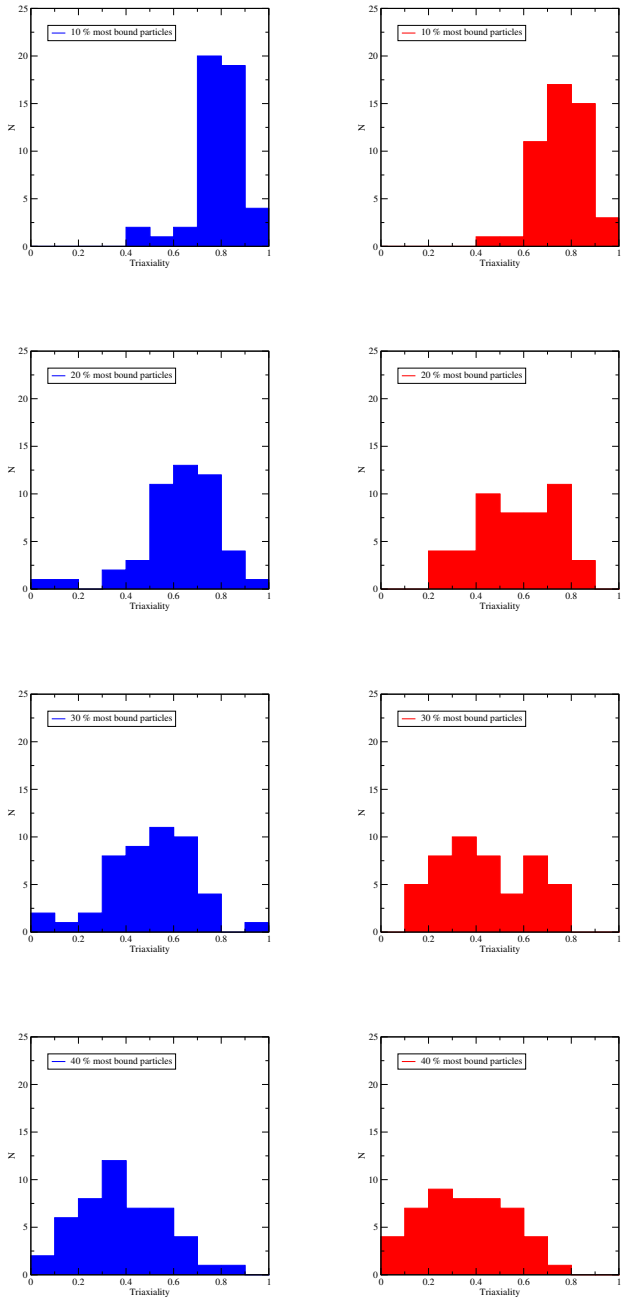

Figure 5.6: Statistics of triaxialities at different particle fractions of the mergers. Compared are the 1:1 and 3:1 sample of the close encounters (left) and of the distant encounters (right).

of elliptical galaxies. For both tasks variants of the Schwarzschild method are applied.
For observations, however, almost only axis-symmetric models either with two-integrals or with three integrals have been used. Kronawitter et al. (2000) examined the orbital structure of a sample of E0/1

galaxies and could restrain themselves to spherical models. Cretton et al. (2000) determine the orbital anisotropy of the giant elliptical NGC2320 with an axisymmetric model. They briefly discuss that orbit fractions found in triaxial merger remnants cannot be compared with their results, because box orbits do not exist in axisymmetric models. Mathieu & Dejonghe (1999) construct a triaxial Stäckel model which they fitted to data of Centaurus A, but gave no explicit orbit fractions. If triaxial models are in general to be preferred to axisymmetric or spherical models is another question. At least in some galaxies it seems to be feasible. Matthias & Gerhard (1999) examined the boxy elliptical NGC 1600. They had to put a lot of mass on radial z-tube orbits, i.e. z-tubes with very low angular momentum, and speculated if NGC 1600 is in truth triaxial the mass could be better assigned to box orbits. For a comparison with our merger remnants there are no usable orbit fractions from observations which tried to fit a triaxial model in the literature.
There are two theoretical works which give explicit numbers of orbit fraction in models of triaxial galaxies. Statler (1987) constructed several models for the perfect ellipsoid (de Zeeuw & Lynden-Bell, 1985) which has a smooth core. He finds mathematically allowed solution for all possible axis ratios. There is not only one model for each axis ratio but a solution space constrained by the extreme angular momenta of the orbits. He terms the solutions xmax, for weight on maximum L_x, zmax for weight on maximum L_z and min, for a minimum weight on any angular momentum. As can be guessed the minimum solutions prefer models which populate more box orbits. The xmax solution prefers x-tubes and the zmax prefers z-tubes. He also uses a different numerical method, called Lucy's method, which converges on a solution in the middle of the angular momentum solution space and therefore does not prefer any type of orbit. In Fig. 5.7 Statler's results are contrasted to our results. We only compare models c/a greater or equal to 0.375 (see Fig. 5.1 models 1-10), because no merger remnant falls below this value (in truth they do not even fall below 0.45 or so, but there are not enough models to compare to). Note that we are plotting both x-tube families in one plot for better comparison.
The xmax solution comes quite close in absolute numbers as well as in tendency towards the relations we extract from the merger sample. The zmax and Lucy's solution show an increase in box orbit fraction with triaxiality beyond T=0.5, which we do not observe. The min solution shows no dependence on triaxiality for z-tubes, which we also do not find. It is open to debate if the xmax solution has any bearing on the processes which populate the orbits. Maximum L_x should prefer x-tube over z-tubes in general, which is not the case in mergers as they are results of the collision of two disks which are purely composed of z-tubes. Consequently we find that z-tubes are more prominent in the mergers than x-tubes.

A related study by Terzic (2003) highlights the stability of triaxial scale-free potentials (see also Merritt, 1997). He uses a combination of Schwarzschild method and spectral analysis to build self-consistent models. He uses a Schwarzschild code to match the scale-free triaxial density distribution, but also finds the base frequencies of the orbits. The classification of the orbits is analogous to CA98. Additionally he computes the diffusion time of the orbits. A chaotic orbit does not keep his base frequency. The integration of an orbit from say t=0 to t=100, and from t=100 to t=200 will not give the same result if the orbit is chaotic. The rate of diffusion according to this definition is simply $\delta\omega = \frac{\omega_0 - \omega_1}{T}$, where T is one integration interval. The more chaotic the orbit is the higher the rate of diffusion. For a regular orbit $\delta\omega$ will be exactly zero. The scale-free models in his calculations are variable in the steepness of their central density cusps. He finds that the parameter space of allowed shapes diminishes with increasing steepness of the cusp. This is so because an ever greater amount of orbits becomes stochastic and cannot retain a very triaxial shape. In very steep cusps only the extreme models with T=1 (prolate limit) and T=0 (oblate limit) can survive. Balsa Terzic kindly provided us with the detailed data for the weak cusp $\rho \propto r^{-0.5}$. At this steepness he finds the biggest number of feasible models which lie between c/a=1 to c/a=0.5, which is in good agreement with the merger remnants. We can now overplot his results to the merger sample, additionally to Statler's results we can compare the resonant box orbits as well. Again the tendencies are the same, except for the resonant orbits. The explanation might be that the higher resonances are not taken into account but added to the normal box orbits for pragmatic reasons (Terzic, private communication). The box orbit fractions also drops towards the prolate and the oblate ends in the final model, In contrast the

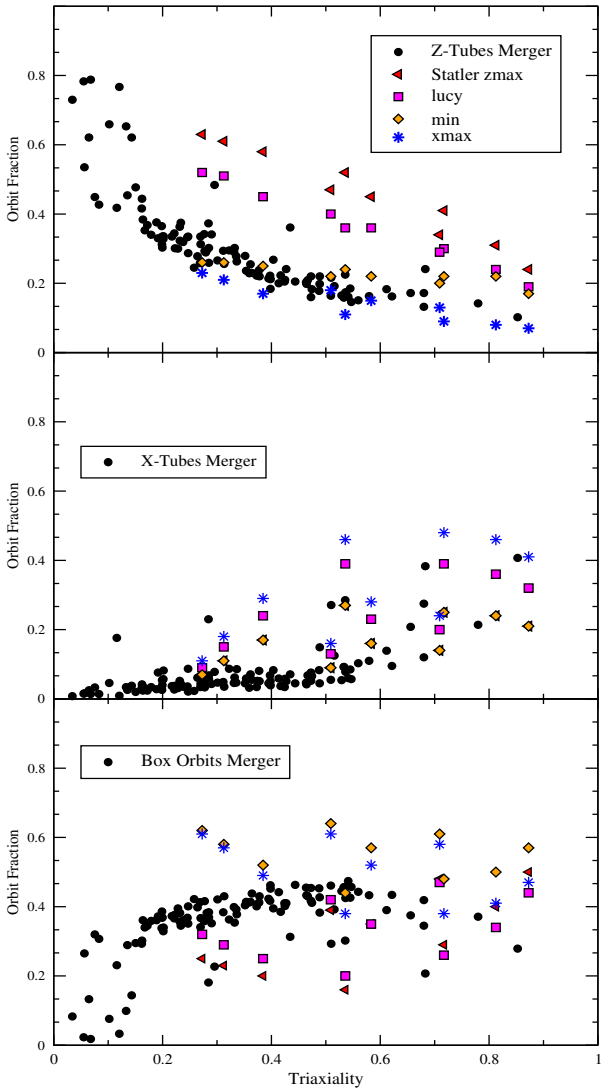

Figure 5.7: Comparison of the merger sample orbit fraction with orbit fraction from Statler(1987) self-consistent triaxial Stäckel model.

top-most row of models shows an inverse behaviour. These are extreme models with c/a=0.9 which we do not observe in the merger remnants. It is possible that these models are feasible, but can result only from an unlikely merger symmetry. The scatter in his results for a given result show that a different combination of c/a and b/a will result in a slightly different orbit fraction although the triaxiality parameter has the same value.

5.5 Discussion

We analyzed the orbital content of a large sample of dissipationless mergers and correlated the number fraction of different orbit classes with the shape. We achieve a suprisingly concise picture for the close encounter sample. Correlations with triaxiality (one-dimensional) and axis ratios (two-dimensional) are tight and homogeneous over a large range of triaxialities. Trends in the occupation numbers of the different orbit classes are in agreement with general considerations of triaxial models and with detailed studies of self-consistent triaxial configurations constructed with the Schwarzschild method. Orbit fractions in merger remnants and fraction obtained from Schwarzschild methods do not coincide in absolute numbers and find trends which we do not observe. We list what we think are the main reasons for the discrepancy.

- The integration of our orbits is noisy. The algorithm does not classify about 10 % of the orbits. Schwarzschild methods have infinite resolution in the integration of the orbits. (Not in the resolution of fitting the library to a mass model, of course)
- The potentials have not the same central density structure. The perfect ellipsoid has a smooth core and is expected have more tubes in general. Terzic explores a variety of cusps, but unfortunately there was no data for $\rho \propto r^{-1}$ available, which would be more suitable for our remnants.
- The mergers are not self-similar, but change shape with radius. We simplified the picture by assigning a typical triaxiality close to the half-mass radius. We tested the impact of these twists and found them to affect the classification neglibly, however there are no Schwarzschild models for such a case to test our classification more rigorously.
- The population process in the Schwarzschild models has to be chosen in a certain way. Statler weighted different orbit classes according to their angular momentum, while Terzic chose to use the start space method devised by Schwarschild to explore the orbital content of the logarithmic potential. The mergers populate in a natural way. The phase space is rearranged through the violent relaxation process during the tidal disruption of the galaxies. In other words there is no non-uniqueness problem for the merger remnants.

This nice picture fails for the distant encounter sample, though. The orbit fraction seem to 'decouple' from the triaxiality of the merger remnant, as the correlation flattens out. We could argue that the distant encounters leave more of the original disk intact, but this is not the case. Indeed the opposite is the problem, we can produce more oblate models with close 3:1 encounters. This can be seen by the fact that the correlation for z-tubes approaches rapidly 1 for T=0, not so for the distant encounters. Another problem might be that the triaxiality value we choose does not describe the remnant well. Instead of sorting the particles according to binding energy, we will have to determine the triaxialities from the density structure directly. Streaming motions might also prove to be a powerful tool to cross-check intrinsic shapes more reliably (Statler et al., 2001).
In a long term perspective this point should be settled, because the distant encounters are more relevant from the viewpoint of hierarchical galaxy formation in CDM, than the close encounters.

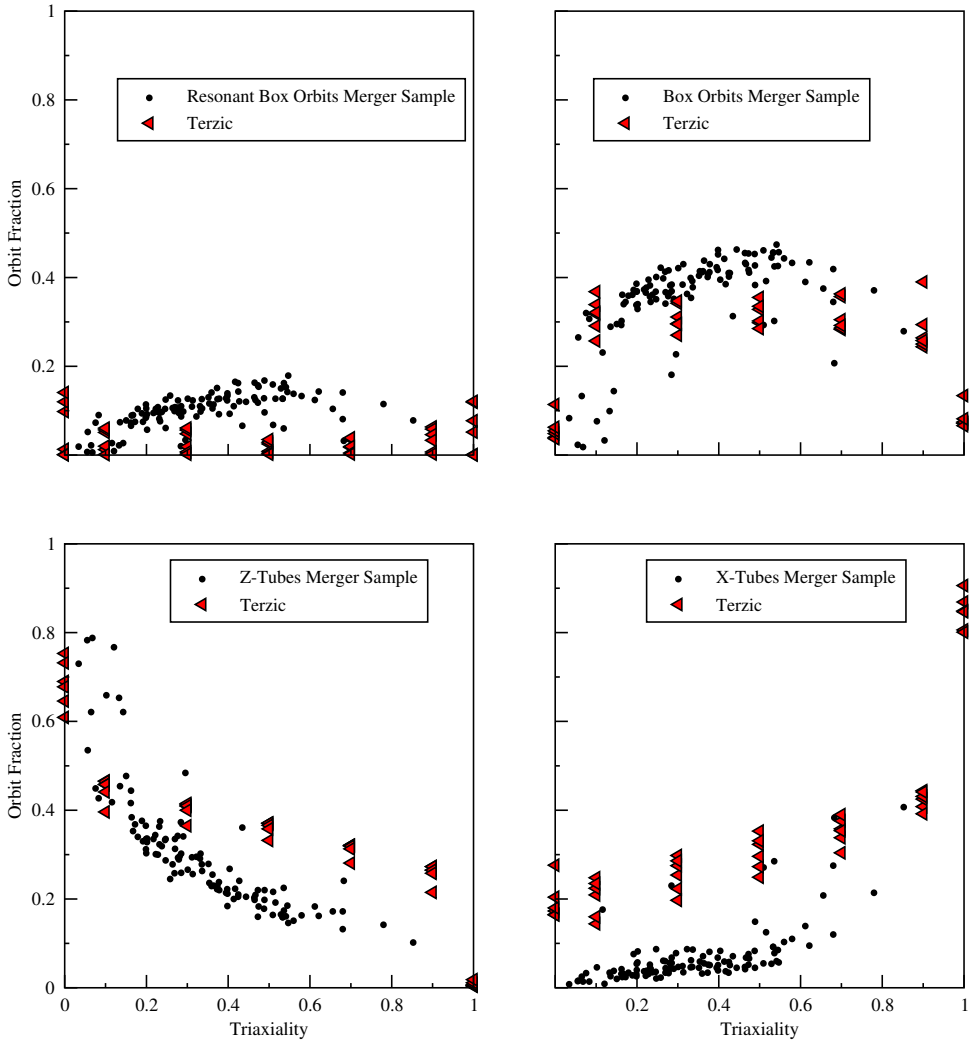

Figure 5.8: Comparison of the merger sample orbit fraction with self-consistent triaxial models of Terzic with a shallow cusp γ=0.5. Data kindly provided by B. Terzic.

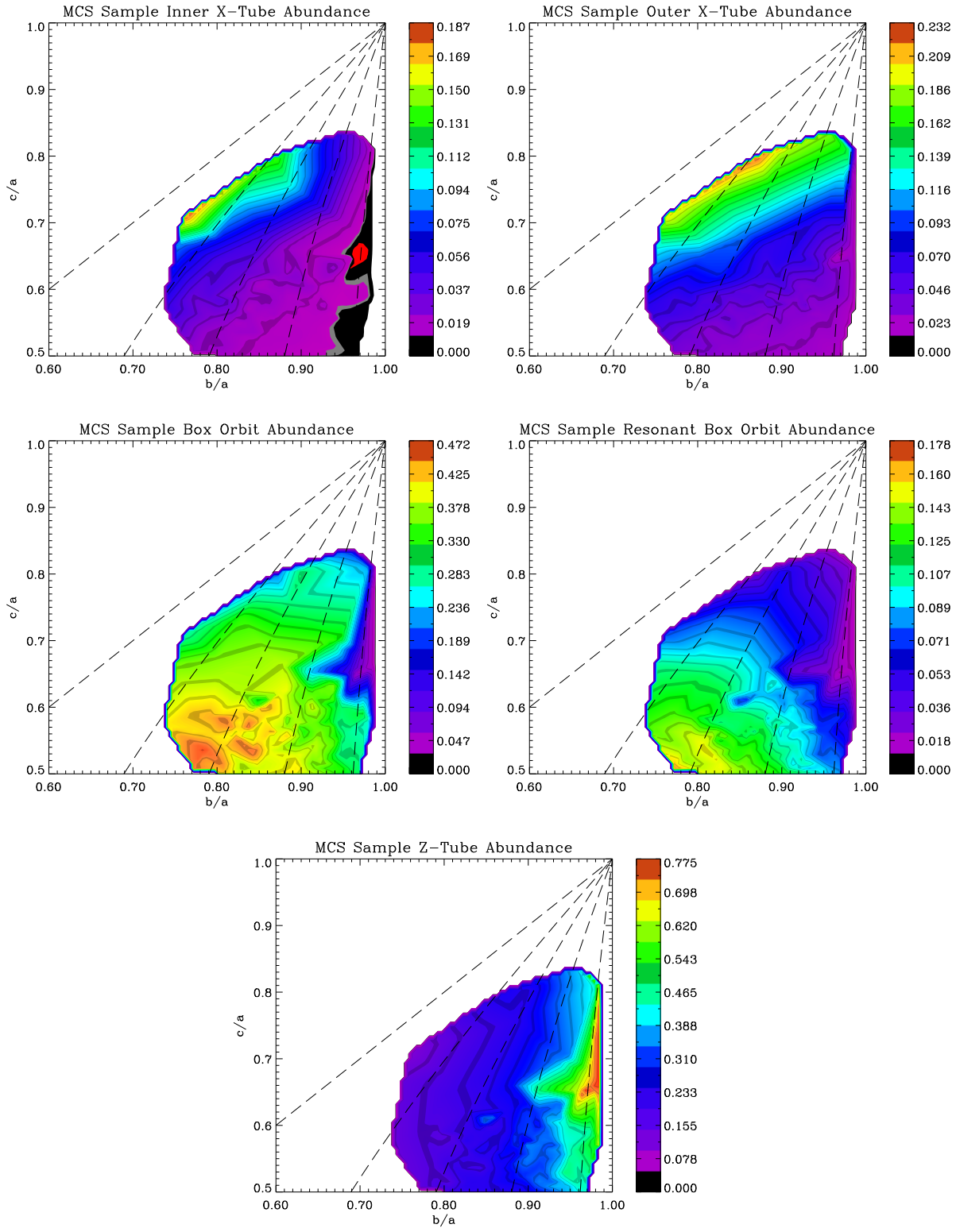

Figure 5.9: Abundance of different types of orbit families in merger remnants with different shapes. The sample of 112 mergers is linearly interpolated on a regular grid to get a smooth picture. We examine here the orbital content of the 40% most bound particles. Lines (dashed) of equal triaxiality are overplotted: T= 1, 0.7, 0.5, 0.3, 0.1.

Chapter 6

General Kinematical Features

We want to show in this chapter that our orbit classification also fulfills expectations of general kinematical features. We must expect that x-tubes are responsible for apparent minor axis rotation and z-tubes for major axis rotation. Box orbits should have in general a higher velocity dispersion, because of the lack of a coherent rotation. We will try to find correlations between the relevant parameters.

6.1 Major Axis Rotation

Z-tubes rotate as the name indicates about the minor axis of the system, hence we would measure significant velocities along the major axis. Like in spiral galaxies it is better to extract the rotation curve, when they are seen edge on, rather than face on. We will plot the mean velocities along the major axis of the z-tube component of two 1:1 remnants. For better comparison we also plot the mean velocities of the same orbits along the minor axis. For better understanding we want to stress, when we are saying, we are plotting the velocity of an 'orbit' it means we are always examining the coordinates and velocities of the particles of the last dump of the merger simulation and not of a subsequent integration that we are performing. This is a really hard test, as we select the particles we examine only according to our classification scheme. In Fig. 6.1 we see that the particles we selected indeed have a significant rotation velocity along the major axis with respect to the rotation of the whole remnant. They show a significantly lower velocity along the minor axis. We could have shown mean velocities of the z-tube component 3:1 or a 4:1 remnant, which rotate much faster. But those remnants rotate much more in total (see also Fig. 6.2) than a typical 1:1 remnant, and the signature would not stand out so much.

Globally the z-tube fraction correlates with the mean of the absolute value of major axis rotation (Fig.6.2). We average here over 50 projections. For z-tube fractions around 20 % there is no clear correlation. The picture is more complicated for the 1:1 remnants as they can produce large amounts of counterrotating populations of tube orbits. The mean rotational velocity can be significantly reduced or neutralized. There is one extreme case of a 1:1 remnant, where the z-tube fraction amounts to 40 %, but there is almost no rotation. This is no surprise, because the merger symmetry is a frontal collision, while the disks have anti-parellel spin vectors.

6.2 Minor Axis Rotation

We extract like in the example before the rotation curve of orbits, this time classified as x-tubes. Because they rotate about the major axis, observers would see the rotation along the minor axis. We have not so much choice this time. X-Tubes are prevalent only in 50 % of 1:1 mergers and in only 10% of 2:1 mergers. We cannot use the 3:1 and 4:1 remnants in this section.

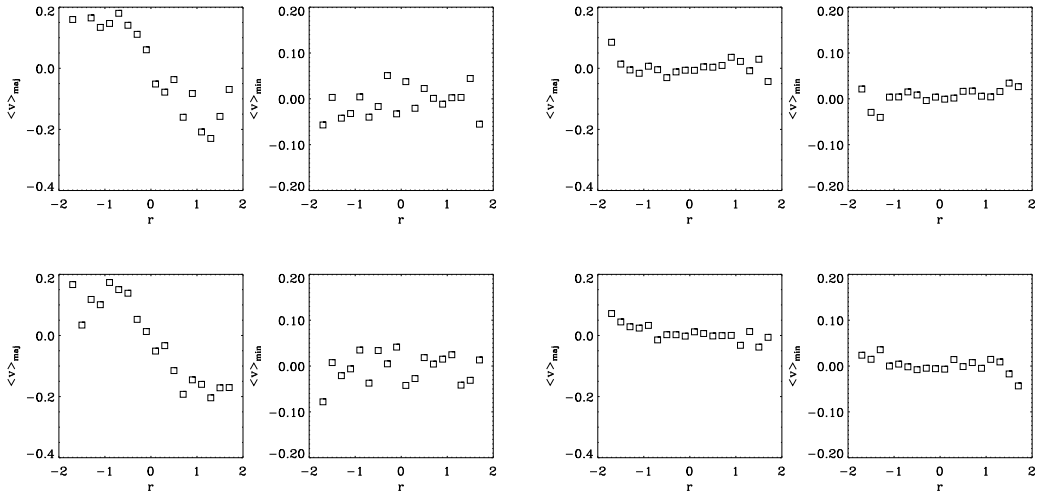

Figure 6.1: Left Column: Mean Velocities along major and minor axis for particles classified as z-tubes in two different 1:1 remnants. Right Column: Same measurements but this time the complete remnant

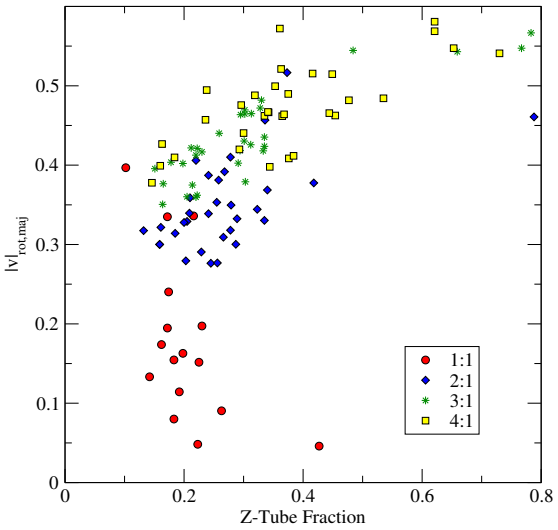

Figure 6.2: Correlation of the absolute value of rotation along the major axis with the z-tube fraction

Observers often use the parameter μ to measure the amount of minor axis rotation. It is defined as

$$\mu = \frac{v_{min}}{\sqrt{{v_{min}}^2 + {v_{maj}}^2}}. \tag{6.1}$$

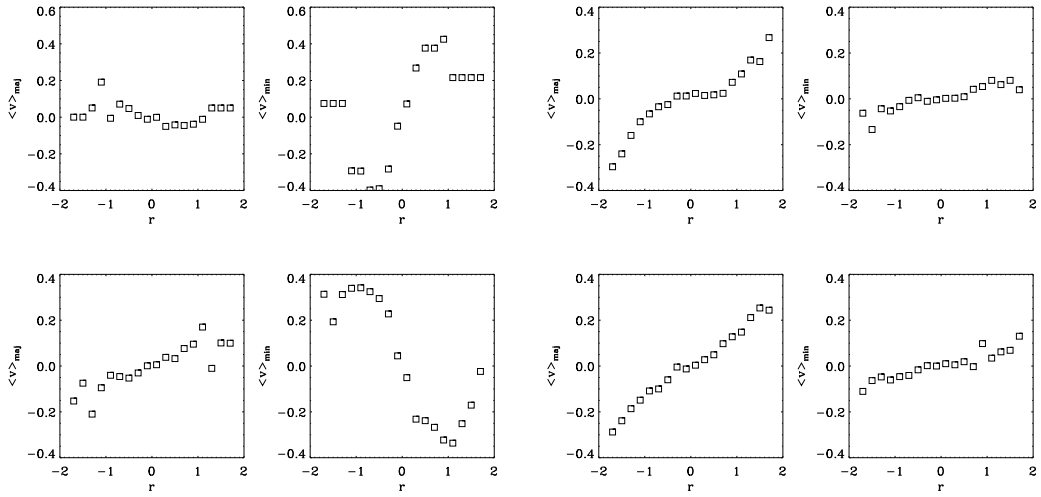

Figure 6.3: Left Column: Mean Velocities along major and minor axis for particles classified as x-tubes. Right Column: Same measurements but this time the complete remnant

A high value of μ in combination with isophotal twists is used as an indicator for triaxiality (Binney, 1985). We can ask if this property is really a good indicator for triaxiality. Again the illustration in 2D can help us. If we look at Fig. 6.4 we see that μ peaks at almost exactly T=0.7. While this is a significant amount of triaxiality, models which lie between the triaxiality maximum and the oblate limit would not be recognized. Even mergers at T=0.5, but with a low value of c/a cannot be detected by this parameter.
It is a good indicator for minor axis rotation though. Fig. 6.5 shows the correlation between the x-tube abundance and the true minor axis rotation value, respectively μ. Both correlations are in good agreement. The correlation for the absolut value of the rotation is smoother than with the μ parameter, as could be expected. However, even for the true minor axis rotation there are some outliers, which again might be explained with counter rotating populations of x-tubes.

6.3 Box orbits and Central Velocity Dispersion

Box orbits which have a negligible mean angular momentum should not rotate at all. This time we examine two 3:1 remnants, because the whole remnant rotates significantly, we must make sure that we extract the orbits which do not contribute to the rotation. The results can be seen in Fig. 6.6. We plot this time the rotation along the major and the intermediate axis. We do not expect a significant number of x-tubes in the remnant and hence no misclassification. The results are unambigous. These orbits really do not rotate, while the remnant shows a clear rotation curve.

Eskridge et al. (1995) found interesting correlations between structural parameters, such as a4 or a/b and properites of the ISM in elliptical galaxies and S0s. σ_0, the central velocity dispersion is often taken as an indicator of the depth of the potential well of an early type galaxy. They found strong correlations with the B-band luminosity of the ellipticals in their sample, which they assume to be a good tracer for the mass of the galaxy. They do not find a good global correlation between the central velocity dispersion and the shape of the galaxy though. However, for constant L_b there is a significant correlation. They speculate that at a given luminosity (or to say mass) there is a higher support of rotation in flatter systems.

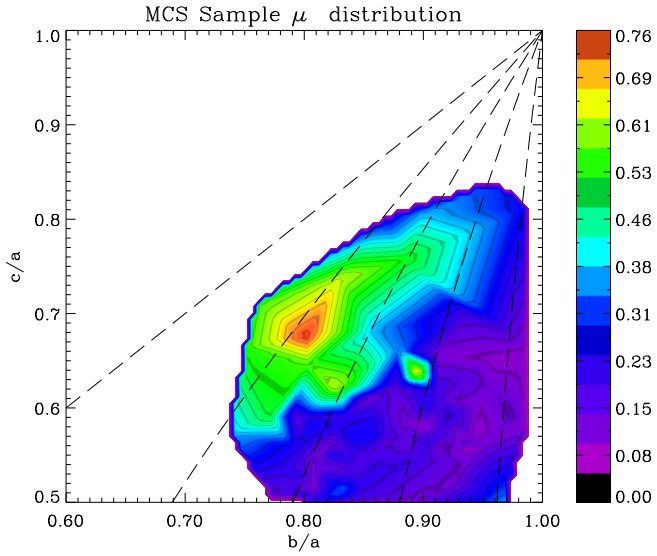

Figure 6.4: Distribution of μ parameter as defined in text in axis ratio space.

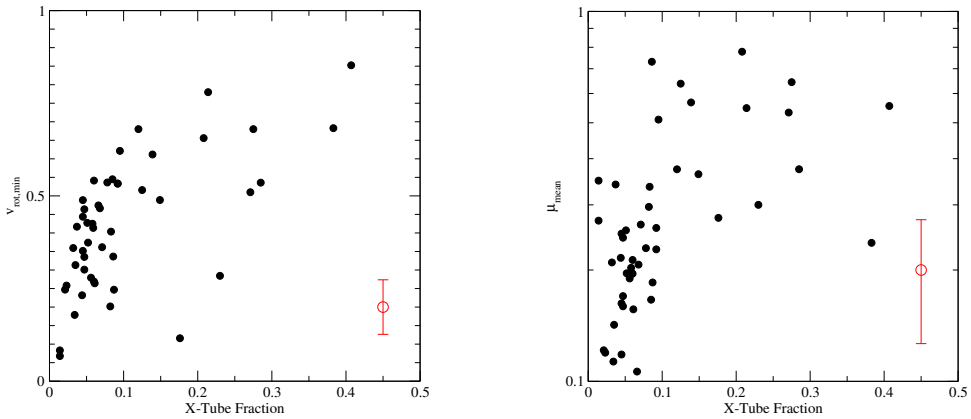

Figure 6.5: Comparison between true minor axis rotation and the mean μ value. Left plot: minor axis rotation vs x-tube fraction. Right plot: μ parameter vs x-tube fraction. For clarity only values of 1:1 and 2:1 mergers are plotted. μ is averaged over 50 projections. Typical errors are indicated lower right corner.

When we plot the correlations between the central velocity dispersion and box to z-tube ratio in the remnants, we indeed find that the correlation divide up into the different mass ratio samples. Of course, we know that in each sample the mass (or so to speak luminosity) is identical. We also know that the fraction of box and z-tube orbits is a very good indicator of the shape of the remnant (at least in the close encounter sample). But, of course, if we would observe these remnants without

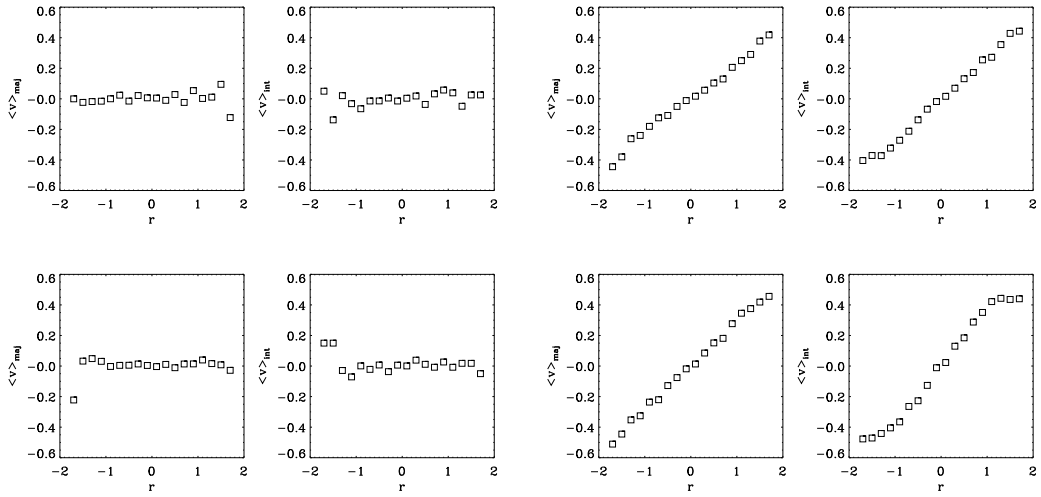

Figure 6.6: Left Column: Mean Velocities along major and intermediate axis for particles classified as boxes in two different 3:1 remnants. Right Column: Same measurements but this time the complete remnant

the background knowledge we have we would find no correlation between the velocity dispersion and the shape, because the same amount of velocity dispersion can appear in a 2:1 or 4:1 remnant, but corresponds to a different box to z-tube ratio (different shape). Albeit inside a sample a higher σ_0 value would mean more box orbits, which also means less flattening and could be perceived as a rounder galaxy in projection.
It is too far fetched to explain the findings of Eskridge and co-workers with dissipationless mergers. There are stronger correlations between σ_0 and Mg_2, which are determined by the evolution of the gas inside these galaxies. We cannot make any statement of absolute masses, because the merger simulations are scale-free. Also there will be other mergers in nature like 1:1.5 or 1:2.5, which will further wash out any dependence on the shape. But at least it is a simple procees which can explain a similar structural dependence on σ_0. We list the correlations for completeness.

$$\sigma_0 = 0.69 + 0.027 f_{b/z-tb} \tag{6.2}$$

is the correlation found for the 1:1 sample

$$\sigma_0 = 0.6 + 0.039 f_{b/z-tb} \tag{6.3}$$

for the 2:1 sample

$$\sigma_0 = 0.54 + 0.049 f_{b/z-tb} \tag{6.4}$$

for the 3:1 sample

$$\sigma_0 = 0.53 + 0.043 f_{b/z-tb} \tag{6.5}$$

and for 4:1 sample.

6.4 Discussion

Our orbit classification passes elementary kinematical test and gives us confidence that we have indeed extracted the correct orbit classes. We can proceed now to more complex features of remnants like

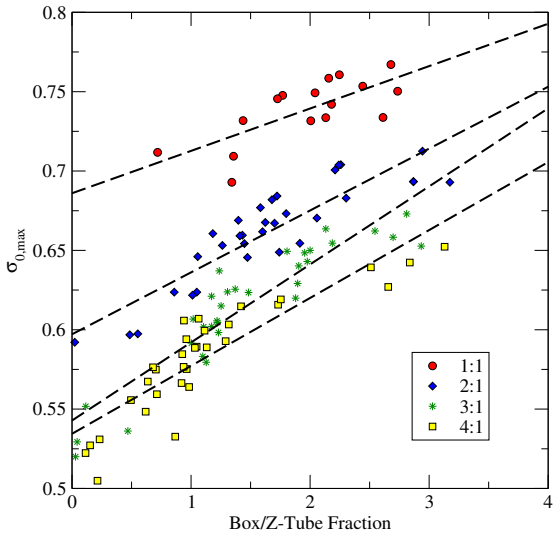

Figure 6.7: Correlations between the central velocity dispersion σ_0 and the box to z-tube ratio. χ^2-fits are overplotted.

isophotal shape and higher moments of the line of sight velocity distribution which have no clear theoretical connection with the orbital content.

Chapter 7

Orbit Classification and the Isophotal Shape of the Remnants

Observations have shown that a large fraction of ellipticals exhibit small deviations from purely elliptical isophotes (see e.g. Bender et al., 1988). By expanding the radial deviations $\Delta r_i = r(t_i) - r_E(t_i)$ between the radius of an isophote $r(t_i)$ and the best fitting elliptical isophote $r_E(t_i)$ in a Fourier series can th isophotal shape be found. Here the t_i are the equidistant polar angles from the origin to N isophote points. With $\Delta r_i = \Delta r(t_i)$, $r_i = r(t_i)$ and $r_{i,E} = r_E(t_i)$ the expansion read as

$$\Delta r_i = r_i - r_{i,E} = \sum_{j=0}^{N-1} a_j \cos\left(\frac{2\pi ij}{N}\right) + b_j \sin\left(\frac{2\pi ij}{N}\right). \tag{7.1}$$

In nearly all elliptical galaxies the fourth-order cosine coefficient a_4 dominates the Fourier spectrum. Figure 7.1 shows the effect of a non-zero a_4-coefficient. A positive value of a_4 corresponds to an elongated, pointed or disk-like shape (hereafter called *disky*) while a negative value of a_4 corresponds to an isophote with a box-like shape (hereafter called *boxy*). To get a scale free parameter for the isophotal shape it is convenient to measure isophote shapes by $a4 = a_4/a$ where a is the semi-major axis of the best fitting ellipse.

Heyl et al. (1994) investigated the disky and boxy shapes of simulated merger remnants of disk- disk coliisions and came to the conclausion that each remnant could be made boxy or disky depending on the viewing angle. Lima-Neto & Combes (1995) reach a similar conclusion, but they are also analysing collapsed structures. Their point is the reverse that initially the collapsed objects are boxy. The big collapsed objects (giant ellipticals) are not disturbed by mergers and retain their boxyness. While smaller ellipticals get more disky with continuing merging. Bekki & Shioya (1997) argued that isophotal shapes are a sign for a different history of star formation. Rapid star formation can produce more likely boxy isophotes and slow star formation disky isophotes. Barnes (1998) argued that the difference of isophotal deviations in observed galaxies could be explained without dissipation, only by different mass fraction of the merging disks. Unequal mass-fractions would lead to disky merger remnants and equal mass mergers are progenitors of boxy ellipticals. This hypothesis was tested and confirmed by Naab et al. (1999), who found that a sample of 3:1 mergers and 1:1 form two distinct groups of objects with preferably disky, respectively boxy isophotes.

7.1 Extraction of the Isophotes

We use a software package programmed by T. Naab to reduce the observable quantities of the remnants. For determination of two dimensional properties this the merger remnant is binned in a 128x128 pixel grid. The picture is smoothed (Gaussian) to account for seeing in a real observation. It is beyond the scope of this thesis to describe the extraction of the observable properties in detail. We refer the

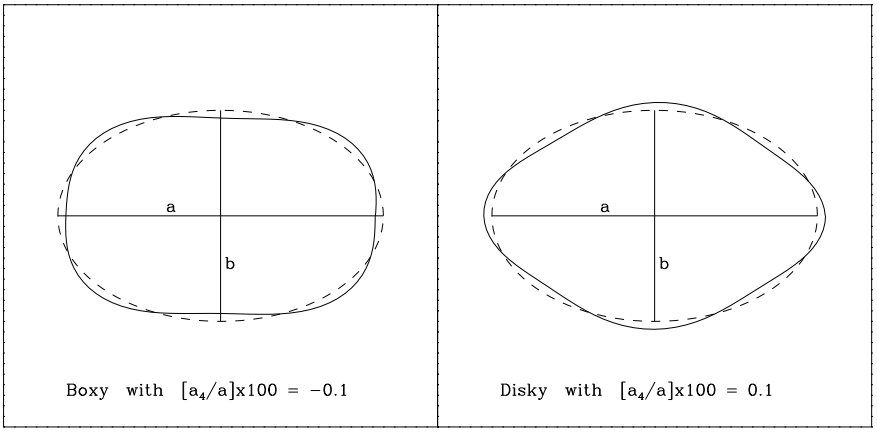

Figure 7.1: Illustration of a boxy ($a4 \times 100 = -0.1$) and a disky ($a4 \times 100 = -0.1$) isophotal shape compared to the corresponding ellipse (dashed). a and b is the long and short axis, respectively. Figure kindly provided by T. Naab

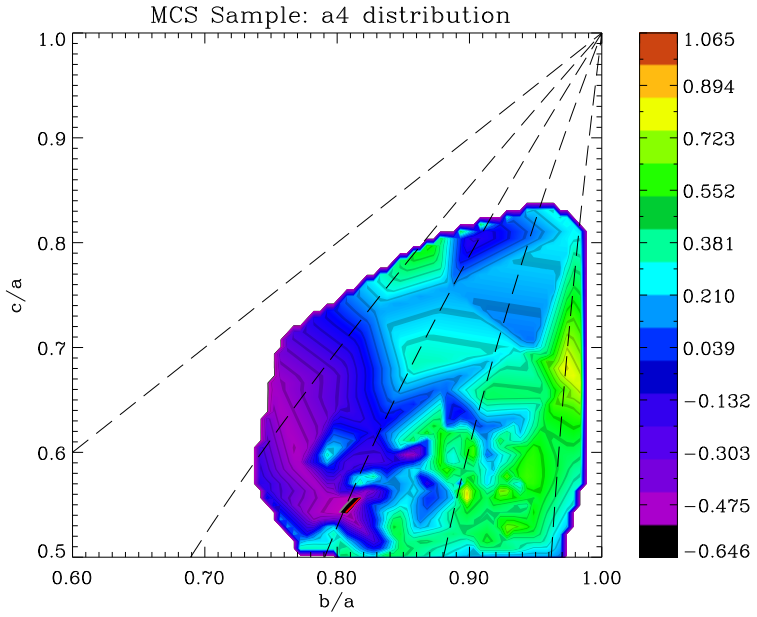

Figure 7.2: Distribution of a4 in axis ratio space

reader to the thesis of Naab (2000)

7.2 Isophotal Shape of the Remnants

It is natural to assume that, taking projections effects into account, boxy isophotes origin from box orbits and disky isophotes from z-tube orbits, which are building up the disk.
If we examine the distribution of the a4 parameter in axis-ratio space, which is independent of the orbit classification, we already see that this simple picture is probably not true. If a4 would reflect the true orbital content than a4 should follow the traxiality lines smoothly. On the other hand a4 does not lead us too far from the truth, because the peak for negative (boxy) is located T=0.5, where the box orbits are most common and the positive peak is also located where we would expect it at T=0. The space in between however is a mess. We can now plot the Box orbit to Z-Tube ratio in each remnant with respect to the a4 values. The results are shown in Fig. 7.3. While we could argue that a correlation for the 1:1 and 2:1 mergers is visible the 3:1 and 4:1 have become indifferent to their box orbit content, which can amount to a significant number. It is true however that the fraction z-tubes to the total fraction has increased in the 3:1 and 4:1 mergers, because the x-tubes become less and less important. We do not find any significant correlation between isophotal shape and x-tube content, though.

Disky isophotes are supposed to come from disk-like components in elliptical galaxies, but do these components really look like a disk. We compare the density shapes in Fig. 7.4. We plot the density projections of an exponential disk, an exponential disk plus a bulge and three remnants from 1:1, 3:1 and 4:1 simulation respectively. It is consistent with the simple assertion that the higher the mass ratio between the merger partners, the more does the disk of the more massive partner stay intact. The z-tube distribution of the 1:1 merger is much more dispersed than the one of the 4:1 merger. Also

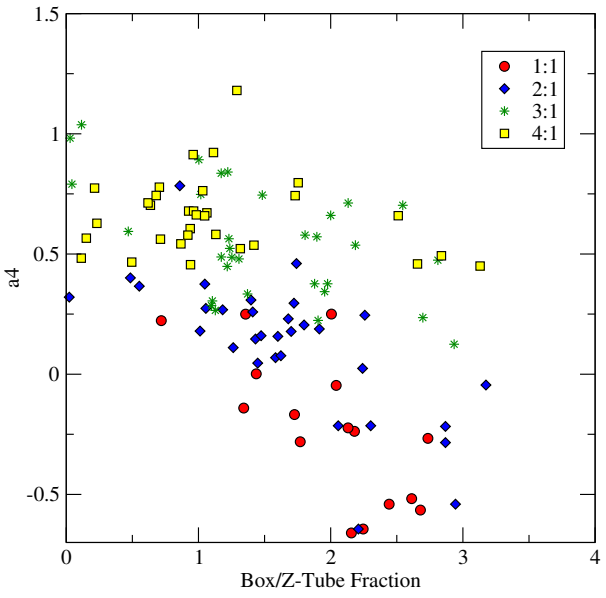

Figure 7.3: Correlation between the a4 paramter and the box to z-tube ratio in the remnants

Table 7.1: Mean values for the isophotal shape parameter for different orbit population extracted from three test remnants.

Test Case	Z-Tubes $a4_{mean}$	Non Resonant Box	All boxes	Boxes + Z-Tube	Complete Remnant
exp disk	0.537694				
exp. disk + bulge	1.03698				
1:1	-4.256	0.005	0.0006	-0.021	-0.556
3:1	-3.576	0.059	0.075	0.460	0.809
4:1	-1.594	-0.064	-0.057	0.289	0.526

consistently the hole in the center of the disk-like component is bigger for the equal mass merger. The center is filled with box orbits, which we plotted in Fig. 7.5.
It is instructive to look at the isophotal shape of the presented subsets of particles. The results are summarized in Fig. 7.6. As has been reported before the exponential disk appears boxy under $\approx 20\%$ of the projections. If we add the bulge almost all disky projections vanish. However, the projection of our puffy 'disks' extracted from the remnants are almost all boxy. It is therefore not correct to say that, at least in the numerical remnants, disky isophotes originate from disky components. It is also true, that the average value for $a4_{eff}$ is increasing with mass ratio, but in absolute values even the 4:1 disk is still boxy. The distribution of the isophotal shape parameter for the boxes are displayed in Fig. . The surprising result is that their isophotal shape is rather neutral and not boxy. In the 3:1 remnant they are even biased to the disky side. When we add the resonant box orbits to non resonant population, we see that the isophotes are not affected significantly in the 1:1 and 4:1 remnant, but appear even more disky in the 3:1 remnant (7.7). Interestingly when we superpose the box orbits and the z-tubes hte isophotes become disky and become close to what we see for the complete remnant. The average values for th a4 parameter are summarized in Table 7.1.

7.3 Discussion

We can conclude from this simple analysis, that there is no one component which can attribute for a disky isophotal shape. If the disk-like components present in the remnants would resemble an exponential disk only one-fifth of the projections would appear boxy. But we find that 80 % of the projections of the disk-like features have actually boxy projections. When the disks are superposed with centrally concentrated populations, in the case of the remnant the box orbits, and in the case of the exponential disk, the bulge, the projections become much more disky. Indeed when we compare the average values of a4, we have already obtained the right ranking in isophotal shape. The 3:1 remnant is more disky than the 4:1 remnant and the 1:1 remnant is a boxy remnant. We could not have deduced this from the disk-like compenent alone, though. The z-tube isophotal shape for the 4:1 remnant is more disky than the one of the 3:1 remnant. Strangely the box content of the 3:1 remnant already appears disky. We can now reveal that the z-tube fraction of the examined 4:1 remnant is 45 % while it is only 31 % in the 3:1 remnant. In part this demonstrates at least for our test remnants the insensitivity of a4 on box/z-tube ratio. We checked if the box orbits in the center of the 3:1 remnant are misclassified z-tubes or x-tubes, but they do not show any kind of rotation, hence we must believe that they are some kind of radial orbits.
But our test case, the exponential disk plus a bulge, clearly demonstrates that a disk component can be made more disky by adding a spherical component to its center. Again we have to stress that the equation box orbits boxy isophotes is not completely true for the remnants. We cannot make a final verdict on the isophotal problem, because for we chose to classify only 40 % of the remnant and the outer parts of the remnant can not be neglected.

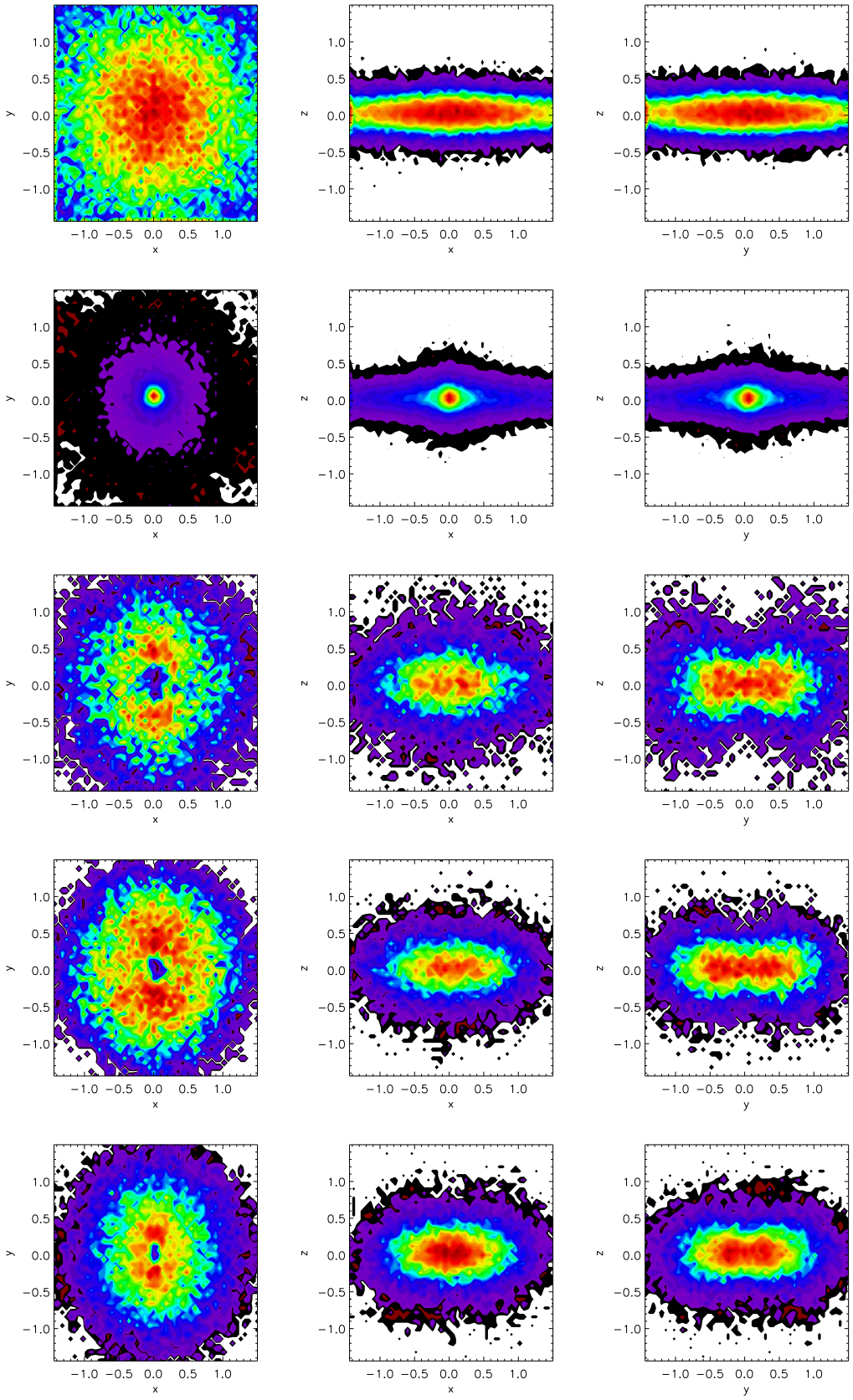

Figure 7.4: Projected density distribution of particles classified as z-tubes. From top to bottom: exponential disk, exponential disk plus bulge, z-tube component of a 1:1 merger, z-tube component of a 3:1 merger, z-tube component of a 4:1 merger.

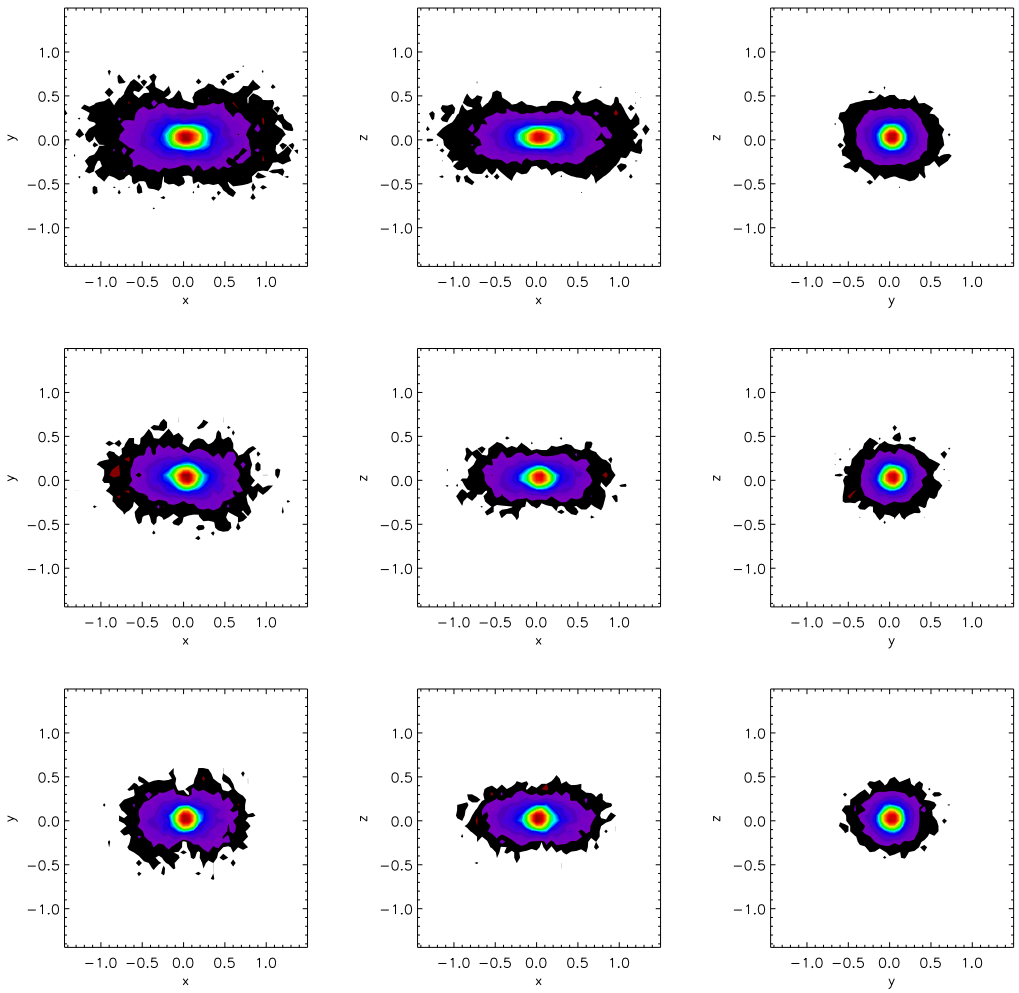

Figure 7.5: Projected density distribution of the particles classified as non resonant boxes. From top to bottom: exponential disk, exponential disk plus bulge, z-tube component of a 1:1 merger, z-tube component of a 3:1 merger, z-tube component of a 4:1 merger. Errors are indicated by a cross

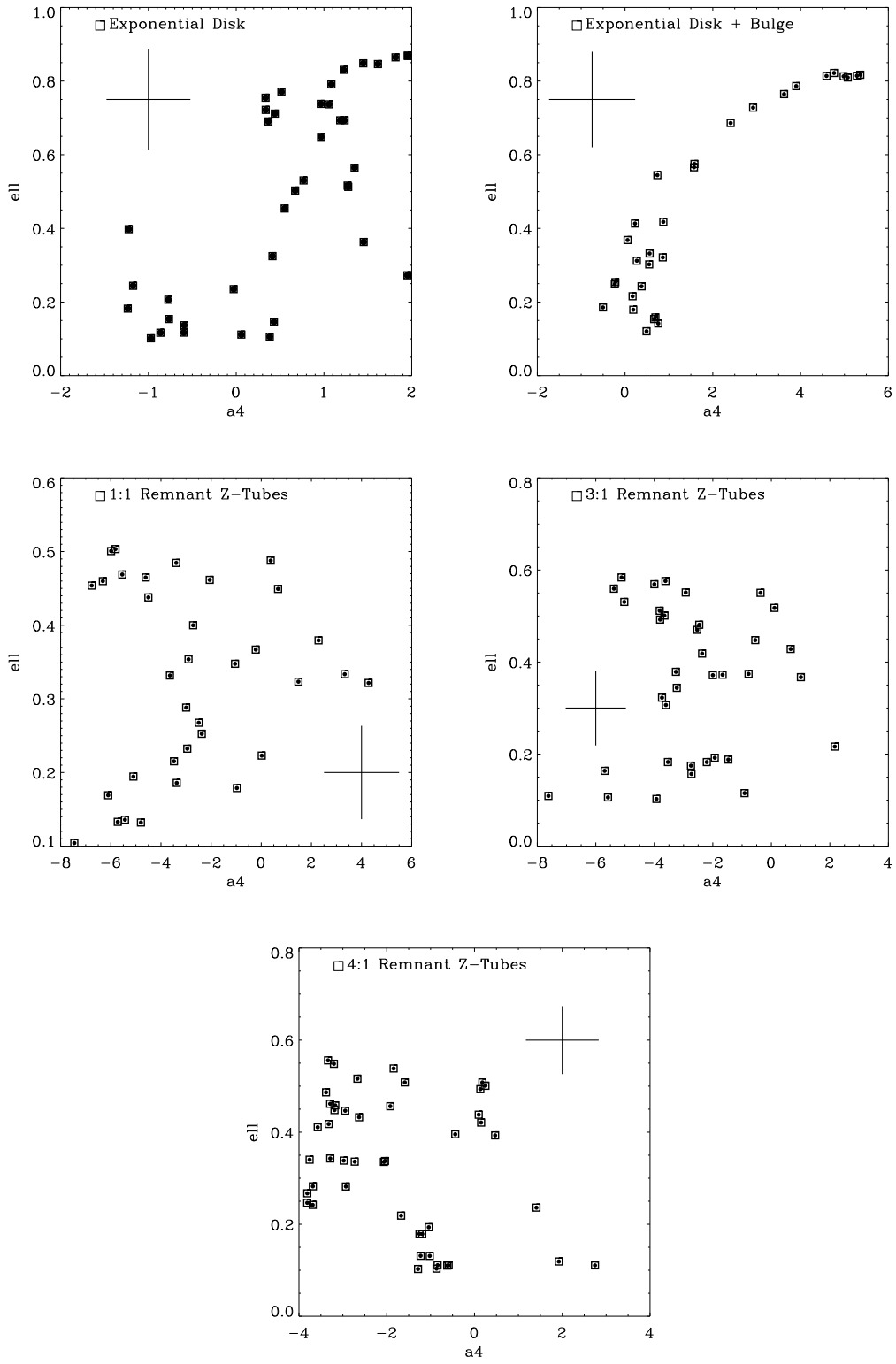

Figure 7.6: Results of 50 random projections for the effective isophotal shape parameter for the same remnants like in Fig. 7.4. Errors are indicated

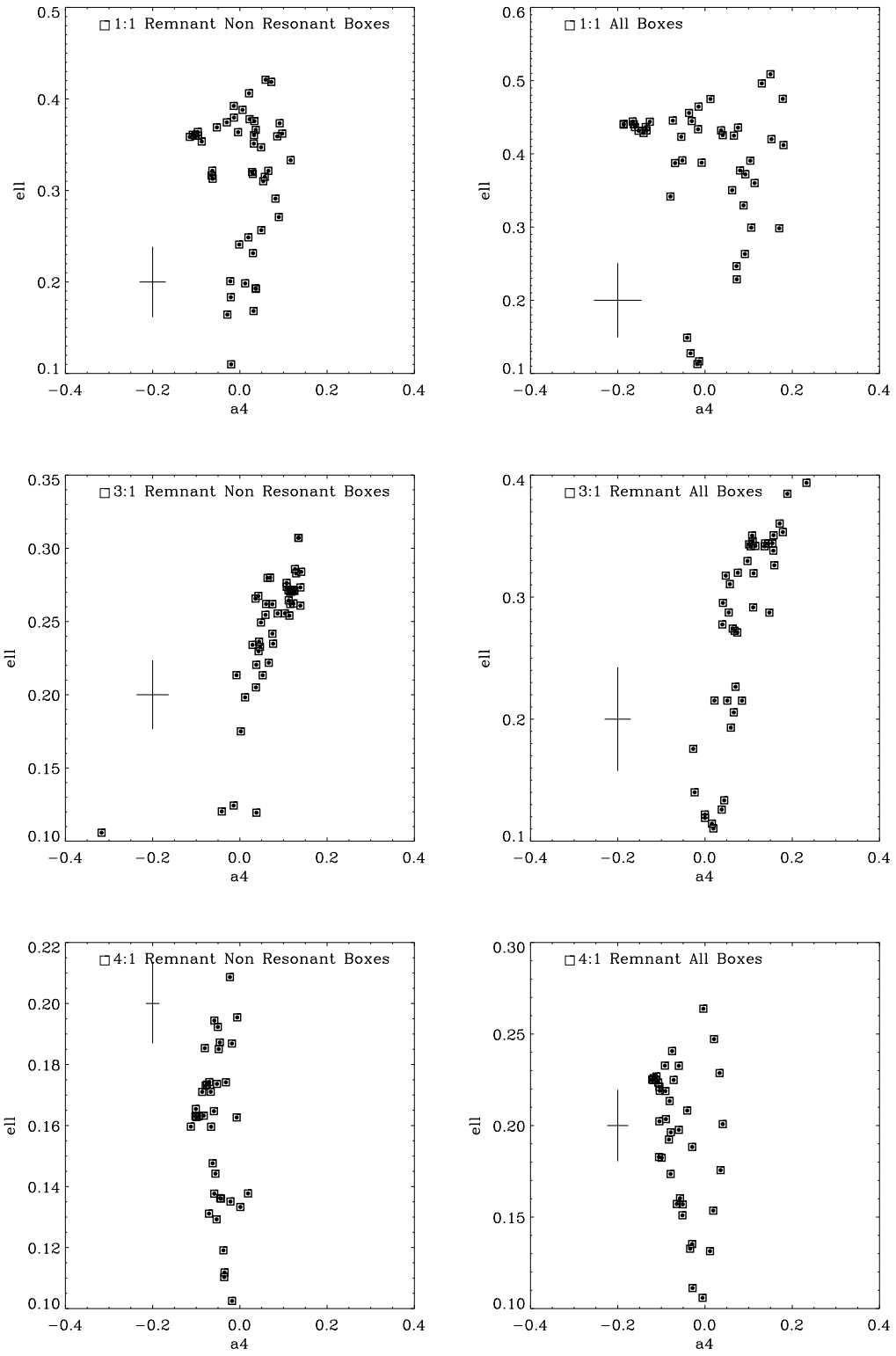

Figure 7.7: Results for the A4 shape parameter for the non resonant boxes (left column) and all box orbits (right column). Same Remnants as before

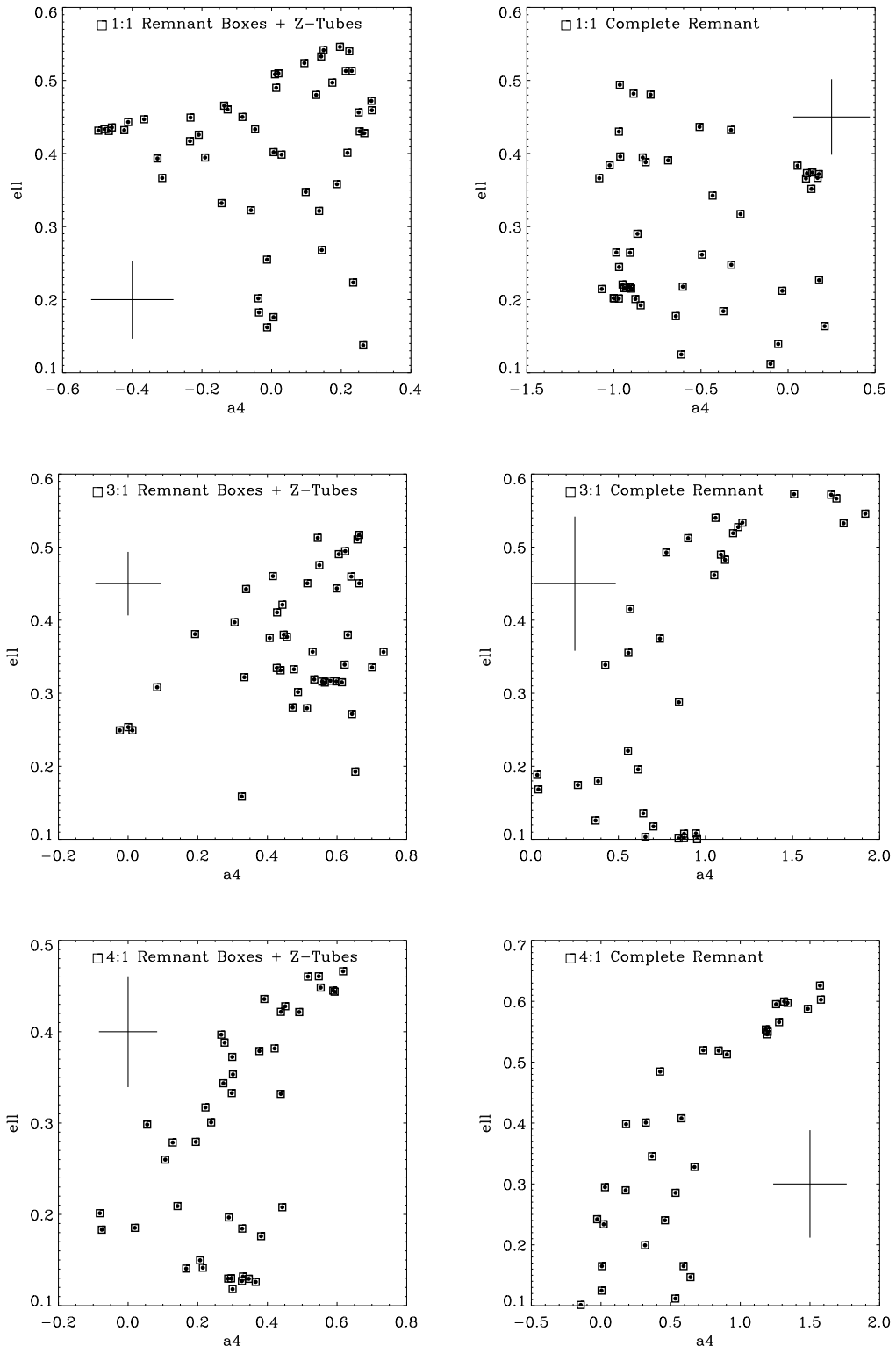

Figure 7.8: Results for the A4 shape parameter for the box and the z-tube component superposed (left column) and isophotal shapes for the complete remnant (right column). Same Remnants as before.

Chapter 8

Measurements of h_3 in merger remnants

The light which reaches from external galaxies is a superposition of the unresolved spectra of their individual stars. The individual stars, however, will have different line of sight velocities v_{los}. Their spectra will therefore be shifted. The composite spectra will appear broadened. We can quantify the contribution of each star by defining the line-of-sight-velocity distribution, in short LOSVD, $F(v_{los})$. The analysis for the extraction of the LOSVD are beyond the scope of this thesis and we refer the reader to binney Merrifield for an introduction.
We are concerned with the moments of the LOSVD. The first moment is just the mean velocity

$$\bar{v}_{los} = \int dv_{los} v_{los} F(v_{los}). \tag{8.1}$$

The second moment is the velocity dispersion

$$\sigma^2_{los} = \int dv_{los} (v_{los} - v_{los})^2 F(v_{los}). \tag{8.2}$$

The simplest approach is to assume that LOSVD is of Gaussian form. To determine now v_{los} and σ_{los} we would need to fit the Fourier transformed functional form of $F(v_{los})$ to the Fourier transformed spectral data. However, these are only the first two moments. We fully parametrize $F(v_{los})$ by the moment equation

$$\mu_k = \int dv_{los} (v_{los} - \bar{v}_{los})^k F(v_{los}) \tag{8.3}$$

The shape parameters of the LOSVD are defined as

$$\xi_k \equiv \mu_k / \sigma^k_{los}. \tag{8.4}$$

The division by the velociy dispersion makes them dimensionless. Most important four our purposes are ξ_3 and ξ_4, which are called skewness and kurtosis of the LOSVD. The skewness measures the asymmetric deviation of the LOSVD from a Gaussian, while the kurtosis measures the symmetric deviation from a Gaussian. The measurements of true moments are prone to large errors coming from v_{los}, which are far from the mean value. Therefore the best way to determine the higher moments of Eq. 8.3 is by fitting a truncated Gauss-Hermite series of the form

$$F_{TGH}(v_{los}) \propto e^{-\frac{1}{2}\omega^2} [1 + \sum_{k=3}^{n} h_k H_k(\omega)] \tag{8.5}$$

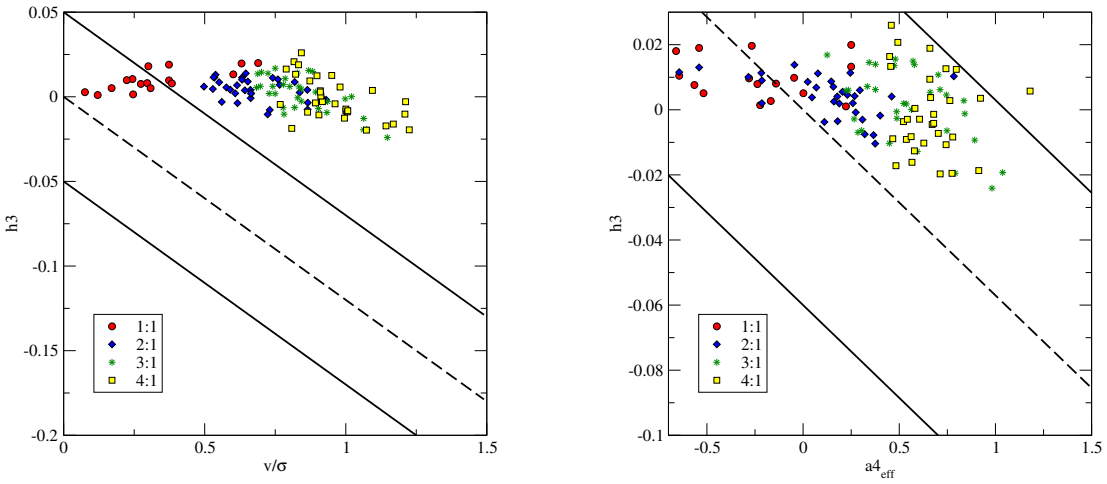

Figure 8.1: Comparison of h_3 correlations as found by Bender et al. (1994) to the full sample of close encounters.

pioneered by Gerhard (1993) and van der Marel & Franx (1993). Normally the truncation is already set at n=4. The h_k are constant coefficients. Note that the h_k and the ξ_k are not identical, but they contain similar information and are used synonimously in most cases.
In observed elliptical galaxies only significant correlations for h_3 have been found. We will therefore neglect h_4 in the following discussion.

8.1 Global Correlations

Bender et al. (1994) were the first to point out that in the sample of elliptcial galaxies they surveyed $< h_3 >$ and the isophotal shape parameter a4 on one hand and $< h_3 >$ and v/σ_m on the other hand show a strong correlation. They obtained a rough fit

$$< h_3 > \approx -0.12 v/\sigma_m. \tag{8.6}$$

In general they did not find significant measurements over the 1σ level for $< h_3 >> 0$. They point out that not only disky ellipticals follow this relation, but also the boxy ellipticals. An explanation for a mean $h_3 < 0$ is easily found by a two component system of a rotational system, like a disk and a not rotational, like a bulge. The mean motion of the 'bulge' will skew the Gaussian towards velocities, which are less than the mean and result in a negative h_3. As has been reported before the merger remants do not follow theses relations. We show the relations in the remnants averaged over 50 projections. The tendency is that too positive values of h_3 are found in the remnant for a given v/σ, as can be seen from Fig. 8.1.
Our 1:1 mergers show a richer variety of orbital classes than the 3:1 or 4:1 mergers, but the unequal mass mergers fail to lie on the correlation as much as the 1:1 mergers. Although the observed correlation is not reproduced by the remants, there is a tight correlation between $< h_3 >$ and the box to z-tube ratio in the remnants. It is a true global correlation in the sense that no merger ratio forms an isolated correlation, like e.g. for σ_0. As can be seen in Fig. 8.2 negative values appear foremost in oblate remnants which are z-tube dominated, but they are never reaching oberved values

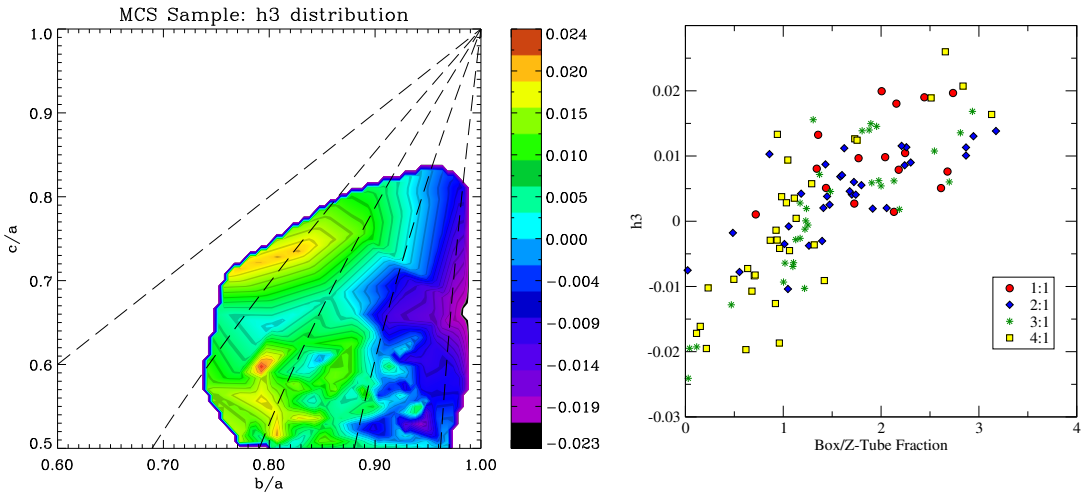

Figure 8.2: Left: Distribution of h_3 values for merger remnants with different axis ratios. Right: h_3 coefficient in remnants with different ratios between box orbits and z-tubes

of $< h_3 > \approx -0.1$. Although the tendency agrees with theoretical expectations which are found for distribution functions of axisymmetric rotating models (Dehnen & Gerhard, 1993,Dehnen & Gerhard, 1994,Evans & de Zeeuw, 1994), the rotating component seems not to be strong enough in the remnants compared to what is found in ellipticals (see Scorza & Bender (1995) for a thorough discussion of disky structures and their kinematical features in elliptical galaxies). If this problem can be alleviated by primordial disks or mergers with dissipation is possible and must be tested.

What can we learn if we are dissecting a 3:1 merger into different dynamical constituents? We are comparing the results of the observed correlations with the values we extract from the z-tube component, the box component, box and z-tube component superposed, all orbits which run through our classification scheme (for a 3:1 remnant this amounts to 42666 particles) and the complete remnant (106666 particles). We immediately see from Fig. 8.3 that the full solution to our problem lies outside the classified domain. Significant positive values for $< h_3 >$ appear in the total remnant rather than in the classified sample. However, we know now that we have to look into the outer parts of the remnants to explain the exact amount of discrepancies with what is found in the observations.
Still there are some poins to note. The box orbits have an $< h_3 > \approx 0$ for all projections which we expect for a component with no preferred rotationial direction. Again we observe that disky isophotes appear when we superpose box orbits and z-tubes. Consistently we find significant negative $< h_3 >$ for the z-tube component, which shows significant rotation for almost all projections. Strangely however it follows rather well the observed correlations for $< h_3 >$ and v/σ. We checked if this is a coincidental isolated find. It is not. Actually all z-tube components of 3:1 and 4:1 mergers follow the correlation. They do not only follow the correlation, but also produce $< h_3 >$ values in the exact range, where they are found in observations ($0.02 < h_3 < -0.15$). Some examples are given in Fig. 8.4. They do not simultaneously fit the correlation for a4 and therefore cannot account for the observations alone. But as seen before, as soon as another component is superposed the correlation vanishes. We can tentatively make two conclusions from this finding: 1. the correlation is a projection effect. 2. we

need only one component to get significant negative $< h_3 >$. This component looks like a puffy disk. We need to investigate further if a general process is populating the z-tubes in such a way the that it fits the v/σ correlation.

8.2 h_3 and the mean velocity

There is a notorious discrepancy between merger remnants and observed elliptical galaxies: h_3 and the mean velocity have opposite signs. This is not found in merger remnants in general. Only retrograde mergers seem to produce such a correlation, but they can only account for 50 % of the elliptical population. We will study this problem in the merger remnants and exploit the fact that there seems to be a global correlation between box to z-tube ratio and h_3 in the merger remnants. We are extracting as before just the z-tubes and instead of examining many projections, we are focussing on the major axis projection. We plot the radial profiles of the mean velocities and h_3 for a couple of remnants. We see that in contrast with the total remnant the anti-correlation of signs is conserved for the z-tube orbits (see Fig. 8.5). We can quantify this in a simple way: for each radial bin we multiply the value of h_3 and the mean velocity. If the product is less than zero, we have a valid correlation, if it is positive then h_3 and v_{mean} have the same sign. The results are shown in two histogramms 8.6. Clearly the z-tubes peak at one or two wrong correlations and can therefore be said to correlate very well. For the whole remnant the picture is more complicated, almost every amount of wrong correlation along the major axis is found. Now we correlate the number of wrong correlations in the rotation curve with the box to z-tube ratio (Fig. 8.7).
The trend is clearly seen. The more box orbits are found in the center of the remnant, the more h_3 and v_{mean} are decoupling. The 1:1 remnants are spoiling this relation a little bit. Probably other types of orbits, most notably the x-tubes will also introduce a diversification in the h_3 profile. Indeed as presumed the dissipationless merger have too many peculiar kinematical features to coinincide with observations of elliptical galaxies.

8.3 Discussion

We have highlighted two current problems in merger simulations concerning the disagreement with observations of h_3 in real elliptical galaxies. Both problems seem to be related. While we can not completely account for the high positive value of a complete remnant, because our classification does not reach out that far, we can resolve the disagreement concerning the anti-correlation of the signs of h_3 and the mean velocity. The central component of box orbits is clearly destroying this relation, which for the z-tube component of the remnants alone is conserved. The amount of anti-correlation is proportional to the amount of box orbits present in the center of the remnant. Interestingly the z-tube component has the correct anti-correlation of the signs, but follows also the global correlations of ellipticals found by Bender et al. (1994) for v/σ_0, albeit not for a4. The dense central component, which originates from the bulges of the progenitors seems to pose a problem for a simple merging picture as it introduces too peculiar features in the center of the remnant. However, the bulge is needed to fulfill phase space constraints of the central density of ellipticals as found in nature. The resolution of this conflict is not clear, but needs to be addressed in the future.

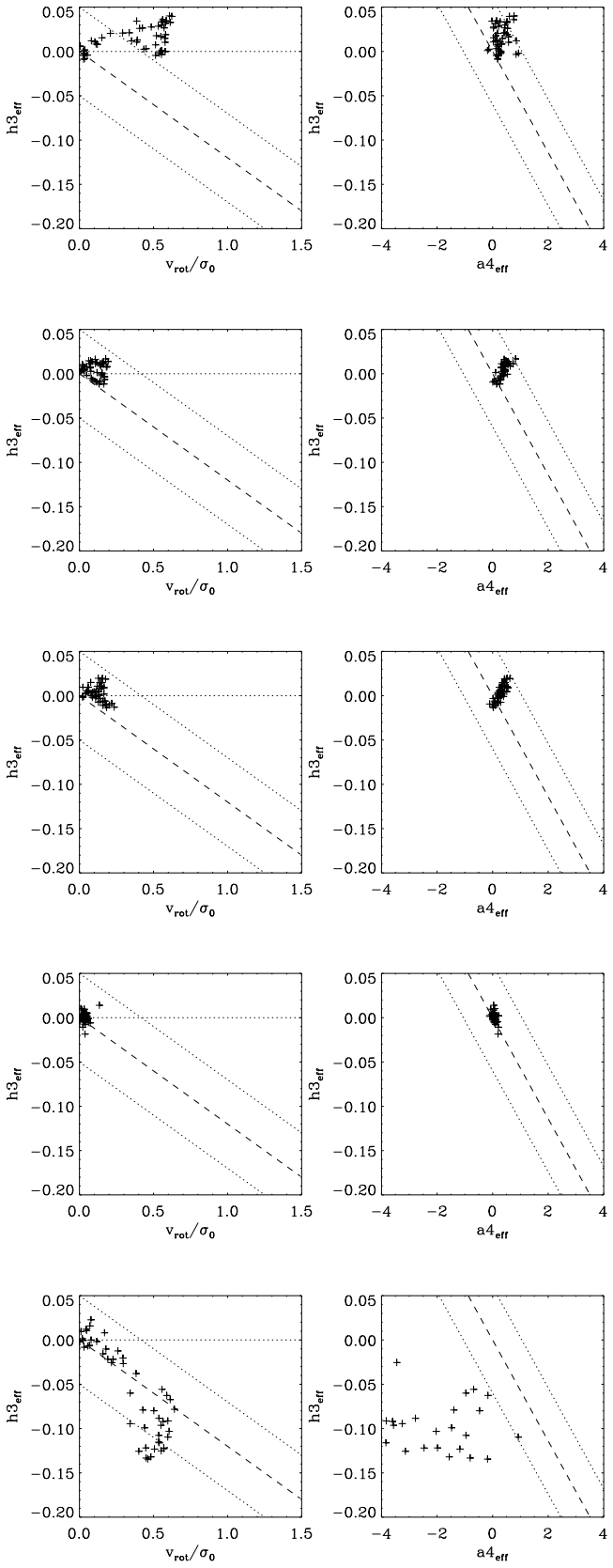

Figure 8.3: Comparison of h_3 correlations as found by Bender et al. (1994) to various constituents of the same 3:1 remnant as found by our orbital classification. From top to bottom: Complete remnant , all orbits classified, all box orbits and z-tubes superposed, non resonant box orbits, z-tubes.

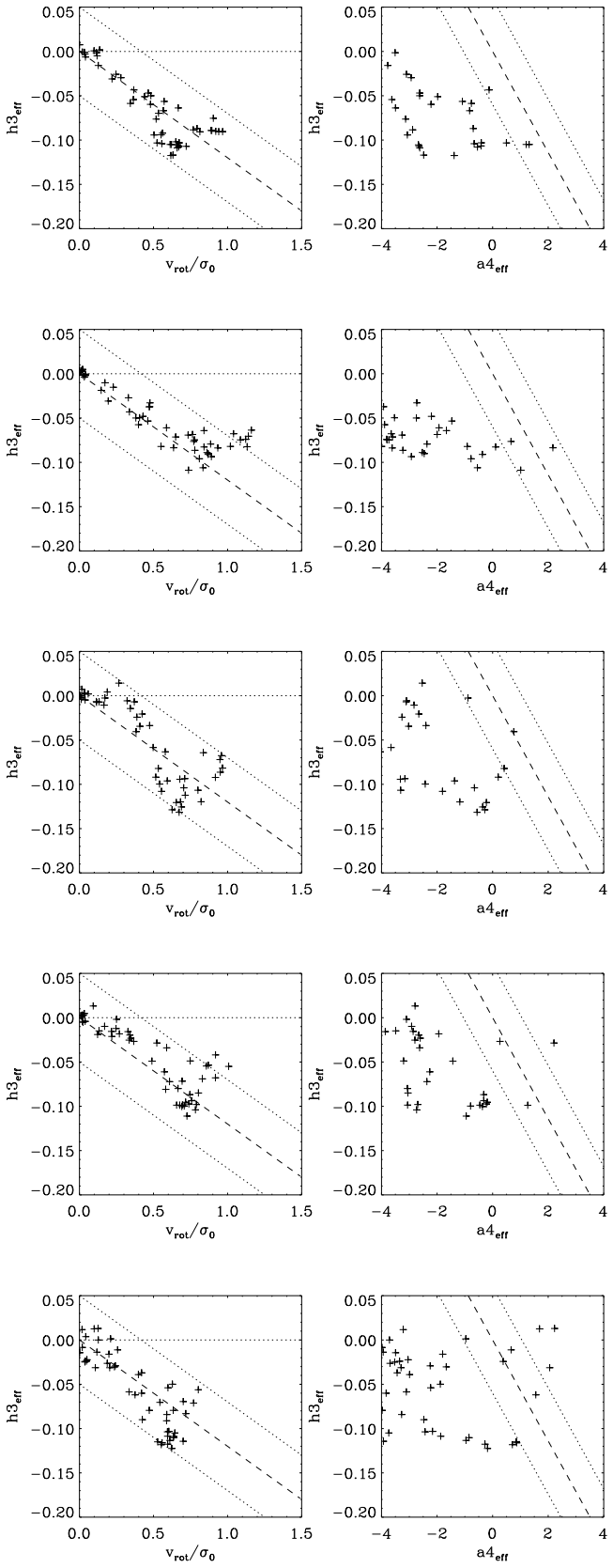

Figure 8.4: Comparison of h_3 correlations as found by Bender et al. (1994) to z-tube populations found in two 3:1 remnants (first two rows) and three 4:1 remnants.

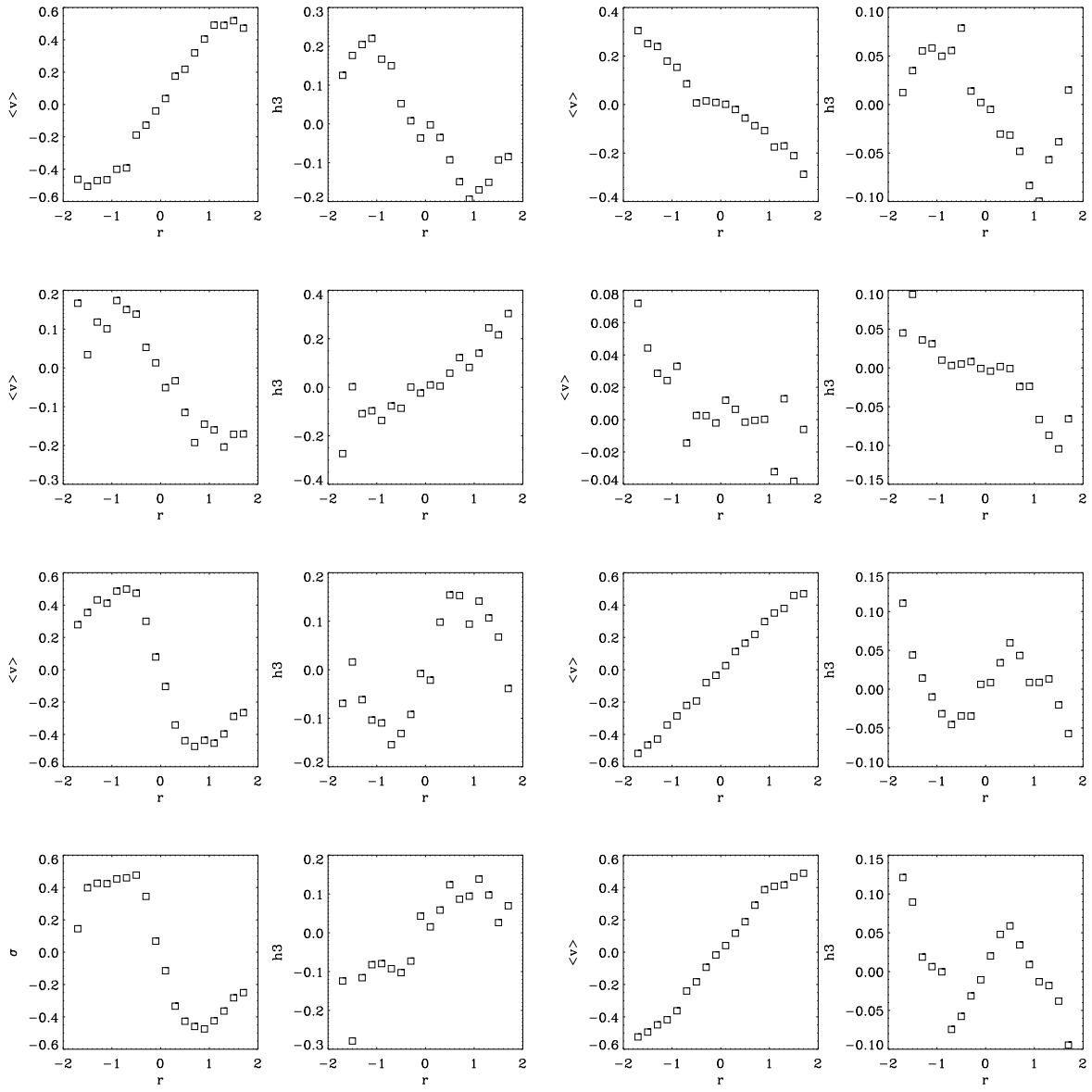

Figure 8.5: Radial profiles for mean velocity and h_3, left, respectively right panel each plot. Left column: particles classified as z-tubes. Right column: complete remnant

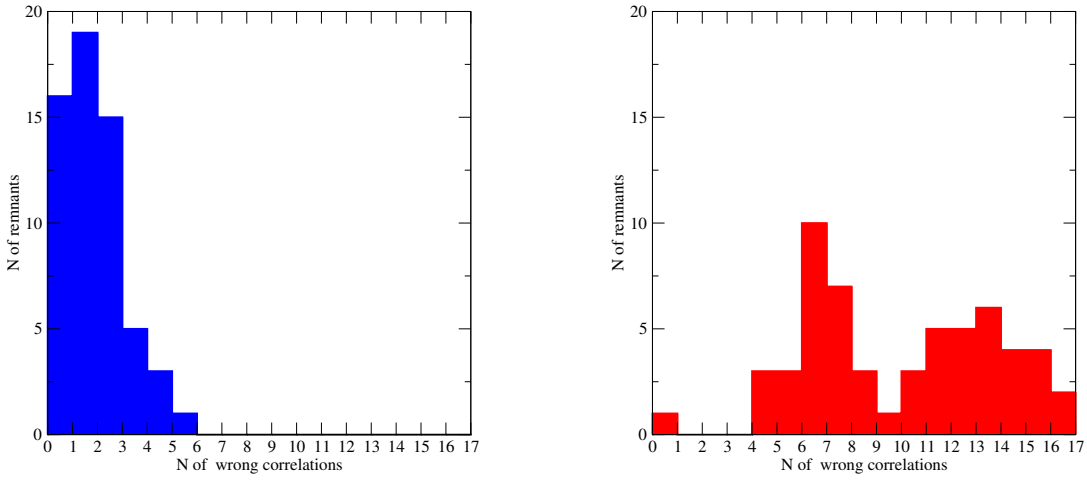

Figure 8.6: Histogram of wrong correlations in one radial profile between $< v >$ and h_3 at the same radial bin. Left plot: z-tube component. Right plot: complete remnants

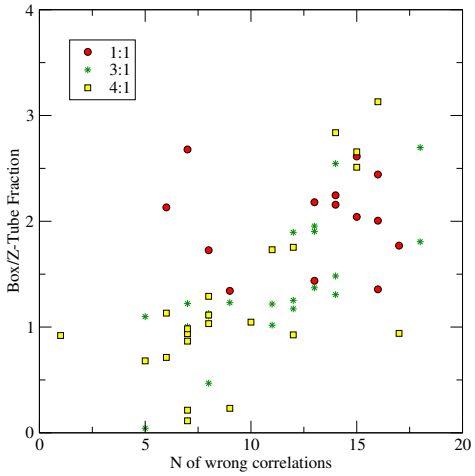

Figure 8.7: Correlation between the amount of non-correlation between h_3 and $< v >$ and box to z-tube fraction in the same remnant

Chapter 9

Conclusions and Outlook

9.1 Conclusions

We have examined a large set of dissipationless merger remnants of disk-disk encounters to relate observational features to their detailed orbital content. We tested our extraction method which is a combination of spectral analysis and a self-consistent field method and find that the particles extracted exhibit the kinematical tell-tale features we would expect theoretically of the assigned orbit class.

In a statistical analysis we tried to relate the orbital content of a given merger remnant with its intrinsic shape. Again our findings are in very good agreement with theoretical expectations. Trends of orbital occupation numbers found in analytical potentials with the Schwarzschild method are in agreement for most orbit classes, but detailed discrepancies exist, which would be expected, because the analytical form of the potentials does not coincide with the N-body potential of the merger remants.

The pathology of orbital content seems to change when the encounters are calculated with a wider pericenter distance, which is more likely to occur in cosmological CDM simulations. As the sample of the wide encounters is smaller, we do not know yet the statistical significance of this trend.

The isophotal shape of a merger remnant is connected to its orbital content, but not in a one-to-one correspondence in the sense that box orbits are causing boxy isophotes and z-tube orbits are the reason for disky isophotes. We showed and confirm an earlier conjecture that this even not true for an exponential disk, which appears boxy under certain projections. If a dense central component is added, like a bulge, the boxy projections are vanishing. Analogously if the box orbit content is superposed over the disk-like component more disky projections are the result. This seems to explain the insensitivity of the isophotal shape on orbit fraction in 3:1 and 4:1 remnants, where the z-tube component is overpowering the boxes. In 1:1 and 2:1 remnants the detailed ratio of both type of orbits matters and a correlation is visible.

Measurements of h3 in merger remants pose a severe problem for the merger hypothesis of galaxy formation. Normally the sign of h3 and the mean velocity are anti-correlated. We could trace the problem to presence of too many box orbits in the center of the remnants, which are destroying this anti-correlation. The disk-like component follows the anti-correlation nicely. Additionaly the z-tube population fits the observed correlations between h3 and $v\sigma_0$ by projection. We conclude that ellipticals have the same features as puffy disks found in our remnants. Bulges in the progenitors of merger events are problematic from the perspective that they produce too many box orbits in the center of the remnant.

9.2 Outlook

There is more to merger remnants than meets the eye. But this is not only true for merger remnants. With the advent of higher and higher resolution in simulations of collisionless systems the analysis of their orbital content becomes more and more feasible. If we can believe that the orbital structure of a galaxy is a fossil record of its formation history, than we have to assume that N-body simulations of galaxy formation, cosmological or in isolation, reproduce this structure. Whenever they fail, we know that our understanding of galaxy formation is not complete.

The simulations presented are not yet at the stage where we could exclude or confirm a certain formation mechanism, like the merger hypothesis. Firstly, not all important physical processes are included in simulations, like dissipation and star formation. One of the biggest challenges would be to include a black hole into the center of the merging spiral galaxies, which is known to change the trajectory of a star in the center considerably. This is such a challenge, because a large range of dynamical times (approximately six orders of magnitude) has to be crossed. Secondly the initial encounter parameters need to be adjusted to the ones found in large scale cosmological simulations. Good enough statistics then will give an answer, if we found the right formation mechanism.

N-body simulations are of course only one side of the understanding of orbital structure of galaxies. They are worthless if we can not compare them to orbital content of real galaxies. This knowledge has been mainly improved by the Scharzschild method. In the future the SAURON project will give us a new wealth of detailed orbital information of elliptical galaxies, against which various formation scenarios can be tested. Maybe we will be able to distinguish ellipticals formed by monolithic collapse, disk-disk mergers, elliptical-disk mergers or multiple mergers. Apart from this zoological ordering, it might even be possible to distinguish between cosmological models by comparing the merger fractions as found in semi-analytical modelling and statistics we deduce from the fine-structure of the ellipticals.

There is also the point of comparing our classification method or further developments thereof with the Schwarzschild method. It should be very instructive if our remnants could be classified with a Schwarzschild code with or without using the kinematics of the remnant in a least-squares fit. Some of our remnants exhibit figure rotation. It is not yet clear, how exactly this will change the classification and if Schwarzschild codes can be adopted to such a case. N-body remnants would be ideal test cases.

We did not discuss chaotic dynamics, but they will have probably an impact on our results. When we will form merger remants in the future with higher central densities (possibly with gas) or black holes, we can not neglect this feature anymore. The shape of the remnant (or galaxy) determines the orbital structure which in turn influences the feeding of the black hole, more box orbit will more likely end in the black hole than tubes. Is there a lot of chaotic diffusion of the orbits which will in turn influence the shape of the galaxy, making it more axisymmetric or round? Diffusion times can be calculated by a spectral code, but as soon as we enter the realm of collision dominated system it is unclear how to extract these features out of N-body calculations.

We did not examine the evolution of the dark matter of the mergers more closely. If the orbital geometry is decisive in determining the orbital structure of the remnant will there be a correlation with the halo? Does the halo take up a significant amount of angular momentum and does it influence its spin paramter? There is a host of open questions.

We hope to have highlightened the importance of orbital structure as found in N-body simulations for the theory of galaxy formation or the evolution of collisionless systems in general. The application of orbit classification to various problems in theoretical astronomy should be able to identify the reason behind problems of formation mechanisms like mergers of spiral galaxies.

Appendix A

Individual Merger Fractions

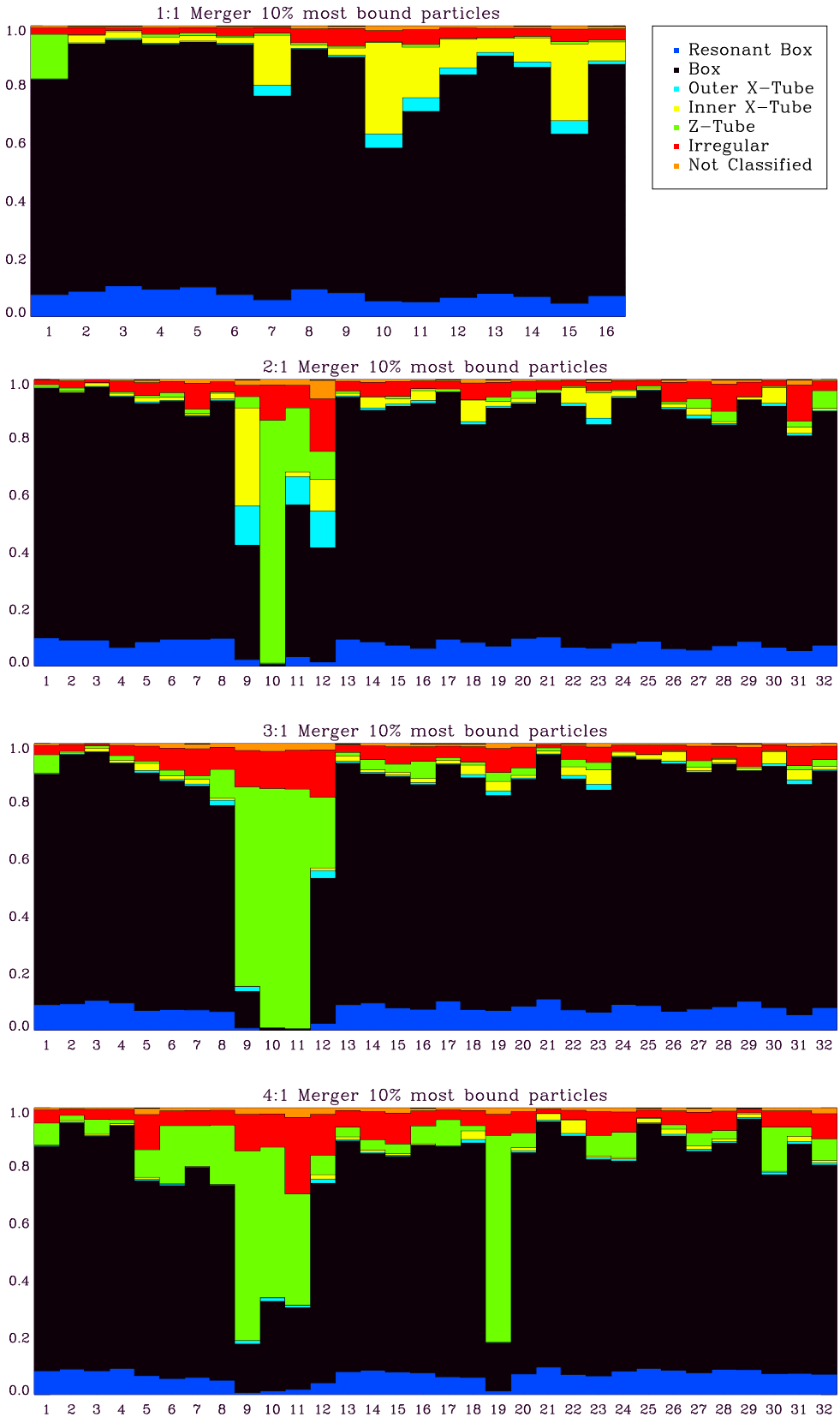

Figure A.1: Orbital statistics of individual merger remnants. Close encounters inner 10%

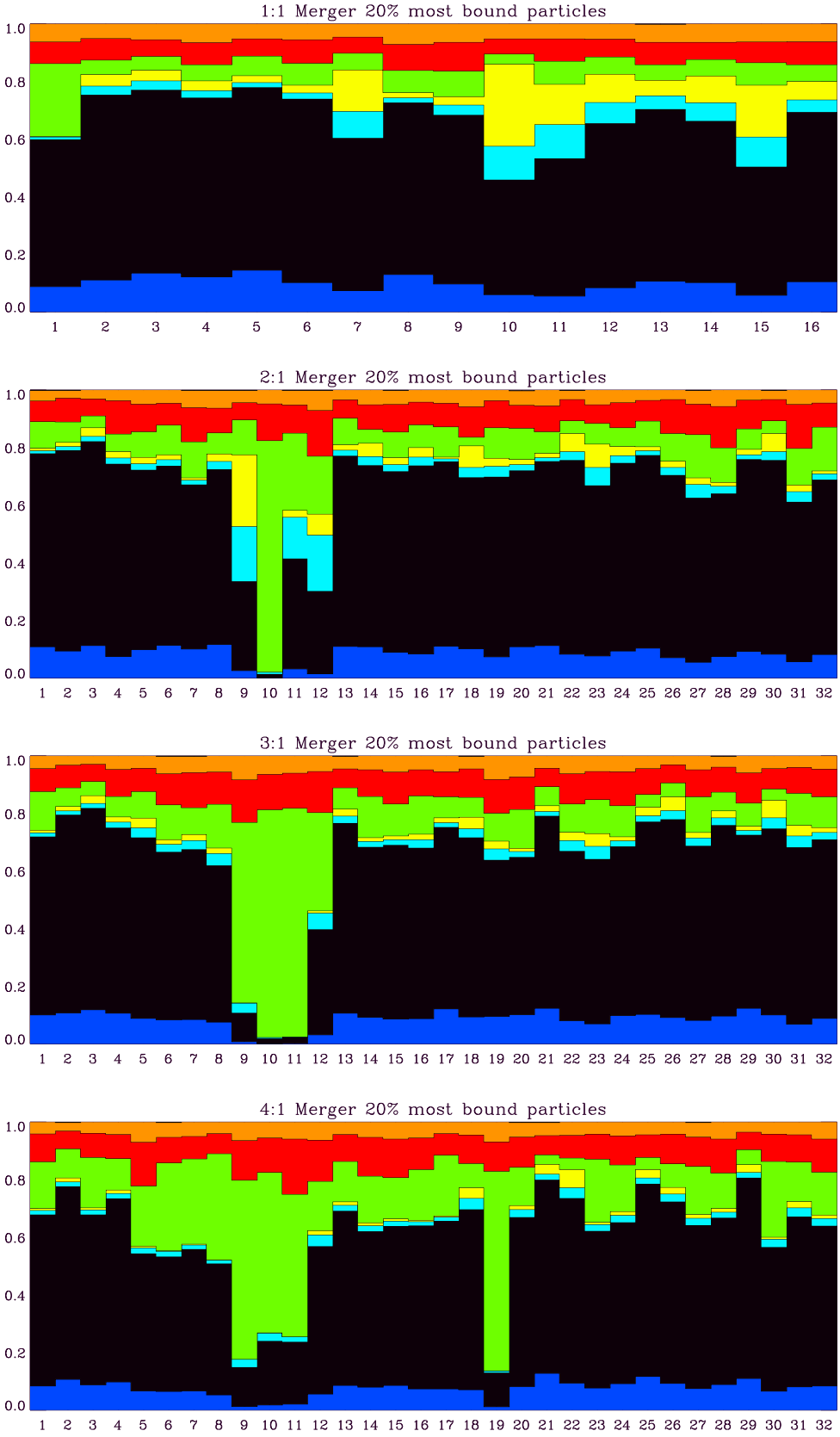

Figure A.2: Like before, but inner 20 %

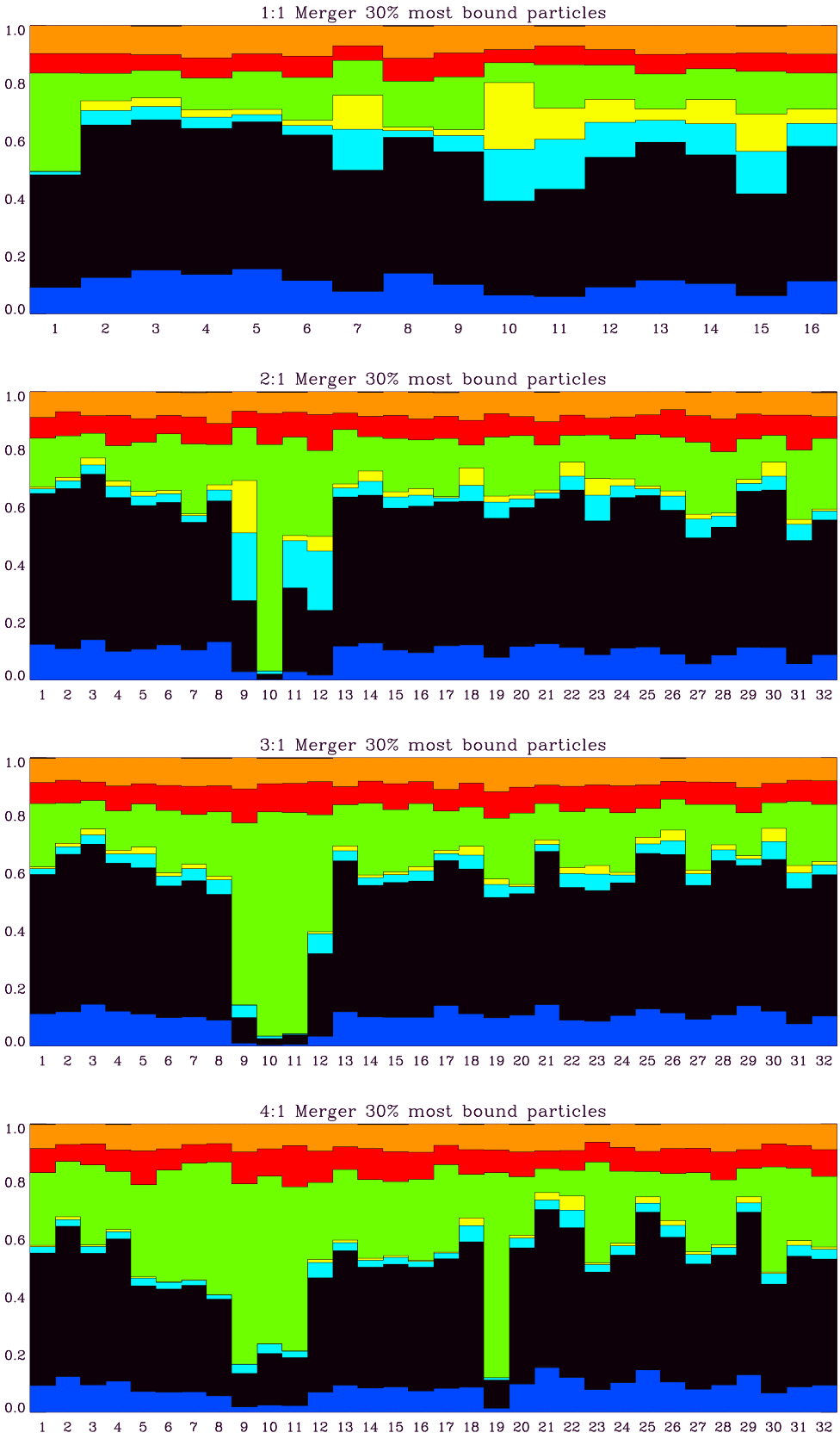

Figure A.3: Like before but inner 30 %

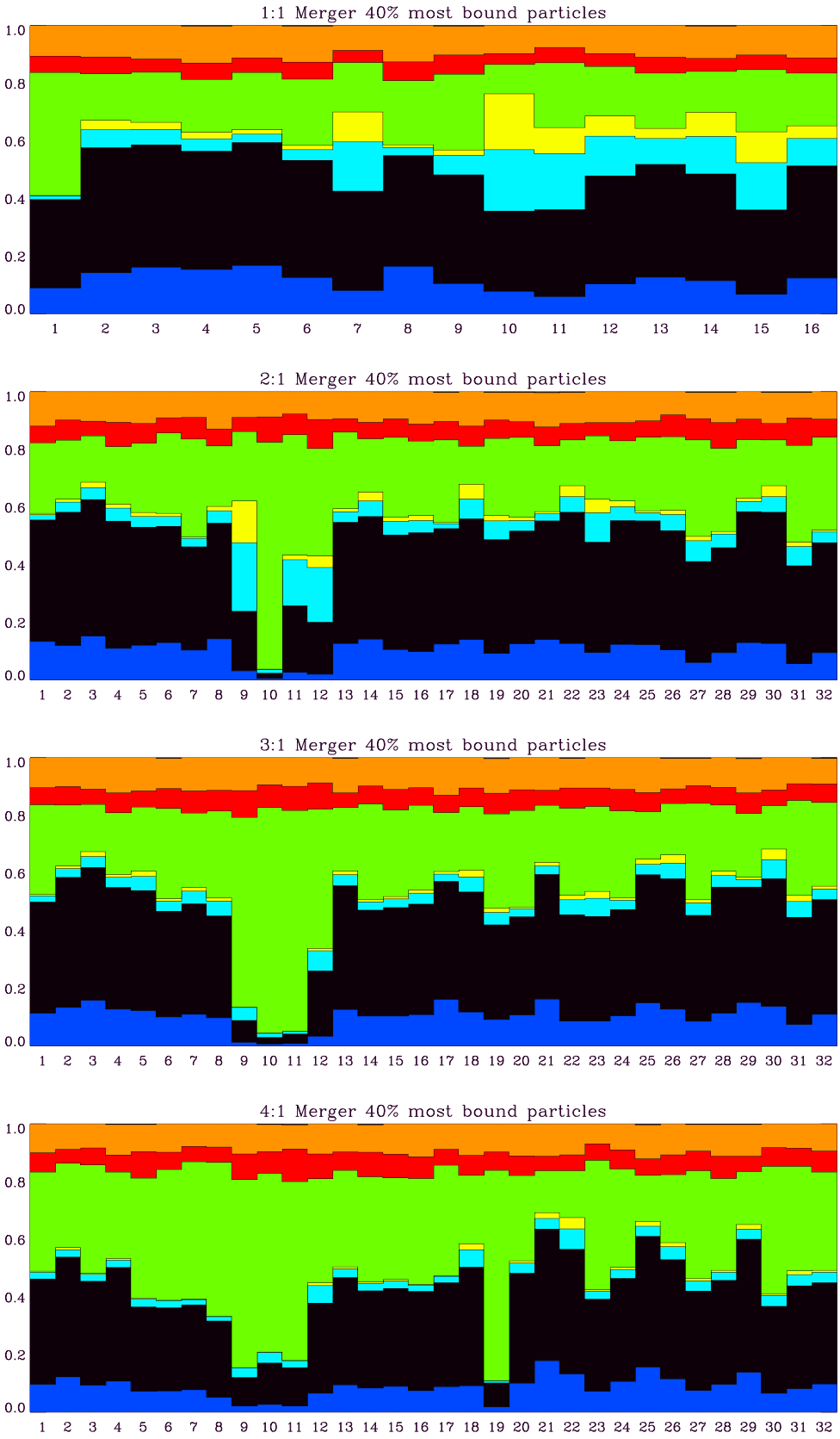

Figure A.4: Like before but inner 40 %

Bibliography

Arnold, R., de Zeeuw, P. T., Hunter, C.: 1994. Orbital Content and Velocity Fields of Triaxial Galaxies. *Monthly Notices of the Royal Astronomical Society*, **271**, 924–+.

Baes, M. Dejonghe, H.: 2002. The Hernquist model revisited: Completely analytical anisotropic dynamical models. *Astronomy and Astrophysics*, **393**, 485–497.

Barnes, J. White, S. D. M.: 1984. The response of a spheroid to a disc field or were bulges ever ellipticals? *Monthly Notices of the Royal Astronomical Society*, **211**, 753–765.

Barnes, J. E.: 1992. Transformations of galaxies. I - Mergers of equal-mass stellar disks. *Astrophysical Journal*, **393**, 484–507.

Barnes, J. E.: 1998. Dynamics of Galaxy Interactions. In *Saas-Fee Advanced Course 26: Galaxies: Interactions and Induced Star Formation*, Seiten 275–+.

Barnes, J. E. Hernquist, L.: 1996. Transformations of Galaxies. II. Gasdynamics in Merging Disk Galaxies. *Astrophysical Journal*, **471**, 115–+.

Bekki, K. Shioya, Y.: 1997. Formation of Boxy and Disky Elliptical Galaxies in Early Dissipative Mergers. *Astrophysical Journal Letters*, **478**, L17+.

Bender, R.: 1988. Velocity anisotropies and isophote shapes in elliptical galaxies. *Astronomy and Astrophysics*, **193**, L7–L10.

Bender, R., Doebereiner, S., Moellenhoff, C.: 1988. Isophote shapes of elliptical galaxies. I - The data. *Astronomy and Astrophysics Supplement Series*, **74**, 385–426.

Bender, R., Saglia, R. P., Gerhard, O. E.: 1994. Line-of-Sight Velocity Distributions of Elliptical Galaxies. *Monthly Notices of the Royal Astronomical Society*, **269**, 785–+.

Bendo, G. J. Barnes, J. E.: 2000. The line-of-sight velocity distributions of simulated merger remnants. *Monthly Notices of the Royal Astronomical Society*, **316**, 315–325.

Bertola, F. Capaccioli, M.: 1975. Dynamics of early type galaxies. I - The rotation curve of the elliptical galaxy NGC 4697. *Astrophysical Journal*, **200**, 439–445.

Binggeli, B.: 1980. On the intrinsic shape of elliptical galaxies. *Astronomy and Astrophysics*, **82**, 289–294.

Binney, J.: 1978. On the rotation of elliptical galaxies. *Monthly Notices of the Royal Astronomical Society*, **183**, 501–514.

Binney, J.: 1985. Testing for triaxiality with kinematic data. *Monthly Notices of the Royal Astronomical Society*, **212**, 767–781.

BINNEY, J. MAMON, G. A.: 1982. M/L and velocity anisotropy from observations of spherical galaxies, or must M87 have a massive black hole. *Monthly Notices of the Royal Astronomical Society*, **200**, 361–375.

BINNEY, J. SPERGEL, D.: 1984a. Spectral stellar dynamics. II - The action integrals. *Monthly Notices of the Royal Astronomical Society*, **206**, 159–177.

BINNEY, J. SPERGEL, D.: 1984b. Spectral stellar dynamics. ii - the action integrals. *Monthly Notices of the Royal Astronomical Society*, **206**, 159–177.

BINNEY, J. TREMAINE, S.: 1987. *Galactic Dynamics*. Princeton University Press.

BISHOP, J. L.: 1987. Axisymmetric shell models with Staeckel potentials. *Astrophysical Journal*, **322**, 618–631.

BLUMENTHAL, G. R., FABER, S. M., FLORES, R., PRIMACK, J. R.: 1986. Contraction of dark matter galactic halos due to baryonic infall. *Astrophysical Journal*, **301**, 27–34.

CARPINTERO, D. D. AGUILAR, L. A.: 1998. Orbit classification in arbitrary 2d and 3d potentials. *Monthly Notices of the Royal Astronomical Society*, **298**, 1–21.

CLUTTON-BROCK, M.: 1973. The Gravitational Field of Three Dimensional Galaxies. *Astrophysics and Space Science*, **23**, 55–+.

COURTEAU, S. RIX, H. W.: 1999. Maximal disks and the tully-fisher relation. *Astrophysical Journal*, **513**, 561–571.

CRETTON, N., NAAB, T., RIX, H., BURKERT, A.: 2001. The Kinematics of 3:1 Merger Remnants and the Formation of Low-Luminosity Elliptical Galaxies. *Astrophysical Journal*, **554**, 291–297.

CRETTON, N., RIX, H., DE ZEEUW, P. T.: 2000. The Distribution of Stellar Orbits in the Giant Elliptical Galaxy NGC 2320. *Astrophysical Journal*, **536**, 319–330.

DE JONG, S., KASSIN, A., BELL, E., COURTEAU, S.: 2003. Properties of Dark Matter Halos in Disk Galaxies. *astro-ph*, **0311100**.

DE ZEEUW, P. T., HUNTER, C., SCHWARZSCHILD, M.: 1987. Nonuniqueness of self-consistent equilibrium solutions for the perfect elliptic disk. *Astrophysical Journal*, **317**, 607–636.

DE ZEEUW, P. T. LYNDEN-BELL, D.: 1985. Best approximate quadratic integrals in stellar dynamics. *Monthly Notices of the Royal Astronomical Society*, **215**, 713–730.

DE ZEEUW, T.: 1985. Elliptical galaxies with separable potentials. *Monthly Notices of the Royal Astronomical Society*, **216**, 273–334.

DEHNEN, W. BINNEY, J.: 1998. Mass models of the milky way. *Monthly Notices of the Royal Astronomical Society*, **294**, 429+.

DEHNEN, W. GERHARD, O. E.: 1993. Three-integral models of oblate elliptical galaxies. *Monthly Notices of the Royal Astronomical Society*, **261**, 311–336.

DEHNEN, W. GERHARD, O. E.: 1994. Two-Integral Models for Oblate Elliptical Galaxies with Cusps. *Monthly Notices of the Royal Astronomical Society*, **268**, 1019–+.

DUBINSKI, J.: 1994. The effect of dissipation on the shapes of dark halos. *Astrophysical Journal*, **431**, 617–624.

DUBINSKI, J. CARLBERG, R. G.: 1991. The structure of cold dark matter halos. *Astrophysical Journal*, **378**, 496–503.

ESKRIDGE, P. B., FABBIANO, G., KIM, D.: 1995. A multiparametric analysis of the Einstein sample of early-type galaxies. 2: Galaxy formation history and properties of the interstellar medium. *Astrophysical Journal*, **442**, 523–537.

EVANS, N. W. DE ZEEUW, P. T.: 1994. Observable properties of the power-law galaxies. *Monthly Notices of the Royal Astronomical Society*, **271**, 202–222.

FLORES, R., PRIMACK, J. R., BLUMENTHAL, G. R., FABER, S. M.: 1993. Rotation curves from baryonic infall - dependence on disk-to-halo ratio, initial angular momentum, and core radius, and comparison with data. *Astrophysical Journal*, **412**, 443–454.

GERHARD, O. E.: 1993. Line-of-sight velocity profiles in spherical galaxies: breaking the degeneracy between anisotropy and mass. *Monthly Notices of the Royal Astronomical Society*, **265**, 213–+.

GERHARD, O. E. BINNEY, J.: 1985. Triaxial galaxies containing massive black holes or central density cusps. *Monthly Notices of the Royal Astronomical Society*, **216**, 467–502.

HAIRER, E., NRSETT, S., WANNER, G.: 1987. *Solving Ordinary Differential Equations I. Nonstiff Problems.* Springer-Verlag.

HEILIGMAN, G. SCHWARZSCHILD, M.: 1979. On the nonexistence of three-dimensional tube orbits around the intermediate axis in a triaxial galaxy model. *Astrophysical Journal*, **233**, 872–876.

HERNQUIST, L.: 1990. An analytical model for spherical galaxies and bulges. *Astrophysical Journal*, **356**, 359–364.

HERNQUIST, L.: 1993. N-body realizations of compound galaxies. *Astrophysical Journal Supplement Series*, **86**, 389–400.

HERNQUIST, L. OSTRIKER, J. P.: 1992. A self-consistent field method for galactic dynamics. *Astrophysical Journal*, **386**, 375–397.

HEYL, J. S., HERNQUIST, L., SPERGEL, D. N.: 1994. Structure of merger remnants. 4: Isophotal shapes. *Astrophysical Journal*, **427**, 165–173.

HOZUMI, S.: 1997. A Phase-Space Approach to Collisionless Stellar Systems Using a Particle Method. *Astrophysical Journal*, **487**, 617–+.

HUBBLE, E. P.: 1926. Extragalactic nebulae. *Astrophysical Journal*, **64**, 321–369.

HUNTER, C.: 1995. Nonuniqueness of Self-Consistent Models. In *Three-Dimensional Systems*, Seiten 76–+.

HUNTER, C.: 2001. Constructing Stellar Dynamic Models for Elliptical Galaxies. In *Stellar Dynamics: from Classic to Modern*, Seiten 281–+.

HUNTER, C.: 2002. Spectral Analysis of Orbits via Discrete Fourier Transforms. *Space Science Reviews*, **102**, 83–99.

HUNTER, C. DE ZEEUW, P. T.: 1992. Triaxial galaxy models with thin tube orbits. *Astrophysical Journal*, **389**, 79–117.

JEANS, J. H.: 1924. Cosmogonic problems associated with a secular decrease of mass. *Monthly Notices of the Royal Astronomical Society*, **85**, 2–+.

KAWAI, A., FUKUSHIGE, T., MAKINO, J., TAIJI, M.: 2000. GRAPE-5: A Special-Purpose Computer for N-Body Simulations. *Publications of the Astronomical Society of Japan*, **52**, 659–676.

KHOCHFAR, S. BURKERT, A.: 2003. Orbital Paramters of Merging Dark Matter Halos. *astro-ph*, **0309611**.

KRONAWITTER, A., SAGLIA, R. P., GERHARD, O., BENDER, R.: 2000. Orbital structure and mass distribution in elliptical galaxies. *Astronomy and Astrophysics Supplement Series*, **144**, 53–84.

KUIJKEN, K. MERRIFIELD, M. R.: 1993. A New Method for Obtaining Stellar Velocity Distributions from Absorption-Line Spectra - Unresolved Gaussian Decomposition. *Monthly Notices of the Royal Astronomical Society*, **264**, 712–+.

LASKAR, J.: 1993. Frequency analysis of a dynamical system. *Celestial Mechanics and Dynamical Astronomy*, **56**, 191–196.

LEVISON, H. F. RICHSTONE, D. O.: 1985. Internal dynamics of highly flattened spheroidal systems. *Astrophysical Journal*, **295**, 349–357.

LIMA-NETO, G. B. COMBES, F.: 1995. Isophote shapes of merger remnants. *Astronomy and Astrophysics*, **294**, 657–666.

MARCHESINI, D., D'ONGHIA, E., CHINCARINI, G., FIRMANI, C., CONCONI, P., MOLINARI, E., ZACCHEI, A.: 2002. Hα Rotation Curves: The Soft Core Question. *Astrophysical Journal*, **575**, 801–813.

MATHIEU, A. DEJONGHE, H.: 1999. Triaxial dynamical models of elliptical galaxies using Stackel potentials. *Monthly Notices of the Royal Astronomical Society*, **303**, 455–465.

MATTHIAS, M. GERHARD, O.: 1999. Dynamics of the boxy elliptical galaxy NGC 1600. *Monthly Notices of the Royal Astronomical Society*, **310**, 879–891.

MERRITT, D.: 1996. Optimal smoothing for n-body codes. *Astronomical Journal*, **111**, 2462+.

MERRITT, D.: 1997. Cusps and Triaxiality. *Astrophysical Journal*, **486**, 102–+.

MERRITT, D. FRIDMAN, T.: 1996. Triaxial Galaxies with Cusps. *Astrophysical Journal*, **460**, 136–+.

MERRITT, D. HERNQUIST, L.: 1991. Stability of nonrotating stellar systems. II - Prolate shell-orbit models. *Astrophysical Journal*, **376**, 439–457.

MIRALDA-ESCUDE, J. SCHWARZSCHILD, M.: 1989. On the orbit structure of the logarithmic potential. *Astrophysical Journal*, **339**, 752–762.

MO, H. J., MAO, S., WHITE, S. D. M.: 1998. The formation of galactic discs. *Monthly Notices of the Royal Astronomical Society*, **295**, 319–336.

NAAB, T.: 2000. Formation of Massive Elliptical Galaxies in a Mixed Merger Scenario. *PhD thesis*, Seiten 267–+.

NAAB, T., BURKERT, A., HERNQUIST, L.: 1999. On the Formation of Boxy and Disky Elliptical Galaxies. *Astrophysical Journal Letters*, **523**, L133–L136.

NAVARRO, J. F., EKE, V. R., FRENK, C. S.: 1996a. The cores of dwarf galaxy haloes. *Monthly Notices of the Royal Astronomical Society*, **283**, L72–L78.

NAVARRO, J. F., FRENK, C. S., WHITE, S. D. M.: 1996b. The structure of cold dark matter halos. *Astrophysical Journal*, **462**, 563+.

PIERCE, M. J. TULLY, R. B.: 1992. Luminosity-line width relations and the extragalactic distance scale. I - Absolute calibration. *Astrophysical Journal*, **387**, 47–55.

QIAN, E. E., DE ZEEUW, P. T., VAN DER MAREL, R. P., HUNTER, C.: 1995. Axisymmetric galaxy models with central black holes, with an application to M32. *Monthly Notices of the Royal Astronomical Society*, **274**, 602–622.

RICHSTONE, D. O. TREMAINE, S.: 1984. A general method for constructing spherical galaxy models. *Astrophysical Journal*, **286**, 27–37.

RICHSTONE, D. O. TREMAINE, S.: 1985. Dynamical models of M87 without a central black hole. *Astrophysical Journal*, **296**, 370–378.

RICHSTONE, D. O. TREMAINE, S.: 1988. Maximum-entropy models of galaxies. *Astrophysical Journal*, **327**, 82–88.

RIX, H., DE ZEEUW, P. T., CRETTON, N., VAN DER MAREL, R. P., CAROLLO, C. M.: 1997. Dynamical Modeling of Velocity Profiles: The Dark Halo around the Elliptical Galaxy NGC 2434. *Astrophysical Journal*, **488**, 702–+.

RIX, H. WHITE, S. D. M.: 1992. Optimal estimates of line-of-sight velocity distributions from absorption line spectra of galaxies - Nuclear discs in elliptical galaxies. *Monthly Notices of the Royal Astronomical Society*, **254**, 389–403.

RYDEN, B. S.: 1988. Galaxy formation - The role of tidal torques and dissipational infall. *Astrophysical Journal*, **329**, 589–611.

RYDEN, B. S.: 1991. Compression of dark halos by baryon infall - self-similar solutions. *Astrophysical Journal*, **370**, 15–24.

RYDEN, B. S. GUNN, J. E.: 1987. Galaxy formation by gravitational collapse. *Astrophysical Journal*, **318**, 15–31.

SALMON, J. K. WARREN, M. S.: 1994. Skeletons from the treecode closet. *Journal of Computational Physics*, **111**, 136–155.

SCHWARZSCHILD, M.: 1979. A numerical model for a triaxial stellar system in dynamical equilibrium. *Astrophysical Journal*, **232**, 236–247.

SCORZA, C. BENDER, R.: 1995. The internal structure of disky elliptical galaxies. *Astronomy and Astrophysics*, **293**, 20–43.

STATLER, T. S.: 1987. Self-consistent models of perfect triaxial galaxies. *Astrophysical Journal*, **321**, 113–152.

STATLER, T. S., LAMBRIGHT, H., BAK, J.: 2001. Uncovering the Intrinsic Shapes of Elliptical Galaxies. IV. Tests on Simulated Merger Remnants. *Astrophysical Journal*, **549**, 871–877.

STATLER, T. S. SAURON TEAM: 2003. NGC 4365: A Truly Triaxial Galaxy. *AAS/Division of Dynamical Astronomy Meeting*, **34**, 0–+.

TERZIC, B.: 2003. Building self-consistent triaxial galaxy models using schwarzschild's method. *astro-ph*, **0305005**.

TOOMRE, A. TOOMRE, J.: 1972. Galactic Bridges and Tails. *Astrophysical Journal*, **178**, 623–666.

TREMAINE, S. D. DE ZEEUW, P. T.: 1987. Stellar Dynamics of Needles. In *IAU Symp. 127: Structure and Dynamics of Elliptical Galaxies*, Seiten 493–+.

VALLURI, M. MERRITT, D.: 2000. Orbital Instability and Relaxation in Stellar Systems. In *The Chaotic Universe, Proceedings of the Second ICRA Network Workshop, Advanced Series in Astrophysics and Cosmology, vol.10, Edited by V. G. Gurzadyan and R. Ruffini, World Scientific, 2000, p.229*, Seiten 229–+.

VAN DEN BOSCH, F. C. SWATERS, R. A.: 2001. Dwarf galaxy rotation curves and the core problem of dark matter haloes. *Monthly Notices of the Royal Astronomical Society*, **325**, 1017–1038.

VAN DER MAREL, R. P., CRETTON, N., DE ZEEUW, P. T., RIX, H.: 1998. Improved Evidence for a Black Hole in M32 from HST/FOS Spectra. II. Axisymmetric Dynamical Models. *Astrophysical Journal*, **493**, 613–+.

VAN DER MAREL, R. P. FRANX, M.: 1993. A new method for the identification of non-Gaussian line profiles in elliptical galaxies. *Astrophysical Journal*, **407**, 525–539.

WEIL, M. L. HERNQUIST, L.: 1996. Global Properties of Multiple Merger Remnants. *Astrophysical Journal*, **460**, 101–+.

WEINBERG, M. D.: 1994. Adiabatic invariants in stellar dynamics, 3: Application to globular cluster evolution. *Astronomical Journal*, **108**, 1414–1420.

WEINBERG, M. D.: 1999. An Adaptive Algorithm for N-Body Field Expansions. *Astronomical Journal*, **117**, 629–637.

Ich möchte mich an dieser Stelle bei allen bedanken, die mich privat oder beruflich oder manchmal auch beides während meiner Promotion unterstützt und immer wieder ermutigt haben. Danke! Thanks to ...

Meinen Betreuer Prof. Dr. Andreas Burkert, der mich immer von neuem gefordert, gefördert und inspiriert hat. Ich möchte Ihm außerdem herzlich danken für die Unterstützung in persönlich sehr schweren Zeiten, ohne die ich die Arbeit nicht hätte zu Ende bringen können.

Prof. Dr. Hans Walter Rix fuer die Möglichkeit am Max-Planck-Institut für Astronomie meine Promotion anfertigen zu dürfen, für die Begutachtung dieser Arbeit und für viele hilfreiche Diskussionen.

Prof. Dr. Wilhelm Kley für das Verständnis meiner Lage.

Ein großes Dankeschön an Dr. Thorsten Naab meinem 'Co-Betreuer', der immer ein offenes Ohr hatte. Für die jetzige und zukünftige wissenschaftliche Zusammenarbeit und für viele, viele Merger ...

The whole theory group, for discussions, help, patience and delightful company throughout.

Shunsuke Hozumi for his help on self-consistent field methods. For the patience in explaining them to me. For the codes he generously provided and his company, which I enjoyed a lot.

Daniel Carpintero for his invaluable classification code.

Ja, Sadegh, alles endet einmal, but we will meet again young Khochfar ...

Nick Nock, the last man standing in Heidelberg! Danke für alles!

Sami Dib, for the reinterpretation of meat waggons, lost keys and for a good political education!

Emir Poturak in some sense my only true WG partner (hi Sadegh ;-))

An Michael, Angela und Andrea meine Zimmergenossen!

Sabine und Michael für die Gastfreundschaft in der entscheidenden Phase dieser Arbeit!

To the many colleagues and friends at the MPIA, which made the stay more delightful and more fun especially Greg Rudnick and Thilo Kranz (the old sofa clique). Robert Weiss for another kind of political education, ich werde die Diskussionen vermissen! To Markus Wetzstein, my first, only and last line of defense in all things organisational. Elena D'Onghia for a broader view on all things astronomical. Elena Puga for all the good advice and just good company.

Meine AEGEE Kumpanen, die jetzt nach München emigriert sind, Heiko, Nicole und Nadine.

Meine Freunde aus Hamburg Kai, Laue, Carsten, Jens, Pollegopoulous und Gesa und vor allem Steffi Arens, Stephan Keten und Levent Demirörs, die, dass muss außerdem erwähnt werden, es als einzige geschafft haben in den letzten sieben Jahren die Elbe in Richtung Süden zu überqueren! Danke für alles!

Mireia, ohne dich würde hier keine Zeile stehen.

And Death Shall Have No Dominion

And death shall have no dominion.
Dead men naked they shall be one
With the man in the wind and the west moon;
When their bones are picked clean and the clean bones gone,
They shall have stars at elbow and foot;
Though they go mad they shall be sane,
Though they sink through the sea they shall rise again;
Though lovers be lost love shall not;
And death shall have no dominion.

And death shall have no dominion.
Under the windings of the sea
They lying long shall not die windily;
Twisting on racks when sinews give way,
Strapped to a wheel, yet they shall not break;
Faith in their hands shall snap in two,
And the unicorn evils run them through;
Split all ends up they shan't crack;
And death shall have no dominion.

And death shall have no dominion.
No more may gulls cry at their ears
Or waves break loud on the seashores;
Where blew a flower may a flower no more
Lift its head to the blows of the rain;
Though they be mad and dead as nails,
Heads of the characters hammer through daisies;
Break in the sun till the sun breaks down,
And death shall have no dominion.

Dylan Thomas